Universidade do Estado do Rio de Janeiro
Centro de Tecnologia e Ciências
Instituto de Física Armando Dias Tavares

Mauricio Thiel

Study of WW Central Exclusive Production in the semileptonic channel with tagged protons at CMS detector

Rio de Janeiro
2019

Mauricio Thiel

Study of WW Central Exclusive Production in the semileptonic channel with tagged protons at CMS detector

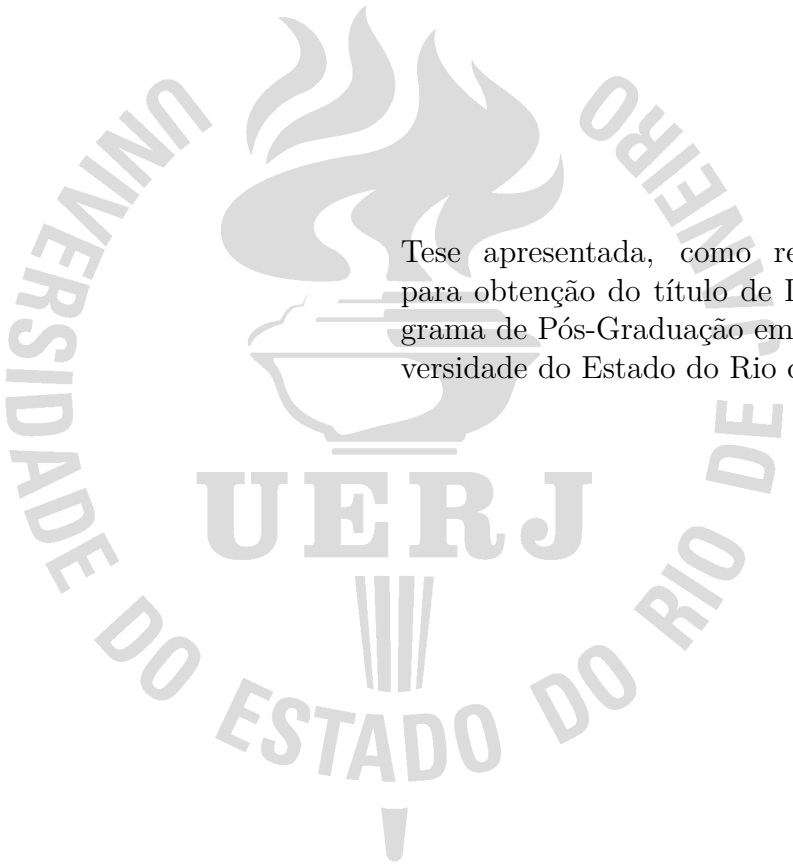

Tese apresentada, como requisito parcial para obtenção do título de Doutor, ao Programa de Pós-Graduação em Física, da Universidade do Estado do Rio de Janeiro.

Orientador: Prof. Dr. Luiz Martins Mundim Filho
Coorientador: Prof^a. Dr^a. Maria Clemencia Rosario Mora Herrera

Rio de Janeiro
2019

CATALOGAÇÃO NA FONTE
UERJ/ REDE SIRIUS / BIBLIOTECA CTC/D

T431s Thiel, Mauricio.
Study of WW Central Exclusive Production in the semileptonic channel with tagged protons at CMS detector / Mauricio Thiel. – 2019.
109 f. : il.

Orientador: Luiz Martins Mundim Filho.
Coorientadora: María Clemencia Rosario Mora Herrera.
Tese (doutorado) - Universidade do Estado do Rio de Janeiro, Instituto de Física Armando Dias Tavares.

1. Bósons W – Teses. 2. Prótons – Detectores – Teses. 3. Interação próton-próton – Teses. 4. Teoria de campos (Física) – Teses. 5. Solenóide de múon compacto – Teses. 6. Grande colisor de hádrons (França e Suíça) – Teses. I. Mundim Filho, Luiz Martins. II. Mora Herrera, María Clemencia Rosario. III. Universidade do Estado do Rio de Janeiro. Instituto de Física Armando Dias Tavares. IV. Título.

CDU 539.12

Bibliotecária: Teresa da Silva CRB7/5209

_____ _____

Assinatura Data

Mauricio Thiel

Study of WW Central Exclusive Production in the semileptonic channel with tagged protons at CMS detector

Tese apresentada, como requisito parcial para obtenção do título de Doutor, ao Programa de Pós-Graduação em Física, da Universidade do Estado do Rio de Janeiro.

Aprovada em 29 de Abril de 2019.
Banca Examinadora:

Prof. Dr. Luiz Martins Mundim Filho (Orientador)
Instituto de Física Armando Dias Tavares – UERJ

Prof^a. Dr^a. Maria Clemencia Rosario Mora Herrera (Coorientador)
Instituto de Física Armando Dias Tavares – UERJ

Prof. Dr. Arthur Marques Moraes
Centro Brasileiro de Pesquisas Físicas

Prof. Dr. Murilo Santana Rangel
Universidade Federal do Rio de Janeiro

Prof^a. Dr^a. María Elena Pol
Centro Brasileiro de Pesquisas Físicas

Prof. Dr. Antonio Vilela Pereira
Instituto de Física Armando Dias Tavares – UERJ

Prof^a. Dr^a. Patrícia Teles
Instituto de Física Armando Dias Tavares – UERJ

Prof. Dr. Wagner de Paula Carvalho
Instituto de Física Armando Dias Tavares – UERJ

Rio de Janeiro

2019

AGRADECIMENTOS

Primeiramente gostaria de agradecer a minha família, que sempre me deu incentivo para estudar, especialmente minha mãe Renilda.

Agradeço a todo corpo técnico e docente do DFNAE, especialmente ao meu orientador Luiz Mundim, o qual sempre depositou confiança no meu trabalho e foi compreensivo nos momentos mais difíceis.

Um grande obrigado aos colegas e amigos feitos na UERJ durante o doutoramento, sem os quais eu não teria conseguido terminar, em especial Ewerton, Marcão, Miguel, Raphael e claro, Eduardo.

Agradeço também aos amigos feitos no Rio durante esses 5 anos, em especial aos moradores do apê da Uruguai: Hélio, Murilo, Guga e Yuri.

Por fim, agradeço aos amigos, colegas e professores que me deram suporte para que eu pudesse chegar até o início do doutorado.

Este trabalho foi financiado pela Coordenação de Aperfeiçoamento de Pessoal de Nível Superior - Brasil (CAPES) - Código de Financiamento 001.

ABSTRACT

THIEL, M. *Study of WW Central Exclusive Production in the semileptonic channel with tagged protons at CMS detector*. 2019. 107 f. Tese (Doutorado em Física) – Instituto de Física Armando Dias Tavares, Universidade do Estado do Rio de Janeiro, Rio de Janeiro, 2019.

One of the most efficient approaches to look for physics Beyond the Standard Model is the use of the Effective Field Theory (EFT) to describe higher energy theoretical models at lower energies, like that of the LHC. In this type of scenario, it is possible to have additional couplings to describe gauge bosons self-interactions, such as anomalous Triple and Quartic Gauge Couplings (aQGCs). These anomalous gauge couplings can appear, for example, as an excess in the cross section of the $\gamma\gamma \to WW$ process. The CMS subdetector Precision Proton Spectrometer (PPS) consists of detector stations at around 200 m on both sides of the interaction point, allowing to detect protons that remained intact after losing a fraction of their energy in the interaction. PPS is an extremely important tool to investigate Central Exclusive Production (CEP) with high levels of pileup collisions. CEP processes are characterized by $p + p \to p^* \oplus X \oplus p^*$, where $\oplus$ represents rapidity gaps, X is the central final state (which could be WW, ZZ, di-jet, etc.) and p (p^*) are the protons in the initial (final) state. An analysis of the CEP of W boson pairs for CMS data recorded during 2016 is presented in this thesis, considering aQGCs in the EFT dimension-6 scenario. The semileptonc channel was chosen, which is characterized in the final state by the presence of a muon, missing transverse energy and a single large jet in the central CMS detector plus two scattered protons in PPS. The dataset analyzed has an integrated luminosity of about 10 fb^{-1} and no event is found after the event selection. The aQGC parameters $\alpha_0^W/\Lambda^2 > 5.0 \times 10^{-4}$ GeV^{-2} and $\alpha_C^W/\Lambda^2 > 15.0 \times 10^{-4}$ GeV^{-2}, considering a form factor of 500 GeV, were excluded at 95% C.L.. Although these limits were already excluded in the previous analysis the study presented discuss a prospect for the entire Run II CMS dataset (about 100 fb^{-1}).

Keywords: Anomalous Couplings. Central Exclusive Production. CMS. LHC.

RESUMO

THIEL, M. *Estudo da Produção Central Exclusiva de WW no canal semi-leptônico com detecção de prótons no detector CMS*. 2019. 107 f. Tese (Doutorado em Física) – Instituto de Física Armando Dias Tavares, Universidade do Estado do Rio de Janeiro, Rio de Janeiro, 2019.

Uma das mais eficientes abordagens para procurar por física além do Modelo Padrão é o uso da Teoria de Campos Efetiva (EFT, sigla em inglês para *Effective Field Theory*) para descrever os modelos teóricos de energias muito altas em energias mais baixas, como a do LHC. Neste tipo de cenário é possível ter acoplamentos adicionais para descrever as auto-interações entre os bósons de calibre, como por exemplo acoplamentos anômalos triplos e quárticos (aQGC, sigla em inglês para *anomalous Quartic Gauge Coupling*). Estes acoplamentos de calibre anômalos podem se manifestar, por exemplo, como um excesso na seção de choque do processo $\gamma\gamma \to WW$. O subdetector Espectrômetro de Prótons de Precisão (PPS, sigla em inglês para *Precision Proton Spectrometer*), do CMS, consiste em estações de detecção colocados em torno de 200 m em ambos os lados do ponto de interação, permitindo detectar prótons que permaneceram intactos após perder uma fração de sua energia na interação. O PPS é uma ferramenta importante para investigar a Produção Exclusiva Central (CEP, sigla em inglês para *Central Exclusive Production*) em colisões com alto nível de empilhamento. O processo CEP é caracterizado por $p + p \to p^* \oplus X \oplus p^*$, onde $\oplus$ representa lacunas de rapidez, X é o estado final central (o qual pode ser WW, ZZ, di-jatos, etc.) e p (p^*) são os prótons no estado inicial (final). Nesta tese, é apresentada uma análise CEP de pares de bósons W para os dados do CMS coletados durante o ano de 2016, considerando aQGC no cenário de dimensão-6 da EFT. O canal escolhido é o semileptônico, o qual é caracterizado no estado final pela presença de um muon, energia transversa perdida e um único jato grande no detector central e dois prótons espalhados no PPS. O conjunto de dados analisado tem uma luminosidade integrada em torno de 10 fb^{-1} e nenhum evento foi encontrado após o processo de seleção. Os parâmetros aQGC $\alpha_0^W/\Lambda^2 > 5.0 \times 10^{-4}$ GeV^{-2} e $\alpha_C^W/\Lambda^2 > 15.0 \times 10^{-4}$ GeV^{-2}, considerando um fator de forma de 500 GeV, foram excluídos com 95% C.L.. Embora estes limites já tenham sido excluídos em análises prévias, o estudo apresentado discute um prognóstico para todo o conjunto de dados do CMS no Run II (em torno de 100 fb^{-1}).

Palavras-chave: Acoplamentos Anômalos. Produção Central Exclusiva. CMS. LHC.

LIST OF FIGURES

LIST OF TABLES

CONTENTS

INTRODUCTION

Each piece, or part, of the whole of nature is always merely an approximation to the complete truth, or the complete truth so far as we know it.

Richard P. Feynman

The development of the scientific method brought to the investigation of Nature a junction between experiment and hypothetical explanations. From the first astronomical observations made by Galileo Galilei to the most recent particle colliders, the technology has advanced in unthinkable scales for the first physicists.

One of the greatest examples of the advancement of scientific experiments is the Large Hadron Collider (LHC) and its detectors, which were built in collaboration of more than 100 countries and thousands of scientists. It makes possible the investigation of several aspects of the Standard Model — the theory that describes the elementary particles — and beyond. The high center-of-mass energy and the large amount of data collected in the LHC operation period represents a landmark in the high energy physics studies and it already was responsible for important discoveries, such as the Higgs Boson.

The Compact Muon Solenoid (CMS) Experiment was built in the LHC interaction point 5 (P5) with a general purpose concept and a cylindrical shape divided into different layers of subdetectors. Among them, it is important to mention the muon chambers with its high precision characterization of muons, the hadron calorimeter surrounding entirely the interaction point that allows to see a large range of particles and the tracking system that combined with a high magnetic field perform an accurate momentum measurement.

Over the years CMS was upgraded in order to explore different aspects of Nature. The Precision Proton Spectrometer (PPS) subdetector started to collect data on 2016 and it was composed by two (three in the 2017-2018 configuration) roman pots in each side of the central detector which allows the insertion of sensors close to the beam and consequently, it can detect with high precision the protons scattered at small angles. The general aspects of LHC, CMS and the PPS are discussed in chapter 2, as well as the contribution of the author for the CMS Collaboration, working in the PPS commissioning.

The beginning of PPS operation opened a new window to investigate the physics of the Central Exclusive Production (CEP), where the protons remain intact after the interaction and a system X is produced centrally. The proton information associated with the central information of the system X is an important tool to discriminate the exclusive events compared to the huge amount of inclusive events in a high energy collision. The system X can be a di-jet, a W boson pair, a Z boson pair or many other processes. The scope of this thesis is the investigation of the anomalous Quartic Gauge Couplings

(aQGCs) predicted by the Effective Field Theory for the process $\gamma\gamma \to WW$, which has the CEP topology as a remarkable way to observe it. The main aspects of the Standard Model and the Effective Field Theory formulation for the aQGCs description in a WW production is presented in chapter 1.

The search for these anomalous couplings was done in previous experiments as D0 and L3 at Tevatron and LEP colliders respectively, no excess above the background expectation was found in both studies, however limits for aQGCs were stipulated. With the beginning of LHC operation, CMS and ATLAS have lowered the limits for the aQGCs parameters using data from 7 TeV and 8 TeV center-of-mass energy collision. Against the high background of the WW process, both CMS and ATLAS used the exclusive topology to look for large rapidity gaps between the protons and the central system to discriminate the signal from the background.

In the beginning of the LHC period called Run II, the center-of-mass energy was raised to 13 TeV as well as the average number of proton collision per bunch crossing, the pileup, which makes the previous CMS and ATLAS strategy inefficient because of the rise of particle multiplicity in the central detector and the rapidity gaps can not be well characterized. In other hand, the possibility of detect the scattered protons opened an opportunity to investigate the aQGC parameters below the established limits.

The first aQGCs study, in the LHC context, using the scattered protons information as a strategy to discriminate signal from background is presented. The chosen channel is the semileptonic one, where one W boson decays into quarks giving origin to jets and the other decays in a lepton plus neutrino, the muon case is used. This channel has a higher branching ratio compared with the fully leptonic, used in previous analysis. It is the first analysis that combines a semileptonic channel with the proton information for the WW production. The CMS 2016 data were analyzed, the data and the Monte Carlo simulated samples are listed and discussed in chapter 3, as well as the generators used. The analysis strategy and the results are presented in chapter 4. In the conclusions, in chapter 5, it is discussed the perspectives for this analysis with the data collected on the 2016 - 2018 period.

1 THE STANDARD MODEL OF PARTICLE PHYSICS AND BEYOND

1.1 Standard Model of particle physics

The understanding of Nature goes through the description and comprehension of its fundamental interactions and constituents. After decades of efforts by physicists, the picture of Nature is composed of four fundamental interactions, described as:

- **Strong Interaction**: It is responsible for the existence of protons and neutrons, biding together their constituents — the quarks — and responsible for keeping the nucleons bonded to make the nuclei. This interaction acts at very short distances and it is described by the Theory of Quantum Chromodynamics (QCD).

- **Weak Interaction**: It describes the neutron decay to proton by the beta-decay. This kind of decay is extremely important to explain the synthesis of heavy elements in the early Universe. It also acts at very short distances and it is described by the Electroweak Theory.

- **Electromagnetic Interaction**: It explains the electron and nuclei attraction — that is crucial to build atoms and molecules — and the chemistry description. Different of the first two interactions, it acts at infinite distances and in the quantum regime it can be described by the Theory of Quantum Electrodynamics (QED) or, with the Electroweak unification, through the Electroweak Theory.

- **Gravitational Interaction**: The weakest interaction of all, it describes the interaction between large bodies such as planets, stars and galaxies. Also, it acts at infinite distances and it is described by General Relativity, which does not work in the quantum regime.

The Standard Model (SM) includes the first three interactions, then to describe the physics of elementary particles, a good knowledge of the QCD and Electroweak Theory is needed. Both theories describe the interaction between elementary particles that are classified into quarks, leptons — both are fermions and the constituents of the matter — and the gauge bosons, which are responsible to mediate the interactions. These elementary particles are summarized in table 1. There is also a scalar particle in the Standard Model which explains the mass generation of these particles, the Higgs boson, discovered recently at the LHC (ATLAS COLLABORATION, 2012); (CMS COLLABORATION, 2012).

The Standard Model is formulated as a quantum field theory with $SU(3)_{color} \times SU(2)_{isospin} \times U(1)_{hypercharge}$ local gauge symmetry. The $SU(3)_{color}$ symmetry represents Quantum Chromodynamics and it describes the interaction between the particles that carry color charge - quarks and gluons - by exchange of the strong interaction gauge

Table 1 - The Standard Model particles and some properties.

Particle	Mass(GeV)	Charge (e)	spin
Leptons			
e	5.11×10^{-4}	-1	$1/2$
ν_e	0	0	$1/2$
μ	0.106	-1	$1/2$
ν_μ	0	0	$1/2$
τ	1.777	-1	$1/2$
ν_τ	0	0	$1/2$
Quarks			
u	2.2×10^{-3}	$+2/3$	$1/2$
d	4.7×10^{-3}	$-1/3$	$1/2$
s	95.0×10^{-3}	$-1/3$	$1/2$
c	1.275	$+2/3$	$1/2$
b	4.18	$-1/3$	$1/2$
t	173.0	$+2/3$	$1/2$
Gauge Bosons			
γ	0	0	1
Z	91.188	0	1
$W^\pm$	80.379	± 1	1
g	0	0	1
Scalar Bosons			
H	125.18	0	0

Subtitle: The Standard Model particles and their respective mass, charge and spin. The values were extracted from (BERINGER et al., 2012).

Source: The author, 2019.

boson, the gluon (g). QCD is very successful to describe aspects of the strong interaction as color confinement and asymptotic freedom (HALZEN; MARTIN, 1984).

1.1.1 Electroweak Theory

In the 1960's S. Weinberg, A. Salam and L. Glashow built a model to describe the electromagnetic and weak interaction together, the Electroweak Theory (SALAM, 1968), (WEINBERG, 1967) and (GLASHOW, 1961). This theory obeys the symmetry of the $SU(2)_{isospin} \times U(1)_{hypercharge}$ group, the weak interaction comes from the $SU(2)$ symmetry generated by the weak isospin and the electromagnetic interaction from the $U(1)$ symmetry generated by the hypercharge.

This theory is a gauge theory, which means that the Lagrangian is invariant under local transformations. As a consequence, the gauge bosons ($W^{\pm}$ and Z) come automatically from the gauge symmetries. The Lagrangian density of this model can be written as:

$$\mathcal{L} = \mathcal{L}_0 + \mathcal{L}_I \ , \tag{1}$$

where $\mathcal{L}_0$ represents the free fields Lagrangian density and it can be written as:

$$\begin{aligned}
\mathcal{L}_0 &= \bar{\psi}_l(i\not{\partial} - m_l)\psi_l + \bar{\psi}_{\nu l}(i\not{\partial})\psi_{\nu l} \\
&- \frac{1}{4}F_{\mu\nu}F^{\mu\nu} \\
&- \frac{1}{2}F^{\dagger}_{W\mu\nu}F^{\mu\nu}_{W} + m^2_W W^{\dagger}_{\mu}W^{\mu} \\
&- \frac{1}{4}Z_{\mu\nu}Z^{\mu\nu} + \frac{1}{2}m^2_Z Z_{\mu}Z^{\mu} \\
&+ \frac{1}{2}(\partial^{\mu}\sigma)(\partial_{\mu}\sigma) - \frac{1}{2}m^2_H\sigma^2 \ .
\end{aligned} \tag{2}$$

The first line describes the free leptons Lagrangian density, where $\psi_{l,\nu l}$ is the Dirac field of the lepton, m_l is the mass of the lepton and $\not{\partial}$ is defined by $\gamma^{\mu}\partial_{\mu}$ where γ^{μ} are the Dirac matrices. In the second line, there are the free photons with the electromagnetic field tensor $F_{\mu\nu}$ given by:

$$F_{\mu\nu} = \partial_{\mu}A_{\nu} - \partial_{\nu}A_{\mu} \ , \tag{3}$$

where A^{μ} is the four-vector potential of Electromagnetism. The charged gauge bosons are represented in the third line with the $F^{\mu\nu}_W$ tensor written in terms of the vector field W^{μ}:

$$F^{\mu\nu}_W = \partial^{\mu}W^{\nu} - \partial^{\nu}W^{\mu} \ . \tag{4}$$

In the fourth line the terms that include the neutral gauge boson Z are given, where the $Z^{\mu\nu}$ tensor is written in terms of the vector field Z^{μ}:

$$Z^{\mu\nu} = \partial^{\mu} Z^{\nu} - \partial^{\nu} Z^{\mu} \ . \tag{5}$$

The mass terms m_W and m_Z in equation (2) represent the masses of the gauge bosons W and Z respectively. The interaction bosons should be naturally massless in a theory with gauge symmetry, however, that was not that was seen in the experiments. Then, to generate mass for these gauge bosons Robert Brout, François Englert and Peter Higgs proposed the spontaneous symmetry breaking mechanism (ENGLERT; BROUT, 1964) and (HIGGS, 1964), which introduces the mass of these gauge bosons as an interaction with a new scalar field, called Higgs Field with a non-zero vacuum expectation value, and consequently the existence of a new particle, called Higgs Boson, that was discovered recently at the LHC. With this new field, it is possible to understand the last line of the equation (2), σ is the Higgs Field and m_H is the mass of the Higgs Boson.

The second term in the equation (1), $\mathcal{L}_I$, represents the interaction Lagrangian density and can be written as:

$$\mathcal{L}_I = \mathcal{L}_I^{LB} + \mathcal{L}_I^{BB} + \mathcal{L}_I^{HH} + \mathcal{L}_I^{HB} + \mathcal{L}_I^{HL} \ , \tag{6}$$

where the terms describe the interactions between leptons and gauge bosons, the interactions between the gauge bosons, the Higgs Boson self-interactions, the interactions between Higgs Bosons and gauge bosons and the interactions between Higgs bosons and leptons respectively. The term of interest of this thesis is the $\mathcal{L}_I^{BB}$.

The $\mathcal{L}_I^{BB}$ Lagrangian density can be written as:

$$\begin{aligned}
\mathcal{L}_I^{BB} &= ig\cos\theta_W[(W_\mu^\dagger W_\nu - W_\nu^\dagger W_\mu)\partial^\mu Z^\nu \\
&+ (\partial_\mu W_\nu - \partial_\nu W_\mu)W^{\dagger\nu} Z^\mu - (\partial_\mu W_\nu^\dagger - \partial_\nu W_\mu^\dagger)W^\nu Z^\mu] \\
&+ ie[(W_\mu^\dagger W_\nu - W_\nu^\dagger W_\mu)\partial^\mu A^\nu \\
&+ (\partial_\mu W_\nu - \partial_\nu W_\mu)W^{\dagger\nu} A^\mu - (\partial_\mu W_\nu^\dagger - \partial_\nu W_\mu^\dagger)W^\nu A^\mu] \\
&+ g^2\cos^2\theta_W(W_\mu W_\nu^\dagger Z^\mu Z^\nu - W_\nu W^{\dagger\nu} Z_\mu Z^\mu) \\
&+ e^2(W_\mu W_\nu^\dagger A^\mu A^\nu - W_\nu W^{\dagger\nu} A_\mu A^\mu) \\
&+ eg\cos\theta_W[W_\mu W_\nu^\dagger(Z^\mu A^\nu + A^\mu Z^\nu) - 2W_\nu W^{\dagger\nu} A_\mu Z^\mu] \\
&+ \frac{1}{2}g^2 W_\mu^\dagger W_\nu(W^{\dagger\mu}W^\nu - W^\mu W^{\dagger\nu}) \ .
\end{aligned} \tag{7}$$

In equation (7), there are all possible interactions between the gauge bosons allowed in the SM. Lines 1 and 2 represent the $W^\dagger WZ$ interaction, lines 3 and 4 the $W^\dagger WA$ interaction, line 5 the $W^\dagger WZZ$ interaction, line 6 the $W^\dagger WAA$ interaction, line 7 the $W^\dagger WAZ$ interaction and line 8 the $W^\dagger WW^\dagger W$ interaction.

Figure 1 - Main interactions for a process $\gamma\gamma \to WW$.

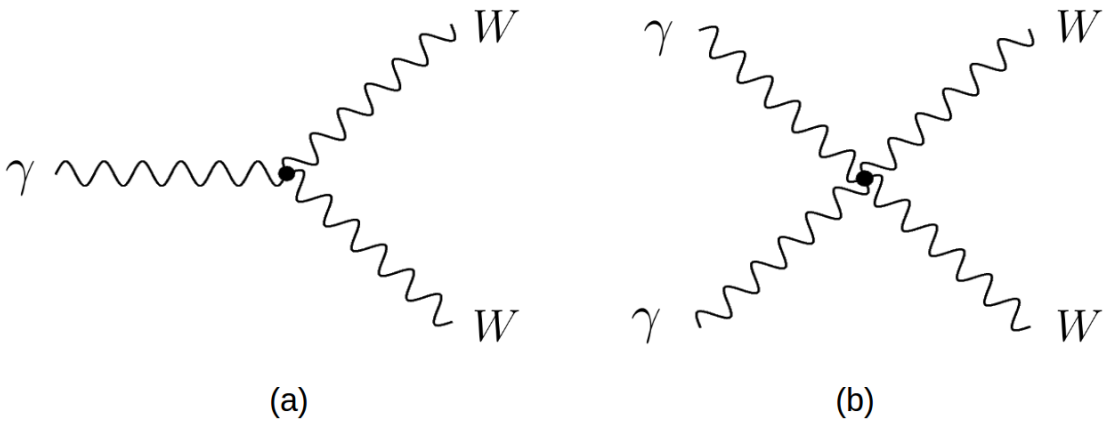

Subtitle: Diagrams for $W^{\dagger}WA$ interaction (left) and $W^{\dagger}WAA$ interaction (right).
Source: The author, 2019.

On this thesis, the focus is the process that produces W pairs from photon exchange. At leading order (LO), the interactions are of the types $W^{\dagger}WA$ and $W^{\dagger}WAA$. In figure 1, the diagrams representing these interactions are shown.

The diagram in figure 1 (b) already represents a process $\gamma\gamma \to WW$, the vertex of this kind of process is called Quartic Gauge Coupling (QGC). The diagram in figure 1 (a) does not represent a physical process itself, but one of the vertices in a $\gamma\gamma \to WW$ process. The vertex is called Triple Gauge Coupling (TGC). The physical process, at leading order, with TGC is represented in figure 2. At LO, the Standard Model describes the process $\gamma\gamma \to WW$ completely with QGC and TGC using the diagrams in figure 2 or figure 1 (b).

1.2 **Beyond Standard Model**

So far the Standard Model seems quite good. It can describe three of the four fundamental interactions, the fundamental constituents of the matter and the interaction particles. All the Standard Model particles have been detected over the years and the model has been successful in a large variety of experimental tests.

On the other hand, the Standard Model is incomplete. For example, it does not include the gravitational interaction, and cannot explain several fundamental phenomena like dark matter and neutrino oscillations, or even questions about the model itself such as: why the $SU(3)_{color} \times SU(2)_{isospin} \times U(1)_{hypercharge}$ symmetry? why this kind of repre-

Figure 2 - Process $\gamma\gamma \to WW$ with TGC.

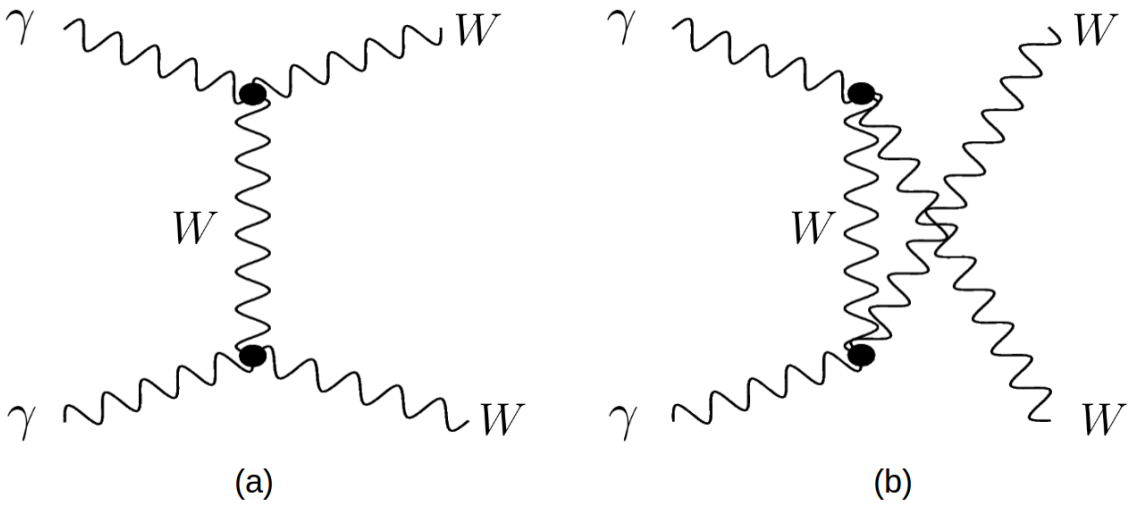

Subtitle: Diagrams for the process $\gamma\gamma \to WW$ with TGC. t-channel (left) and u-channel (right).
Source: The author, 2019.

sentation?

To try to answer these and other questions or explain other aspects, a large number of extended models have been proposed over time, classified as Beyond Standard Model (BSM), such as Warped Extra Dimensions (RANDALL; SUNDRUM, 1999), Supersymmetry (MARTIN, 1998), Grand Unification Theory (LANGACKER, 1981) and many others. This thesis will focus on some aspects of a technique to estimate the effect of any extension to the SM at measurable energy scale, the Effective Field Theory.

1.2.1 Effective Field Theory and Anomalous Gauge Couplings

To build a new and more general theory one of the most important things is to reproduce the current experimental results within appropriate limits. In the High Energy Physics case, to recover the Standard Model and to respect its generalities as a gauge symmetry. The Effective Field Theory approach is very useful to do it.

The Lagrangian for any high energy theory can be written as:

$$\mathcal{L}_{eff} = \mathcal{L}_{SM}^{(4)} + \sum_i \frac{c_i^{(6)}}{\Lambda^2}\mathcal{O}_i^{(6)} + \sum_j \frac{c_j^{(8)}}{\Lambda^4}\mathcal{O}_j^{(8)} + \ldots + \sum_j \frac{c_j^{(n)}}{\Lambda^{n-4}}\mathcal{O}_j^{(n)} + \ldots , \tag{8}$$

where $\mathcal{L}_{SM}^{(4)}$ is the Standard Model Lagrangian density, $\mathcal{O}_i^{(n)}$ are the operators of dimension n, Λ is a new energy scale introduced to correct the Lagrangian dimension and the

coefficients $c_i^{(n)}$ are a parameterization of the strength of the new physics couplings. The sum over n is infinite and it should admit only even numbers, as the odd-dimensional operators do not conserve lepton and baryon numbers.

The scope of this thesis is related to some aspects of the dimension-six operators. According to the equation (8) is possible to identify the dimension-six Lagrangian density as:

$$\mathcal{L}^{(6)} = \sum_i \frac{c_i^{(6)}}{\Lambda^2} \mathcal{O}_i^{(6)} \ . \tag{9}$$

Imposing the $SU(3) \times SU(2) \times U(1)$ invariance, Buchmuller and collaborators (BUCHMULLER; WYLER, 1986) found 80 independent operators $\mathcal{O}_i^{(6)}$ and assuming baryon number conservation Grzadkowski and collaborators (GRZADKOWSKI et al., 2010) could find 59. For the process $\gamma\gamma \to WW$ represented on the figure 1 (b) with QGC, Belanger and collaborators (BéLANGER; BOUDJEMA, 1992) found two operators given by the following Lagrangian densities,

$$\mathcal{L}_0^{(6)} = \frac{-e^2}{8} \frac{\alpha_0}{\Lambda^2} F_{\mu\nu} F^{\mu\nu} W^\alpha W_\alpha^\dagger \tag{10}$$

and

$$\mathcal{L}_C^{(6)} = \frac{-e^2}{8} \frac{\alpha_C}{\Lambda^2} F_{\mu\alpha} F^{\mu\beta} (W^\alpha W_\beta^\dagger + W^{\dagger\alpha} W_\beta) \ . \tag{11}$$

The values α_C/Λ^2 and α_0/Λ^2 parameterize the process of the diagram on figure 1 (b) in the Effective Field Theory (EFT) dimension-six scenario. The parameters α_C and α_0 are called *anomalous Quartic Gauge Couplings* (aQGCs). The interaction represented on the figure 1 (a), is described by the following Lagrangian density,

$$\mathcal{L}_{\lambda^\gamma}^{(6)} = -ie \frac{\lambda^\gamma}{M_W^2} F^{\mu\nu} W_{\mu\alpha}^\dagger W_\nu^\alpha \ , \tag{12}$$

where λ^γ is the anomalous Triple Gauge Coupling (aTGC). In this thesis, only the aQGCs were considered since the diagram in figure 1 (b) has a lower order cross section than the diagrams in figure 2.

When any of the aQGCs are considered non-zero, the cross section of the $\gamma\gamma \to WW$ process increases very fast with the aQGCs parameters, which implies a possible unitarity violation. The cross section can be regulated using a form factor that provides a suppression of the aQGCs effect at high center-of-mass energy. Following (PIERZCHAłA; PIOTRZKOWSKI, 2008), the form factor can be written as

$$\frac{\alpha_{0,C}}{\Lambda^2} \to \frac{\alpha_{0,C}}{\Lambda^2} \frac{1}{(1 + (\frac{s_{\gamma\gamma}}{\Lambda_{cutoff}})^2)^2} \ , \tag{13}$$

where $s_{\gamma\gamma}$ is the invariant center-of-mass energy of the photon exchange process and Λ_{cutoff}

Figure 3 - α_C/Λ^2 and α_0/Λ^2 experimental limits.

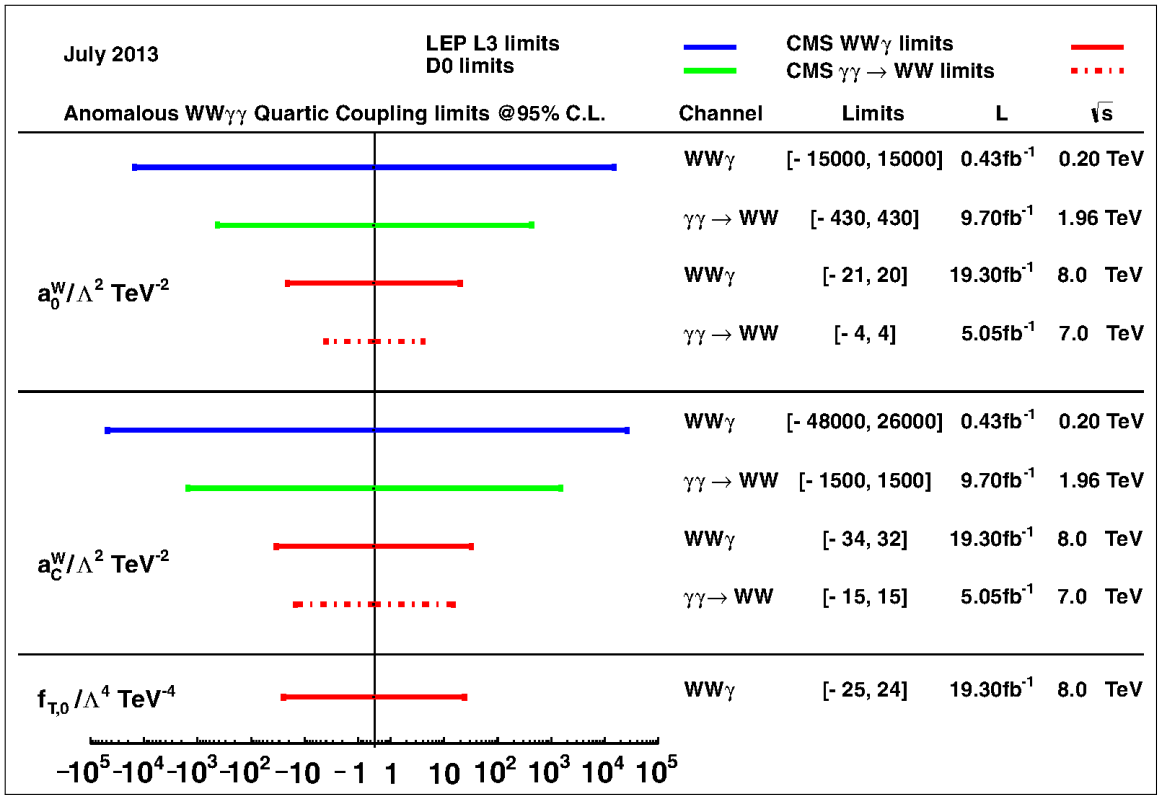

Subtitle: aQGCs limits at 95% C.L. from LEP L3, D0 and CMS collaborations. It is not considered form factors.

Source: CMS COLLABORATION., 2018c.

is the scale of new physics, where EFT is no longer valid. For the analysis presented in this thesis, simulated samples without form factor and with form factor using $\Lambda_{cutoff} = 500$ GeV were considered, to compare with the results of previous measurements at the LHC (CMS COLLABORATION, 2016a) and (ATLAS COLLABORATION, 2016).

1.2.2 Experimental exclusion limits

Various searches for physics beyond Standard Model have been performed by many experiments, especially the study of aQGCs in the EFT context has been made by the L3 Collaboration — at LEP — (ACHARD et al., 2002), D0 — at Fermilab — (D0 COLLABORATION, 2013) and recently the CMS and ATLAS collaborations (CMS COLLABORATION, 2016a) and (ATLAS COLLABORATION, 2016) respectively. Figure 3 presents a comparison of the results, at 95% of confidence level from CMS, L3 and D0 collaborations.

The results in figure 3 were taken in a formalism where $SU(2)_{isospin} \times U(1)_{hypercharge}$

is respected without a Standard Model Higgs boson. If a formalism with the Standard Model Higgs boson is considered, the limits obtained for CMS and ATLAS collaborations are modified as listed in table 2.

1.3 **Proton-proton collision and Central Exclusive Production**

One of the cleanest ways to investigate the Standard Model and beyond at high energy is through particle collisions experiments. The LHC, the most powerful particle accelerator nowadays, accelerates protons with an energy of 6.5 TeV (13 TeV center-of-mass system) and collides them in four interaction points (IP) where the detectors are installed. A collision consists of the interaction of a constituent from proton p_1 with a constituent of another proton p_2.

A considerable fraction of the collisions happen by photon exchange, therefore the LHC can be also considered a photon-photon collider. In some of these collisions, the two protons remain intact after losing a fraction of their energy. This special kind of process is called Central Exclusive Production (CEP). Figure 4 shows a representation of CEP process, where the final state has two intact protons p_1' and p_2', a central object X and rapidity gaps (regions of rapidity without particles).

The fractional momentum loss of the proton (ξ) is defined by,

$$\xi_1 = 1 - \frac{|\mathbf{p}_1'|}{|\mathbf{p}_1|} \qquad and \qquad \xi_2 = 1 - \frac{|\mathbf{p}_2'|}{|\mathbf{p}_2|} \ , \tag{14}$$

where $\mathbf{p}$ ($\mathbf{p}'$) denotes the momentum of the proton before (after) the collision. The mass of the central object X can be reconstructed as

$$M_X = \sqrt{s\xi_1\xi_2} \ , \tag{15}$$

where $\sqrt{s}$ is the center-of-mass energy. The rapidity of the object X can be written as

$$y_X = \frac{1}{2}\ln\left(\frac{\xi_1}{\xi_2}\right) \ . \tag{16}$$

These variables (M_X and y_X) are extremely important to correlate the proton information with the central object information.

Table 2 - Latest limits established for the aQGC parameters.

aQGC parameter	ATLAS (GeV^{-2})	CMS (GeV^{-2})
α_0/Λ^2 (no form factor)	$-1.7 \times 10^{-6} < \alpha_0/\Lambda^2 < 1.7 \times 10^{-6}$	$-1.1 \times 10^{-6} < \alpha_0/\Lambda^2 < 1.1 \times 10^{-6}$
α_C/Λ^2 (no form factor)	$-6.4 \times 10^{-6} < \alpha_C/\Lambda^2 < 6.3 \times 10^{-6}$	$-4.1 \times 10^{-6} < \alpha_C/\Lambda^2 < 4.1 \times 10^{-6}$
α_0/Λ^2 ($\Lambda_{cutoff} = 500$ GeV)	$-0.96 \times 10^{-4} < \alpha_0/\Lambda^2 < 0.93 \times 10^{-4}$	$-0.9 \times 10^{-4} < \alpha_0/\Lambda^2 < 0.9 \times 10^{-4}$
α_C/Λ^2 ($\Lambda_{cutoff} = 500$ GeV)	$-3.5 \times 10^{-4} < \alpha_C/\Lambda^2 < 3.3 \times 10^{-4}$	$-3.6 \times 10^{-4} < \alpha_C/\Lambda^2 < 3.0 \times 10^{-4}$

Subtitle: Limits established for the aQGC parameters obtained for the CMS (CMS COLLABORATION, 2016a) and ATLAS (ATLAS COLLABORATION, 2016) collaborations.

Source: The author, 2019.

Figure 4 - Diagram of a CEP process.

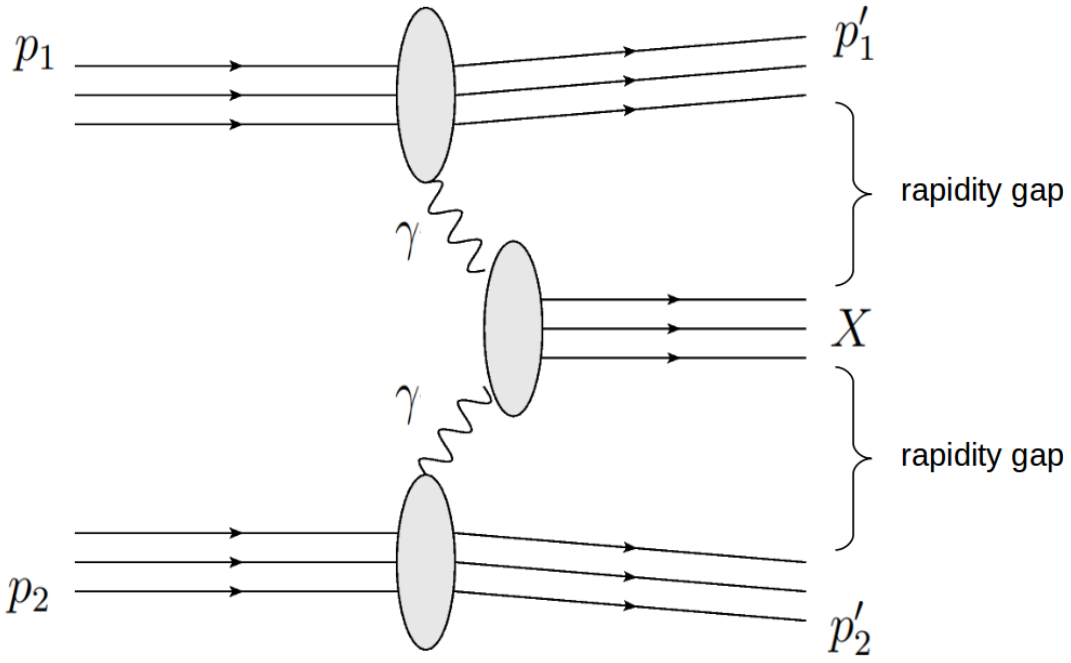

Subtitle: CEP process by γ exchange with two protons and a central object X in the final state.
Source: The author, 2019.

Table 3 - The branching ratio of the WW decays.

Channel	Breaching ratio
$\mu^+\mu^-$	1.17%
e^+e^-	1.17%
$e^\mp\mu^\pm$	2.34%
$\mu^\pm\ q_1q_2$	14.53%
$e^\pm\ q_1q_2$	14.53%
Fully hadronic	45.43%

Subtitle: The Branching ratio of the WW decays. The values were calculated for the single W branching ratio extracted from (BERINGER et al., 2012).

Source: The author, 2019.

1.4 Central Exclusive Production of WW in the anomalous couplings context

The search of the anomalous couplings γWW and $\gamma\gamma WW$ signature over the huge background of the W pair production has the CEP as an ideal topology to do it. In previous analyses at the LHC — (CMS COLLABORATION, 2013), (CMS COLLABORATION, 2016a) and (ATLAS COLLABORATION, 2016) — it was investigated this possibility by looking for the rapidity gaps in the detector. In 2016 the LHC was operating in a high average number of collisions per bunch crossing scheme that makes it harder to look for rapidity gaps in the detector. The solution to still look for CEP processes is to detect the scattered protons and match the proton information with the WW information measured at the central detector.

The goal of this thesis is to study the viability of W pair production in the CEP topology using the semileptonic channel as a way to explore small values of anomalous quartic couplings parameters (α_C/Λ^2 and α_0/Λ^2). The semileptonic channel consists of one W decaying into a lepton (l) and a neutrino ($\bar{\nu_l}$) and the other W decaying into a quark pair (q_1 and q_2), forming jets, as is represented by the diagram of figure 5. In this thesis, only the case when the lepton is a muon was studied.

Smaller values of α_C/Λ^2 and α_0/Λ^2 are related to smaller cross sections for the process, then the semileptonic channel was chosen since the branching ratio is larger than the fully leptonic channel, as can be seen in the table (3). The fully hadronic channel (only quarks in the final state) may look like a better choice, but the QCD background would be extremely high making it a very difficult channel to study.

For this process, the background is dominated by the inclusive production of a W boson in association with jets ($W + jets$). Other important backgrounds are the production of $t\bar{t}$ and the single production of the quark t.

Figure 5 - Diagram of a WW production in the CEP topology.

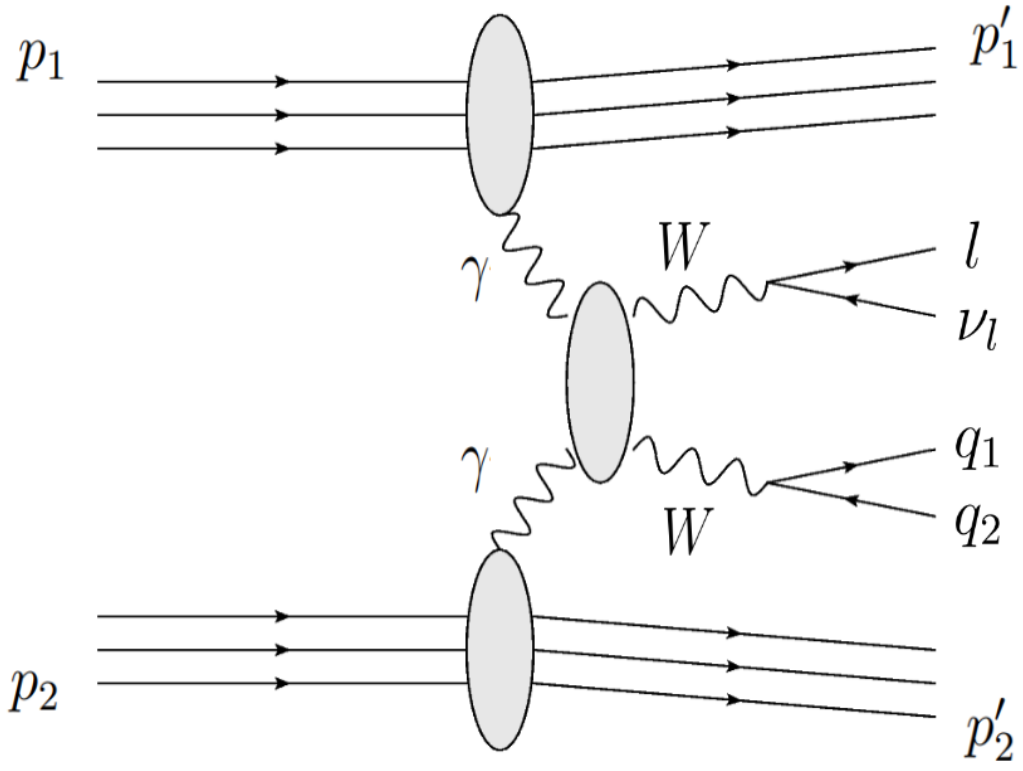

Subtitle: CEP process by γ exchange with two protons in the final state and a W pair decaying in the semileptonic channel.

Source: The author, 2019.

2 EXPERIMENTAL SETUP

In order to perform the current experimental aQGCs study, it was used data from proton-proton collisions at 13 TeV taken in 2016 by the Compact Muon Solenoid Experiment located at the Large Hadron Collider complex at CERN. The scattered protons were detected by the subdetector Precision Proton Spectrometer, which was built and operated by CMS and TOTEM collaborations together. This chapter will present a brief introduction about CMS and PPS, a detailed description can be found in (CMS COLLABORATION, 2008) and (ALBROW et al., 2014) respectively.

The CERN — European Organization for Nuclear Research — is an international scientific organization with country members (founding members, associate members, observers and countries with cooperation agreements) around the world. Its main purpose is the particle physics investigation. Since its creation in 1954, CERN experiments were responsible for numerous discoveries and technological breakthrough, as the most important achievements it is possible to highlight the W and Z discovery in 1983 at UA1 and UA2 experiments (LOCCI, 1986), the determination of the number of light neutrino families in 1989 at LEP (ALEPH COLLABORATION, 1990) and Higgs boson discovery in 2012 at the LHC (ATLAS COLLABORATION, 2012) and (CMS COLLABORATION, 2012).

2.1 The Large Hadron Collider

The LHC is the largest and most powerful particle collider in the world, it is located at the Swiss-French border in the underground at a depth varying between 50 m and 170 m. It is composed of a dual circular ring with a circumference of ~ 26.7 km. The tunnel was excavated in the 80s for the Large Electron-Positron Collider (LEP) and the LHC was built between 1998 and 2008.

To deliver the protons to the LHC machine, they pass through a set of accelerator stages. The protons come from the ionization of hydrogen atoms, at LINAC2 these protons are accelerated until the energy of 50 MeV with radio frequency quadrupoles (RFQ). The next stage is the Proton Synchrotron Booster (PSB), where there are a set of four synchrotron rings that raise the proton energy to 1.4 GeV. After the PSB, the protons are introduced into a synchrotron with a circumference of 600 m, the Proton Synchrotron (PS), where the energy increases to 25 GeV. The last stage before LHC is the Super Proton Synchrotron (SPS), where the protons are accelerated up to 450 GeV. In figure 6 there is a description of the accelerator stages. All these accelerators were previously used for different researches, as for example, the PS which started its operation in 1959 and where the Gargamelle Experiment discovered the neutral currents from a neutrino beam

Figure 6 - The LHC scheme.

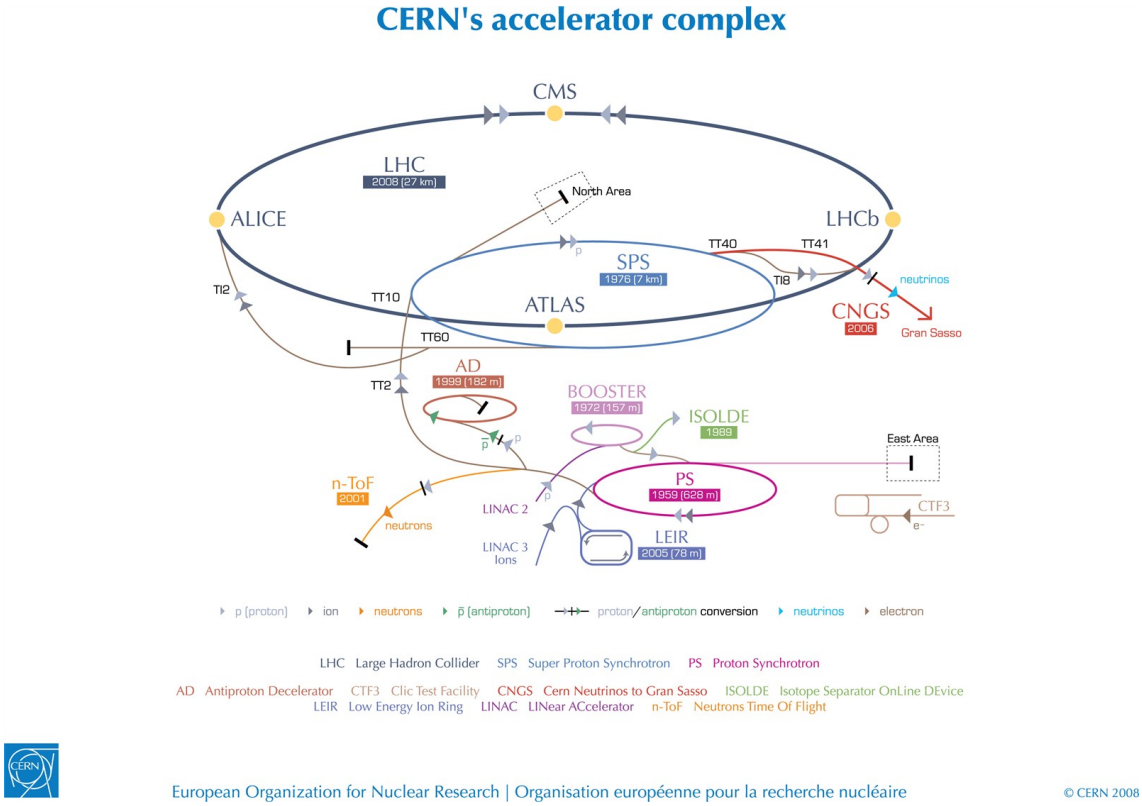

Subtitle: The CERN accelerator scheme till the LHC injection beam.
Source: CERN, 2008.

produced by the PS proton beam (GARGAMELLE NEUTRINO COLLABORATION, 1973).

In the LHC, the protons are accelerated with a complex system of magnets that include 1232 dipoles cooled to 1.9 K and able to produce a magnetic field of 8.33 T. Also a set of magnet quadrupoles are used for beam focusing and squeezing, to apply corrections.

When the protons arrive at the LHC, they are divided into two opposite beams with the protons separated in 2808 bunches with 1.15×10^{11} protons. Each bunch is separated from the next one by 25 ns. A bunch of one beam collides with a bunch of the other with frequency (f_c) of 40 MHz. Taking into account the number of protons per bunch (n_b), it means around 1 billion of proton interactions per second. The average number of proton collision per bunch crossing is called pileup. It results in an instantaneous luminosity of 10^{34} cm^{-2}s^{-1}. The numbers mentioned here are the nominal ones, because of the many technological challenges, the accelerator could not perform the collisions with exactly these parameters. In table 4, these values are shown for different periods of data taking.

The LHC is also able to accelerate and collide heavy ions. There were some periods of data taking with proton-lead, lead-lead collisions and recently xenon-xenon collisions.

Table 4 - LHC technical parameters.

		Run I			Run II		
	Nominal	2010	2011	2012	2015	2016	2017
Center-of-mass energy (TeV)	14	7	7	8	13	13	13
Maximum $\mathcal{L}_{inst}$ ($cm^{-2}s^{-1}$)	1×10^{34}	2×10^{32}	3.5×10^{33}	7.7×10^{33}	5.2×10^{33}	1.53×10^{34}	2.09×10^{34}
f_c (MHz)	40	20	20	20	40	40	40
Maximum n_b	1.15×10^{11}	1.2×10^{11}	1.5×10^{11}	1.7×10^{11}	1.15×10^{11}	1.25×10^{11}	1.25×10^{11}
Maximum N_b	2808	348	1331	1368	2232	2208	2556
Bunch spacing (ns)	150	50	50	50	25	25	25

Subtitle: Technical parameters for proton-proton collisions for nominal, Run I and Run II conditions.

Source: The author, 2019.

Figure 7 - The luminosity delivered to CMS.

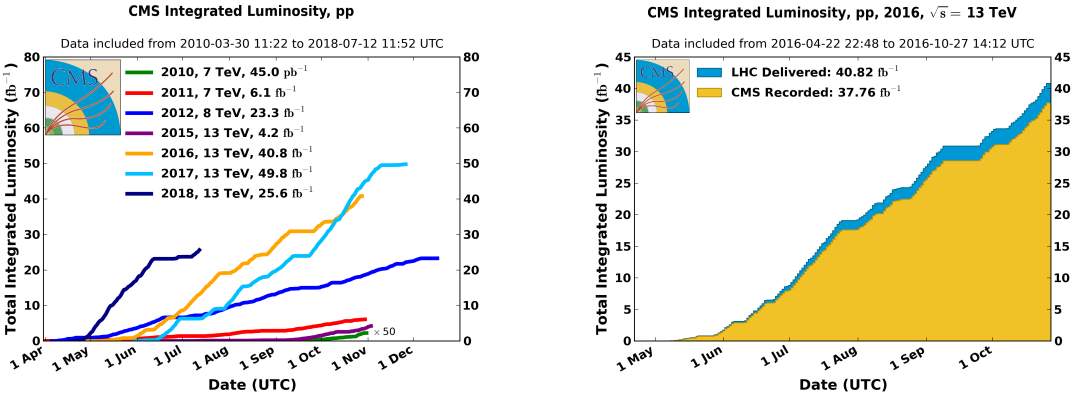

Subtitle: The integrated luminosity delivered to CMS by the LHC from 2010 to 2018 (left) and the comparison between the delivered and recorded luminosity for 2016 (right).

Source: CMS COLLABORATION, 2018b.

All the heavy ion collisions were conducted with lower energy than the proton-proton collisions. Although the photon-photon interaction is very interesting in heavy ion collisions, the scope of this thesis is only the proton-proton collisions.

The first collision in the LHC was in November 2009 with a 900 GeV center-of-mass energy. At the end of the same year, the LHC was colliding protons at an energy of 2.36 TeV and in 2010 started the data taking period called Run I, with 7 TeV center-of-mass energy for proton-proton collisions. The Run I comprises the period from 2010 to 2012, in this data taking the LHC experiments could discover the Higgs Boson. After the shutdown in 2013 and 2014, the LHC started another data taking period, called Run II, in 2015 and ended in 2018. In the whole period, the proton-proton collisions were done at 13 TeV. In figure 7 it is presented the integrated luminosity recorded by CMS experiment from 2010 to July 2018 and the integrated luminosity delivered by LHC to CMS in 2016.

2.1.1 LHC experiments

The LHC can collide particles in four different points of the ring, at Points 1, 2, 5 and 8 where there are caverns with the detectors. They are able to detect particles produced in the collisions using different kind of technologies. The experiments are:

- **ALICE**: **A** **L**arge **I**on **C**ollider **E**xperiment (ALICE COLLABORATION, 2008) is located at Point 2 and dedicated to characterizing heavy ion and proton-ion collisions. The main objective is the study of the quark-gluon plasma, a new state of matter, that appears in the high densities regimes and which is important to understand the early moments of the Universe.

- **ATLAS**: **A** **T**oroidal **L**HC **A**pparatu**s** (ATLAS COLLABORATION, 2008) is located at Point 1 and it is a general-purpose detector with a toroid and a solenoid set that can produce 2 T of magnetic field at the interaction point. It is the largest detector at LHC with a diameter of 25 m and a length of 44 m.

- **CMS**: **C**ompact **M**uon **S**olenoid is located at Point 5, it is also a general-purpose detector. It will be discussed in more details in the next section.

- **LHCb**: **LHC-b**eauty (LHCB COLLABORATION, 2008) is located at Point 8. It is a single-arm spectrometer with a very precise tracking system dedicated to study the properties of the b quark.

- **LHCf**: **LHC-f**orward (LHCF COLLABORATION, 2008) is located at the forward region in both sides of the ATLAS detector. The aim is the study of the π^0 energy and multiplicity produced by the collisions.

- **MoEDAL**: **Mo**nopole and **E**xotics **D**etector **A**t the **L**HC (PINFOLD, 2015) shares the cavern with LHCb detector. This experiment searches for magnetic monopoles.

- **TOTEM**: **TOT**al **E**lastic and Diffractive Cross Section **M**easurement (TOTEM COLLABORATION, 2008) is located at the forward region in both sides of the CMS detector. The goal of TOTEM is the measurement of the total cross section, elastic scattering, diffractive processes, and exclusive process.

2.2 Compact Muon Solenoid

The CMS experiment is a cylindrical detector coaxial with the LHC beam direction distributed in a length of 21.5 m, a diameter of 15 m and with a weight of around 14 kton. It can be divided in the barrel region (the body of the cylinder) and the endcap region (the disks that close the cylinder). The detector is composed basically by a large superconducting solenoid and a set of subdetectors. The solenoid provides 3.8 T magnetic field inside the detector and pointing in the direction of the beam, that allows the compact design of the detector. In figure 8 it is presented a schematic representation of the detector.

The CMS coordinate system is centered in the nominal LHC interaction point with the z-axis in the direction of the anticlockwise beam, the x-axis pointing to the center of the LHC ring and the y-axis in the upward direction. In the x-y plane, there are the azimuth angle ϕ and the radial coordinate r. From z-axis there is the polar angle θ, which is correlated with the pseudorapidity η by $\eta = -\ln[\tan(\theta/2)]$.

The following sections will be dedicated to discuss the CMS subdetectors, the trigger system, and the object reconstruction.

Figure 8 - The CMS scheme.

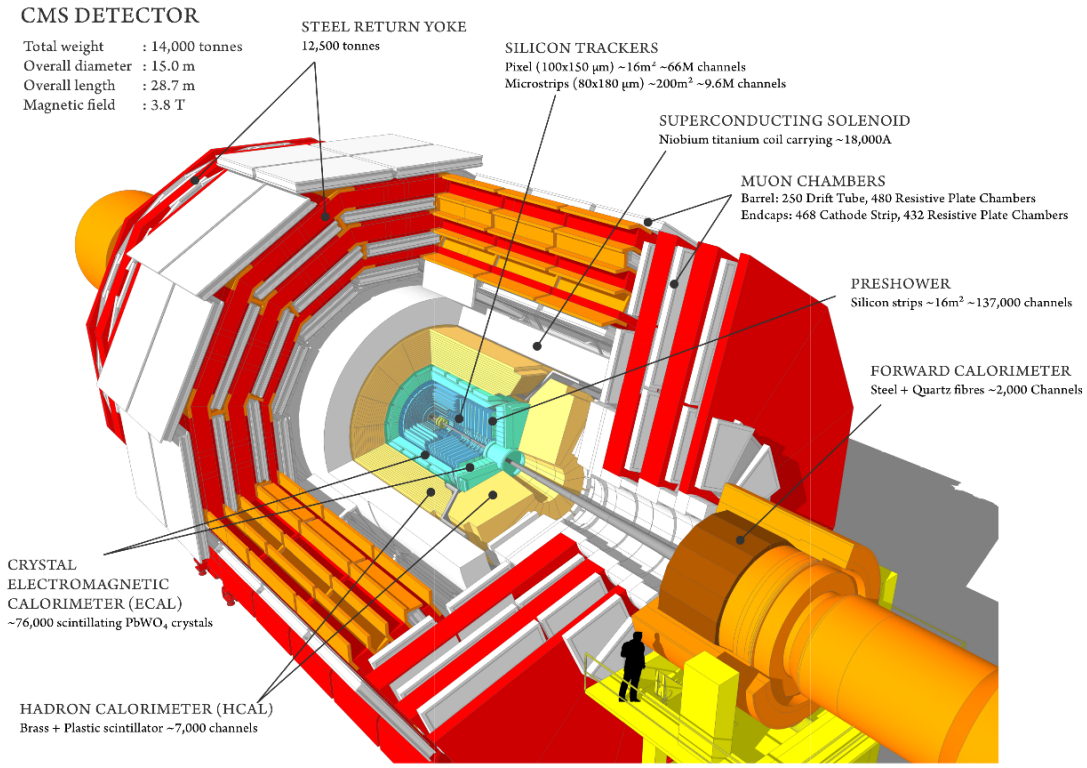

Subtitle: The design of the CMS experiment.

Source: CMS COLLABORATION, 2018a.

2.2.1 Subdetectors

The CMS experiment is composed of a set of subdetectors that make possible the reconstruction of the physics objects. In figure 10 there is a representation of a slice of the CMS detector, in the innermost part, there is the Tracking System that is able to characterize all charged particles (muons, electrons, and charged hadrons). After, the Electromagnetic Calorimeter (ECAL), which is used to measure the electron and photon energy deposit. Between the ECAL and the Superconducting Solenoid, the Hadron Calorimeter (HCAL), where the hadrons (charged and neutral) deposit their energy. In the outer layer, it is placed the Muon System, to characterize the muons.

A new subdetector started to operate in CMS in 2015 for tests and 2016 collecting data, the Precision Proton Spectrometer. It is situated around 210 m from the CMS IP, close to the beam, in both sides of the central detector. The goal of this subdetector is detecting the protons scattered in the IP. It will be discussed in more detail in a next section.

2.2.1.1 Tracking System

The CMS Tracker is responsible for the measurement with high precision of the charged particle curved trajectories and consequently the reconstruction of the primary and secondary vertex positions, as well as the charged particles transverse momentum. The detector covers a sensitive area of 200 m^2, it is composed of silicon sensors and has the region of acceptance in $|\eta| < 2.5$. It has many detecting layers, this is important because it reduces the ambiguity of the reconstruction of a track, and it has a low amount of material, which is important to decrease the probability of particle multiple scattering.

Two subdetectors compose the Tracking system in different regions and with different kind of sensors, they are:

- **Silicon Pixel System**: The innermost subdetector, with 66 million $100\mu m \times 150\mu m$ pixels sensors covering an area of $1.1m^2$. It is divided into three cylindrical layers (barrel region) plus two disks (in each side, endcap regions). The layers are in a radial distance of the IP of $4.3cm$, $7.2cm$ and $11cm$. The disks are located $34.cm$ and $46.5cm$ away from the IP.

- **Silicon Strip System**: This subdetector wraps the pixel one covering an area of $193m^2$ and it is composed of more than 9 million strips. It is composed by 10 layers and 12 disks divided into four parts: 6 layers in The Outer Barrel (TOB), 4 layers in The Inner Barrel (TIB), 3 Tracker Inner Disks (TID) inside the TOB and 9 Tracker Endcaps (TEC) outside the TOB. The barrel region covers a radius between $25cm$

Figure 9 - The CMS object reconstruction scheme.

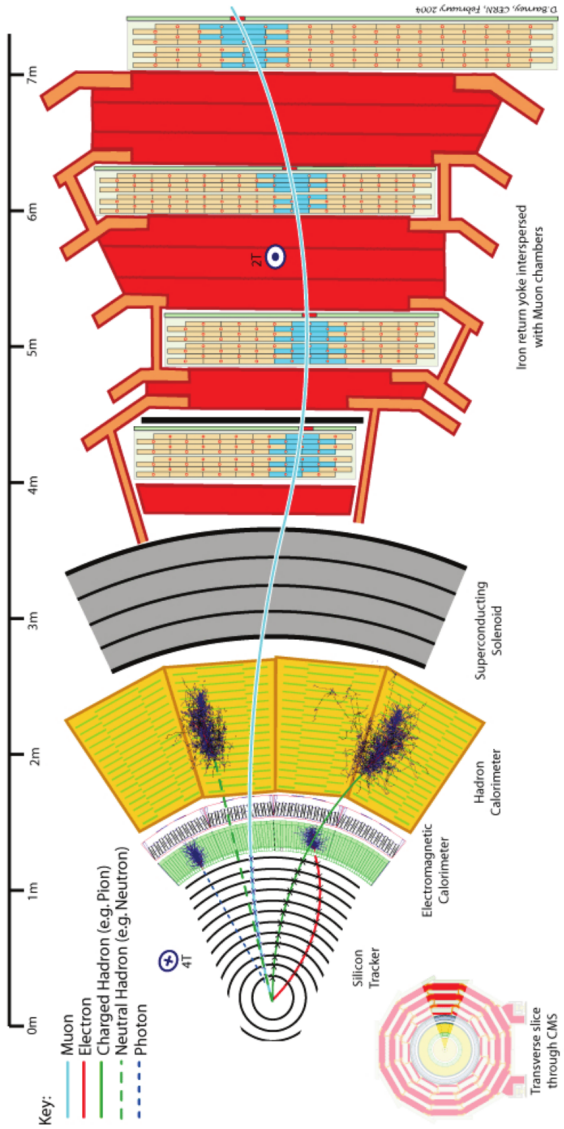

Subtitle: A drawing of a slice of the CMS with the subdetectors and the reconstructed particles trajectories.

Source: BEHN, 2014.

Figure 10 - The CMS Tracking System layout.

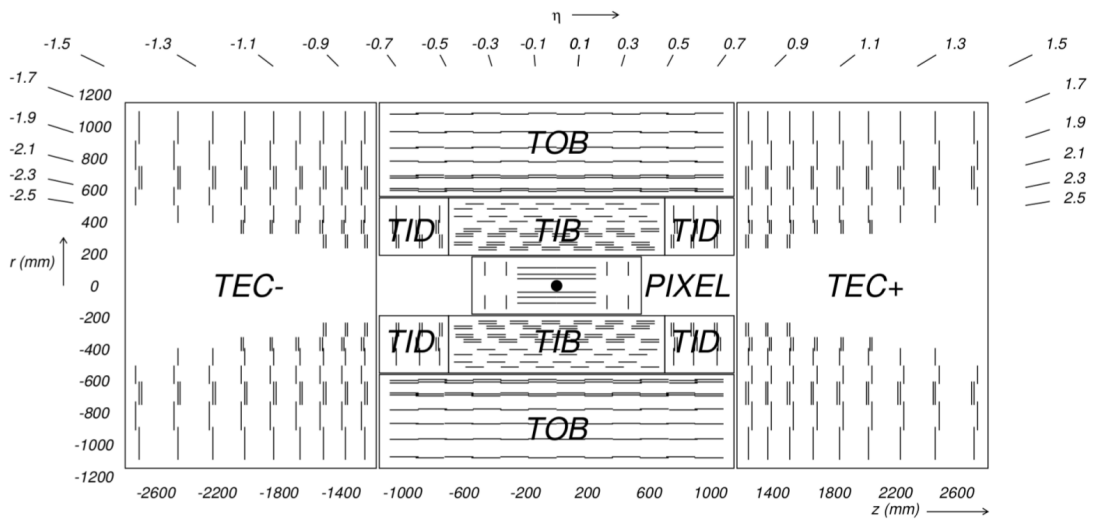

Subtitle: The layout of the Tracking System with all subsystems.

Source: Figure extracted from CMS COLLABORATION, 2008, p. S08004.

and 110cm and the TEC covers a z region between 120cm and 280cm.

In figure 10 it is presented a schematic cross section of the CMS Tracking System with z and η acceptance. The tracker has also a complete azimuthal (ϕ coordinate) acceptance.

2.2.1.2 ECAL

The detection of the electrons and photons is made in the CMS ECAL by the absorption and measurement of their energy deposition in the scintillating crystals. When a photon penetrates the ECAL it interacts with the scintillator material and produces an electron-positron pair which can produce photons again by Bremsstrahlung process. The same process can occur when an electron penetrates the ECAL. Then the scintillated photons are collected.

The ECAL has 75848 crystals, which are made of lead tungstate ($PbWO_4$) that provides a fast scintillation decay time. The crystals are divided into two different regions, the barrel and the endcaps. In addition, there are preshower calorimeters placed in front of the ECAL endcaps.

- **Barrel**: It is composed by 61200 crystals located in an inner radius of 129 cm and divided in 36 "supermodules" (20 crystals in ϕ direction $\times$ 85 crystals in η direction). Each crystal has a trapezoidal shape with 22 $\times$ 22 mm^2 of front area and 26 $\times$ 26

Figure 11 - The CMS ECAL scheme.

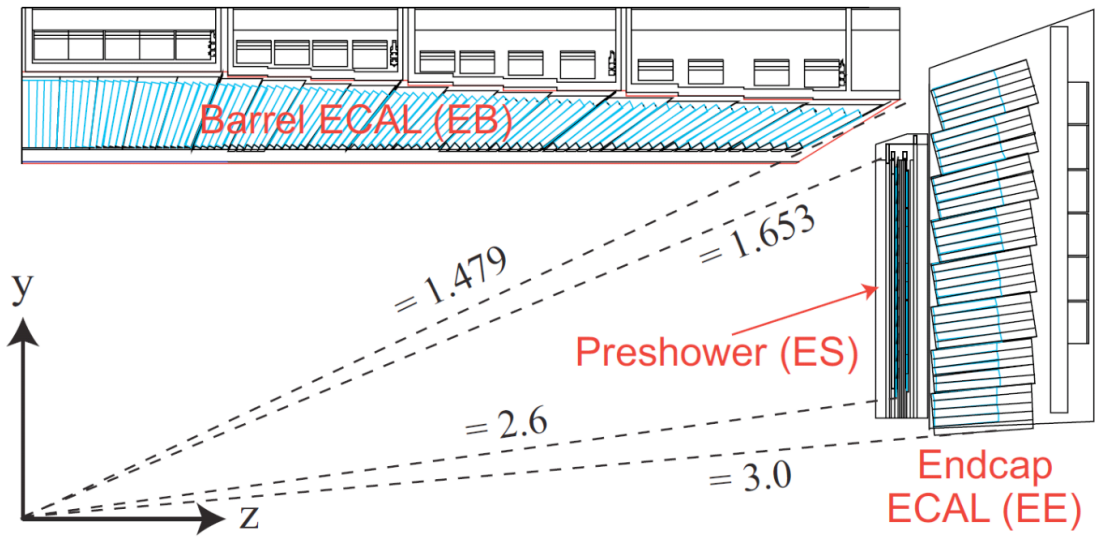

Subtitle: The layout of a ECAL cross section.

Source: Figure extracted from BENAGLIA, 2014, p. 2.

mm^2 of rear area. The length of each crystal is 230 mm. The barrel ECAL area covers a pseudorapidity region of $|\eta| < 1.48$.

- **Endcaps**: They are composed by 7324 crystals in total, located at 314 cm far from the IP (both sides) and divided in 5×5 crystal units (the "supercrystals"). Each crystal has a trapezoidal shape with 28.6×28.6 mm^2 of front area and 30×30 mm^2 of the rear area. The length of each crystal is 220 mm. The endcap ECAL area covers a pseudorapidity region of $1.479 < |\eta| < 3.0$.

- **Preshowers**: They are composed of two layers of a lead radiator to initiate the shower in front of a set of silicon strip sensors to measure the deposited energy of the shower. They are located in front of both endcaps and were designed to identify the neutral pions decay into two photons and separate them from the primary photons. Currently, the energy in the preshowers is just included in the closest ECAL crystals. It has an acceptance in the region of $1.653 < |\eta| < 2.6$.

Figure 11 shows a schematic cross section of the CMS ECAL with η acceptance for each part of the system.

2.2.1.3 HCAL

Surrounding the ECAL is located the hadronic calorimeter, with the goal to measure the energy of the jets, produced in the collisions, and to help in the photon and lepton identification. The HCAL is composed of plastic scintillator tiles and layers of steel and brass. When hadrons penetrate the HCAL they interact with the layers producing showers that are detected by the scintillators.

The HCAL has a η acceptance of $|\eta| <\sim 5$. As the previous subdetectors, HCAL is also divided into different parts: the HCAL Barrel (HB), the Outer Calorimeter (HO) (both in the barrel region), the HCAL Endcaps (HE) and Forward Calorimeters (HF) in the forward region.

- **HB**: It is the inner part at $r = 1.78$ m and is surrounded by the superconducting solenoid. It is composed by 36 wedges covering the region of $|\eta| < 1.4$. It has 17 scintillator tile layers interleaved with steel and brass.

- **HO**: It is located outside the solenoid and it is used to identify late starting showers. It is important to measure the deposited energy after the HB. It covers the region of $|\eta| < 1.26$.

- **HE**: It is placed in the CMS endcap region (in both sides), it covers a region of $1.3 < |\eta| < 3.0$. It is made by 18 layers of brass and the plastic scintillator. Around 34% of the produced particles in the collisions cross the HE.

- **HF**: It is located in the frontal region at 10.9 m away from the IP (in both sides), it covers a pseudorapidity up to $|\eta| = 5$. It consists of different layers of steel and quartz fibers. The HF is able to distinguish electron and photon showers from hadron showers.

In figure 12, there is a CMS longitudinal view with the different parts of the HCAL.

2.2.1.4 Muon Chambers

Finally the outermost subdetector system, the Muon Chambers. They are located in the outer layers of CMS, however, the muons detection are not harmed due to their small loss of energy in the trajectory through the whole inner system. It starts at $r \sim 4$ m (in the barrel region) and is composed basically by gaseous detectors. The goal of this subdetector is to detect the muons and together with the Tracking System, reconstruct their trajectories and transverse momentum with a good resolution.

Different pseudorapidity regions have different muon flux which demonstrates the need of use different kinds of detector materials. There are three kinds of muon chambers

Figure 12 - The CMS HCAL scheme.

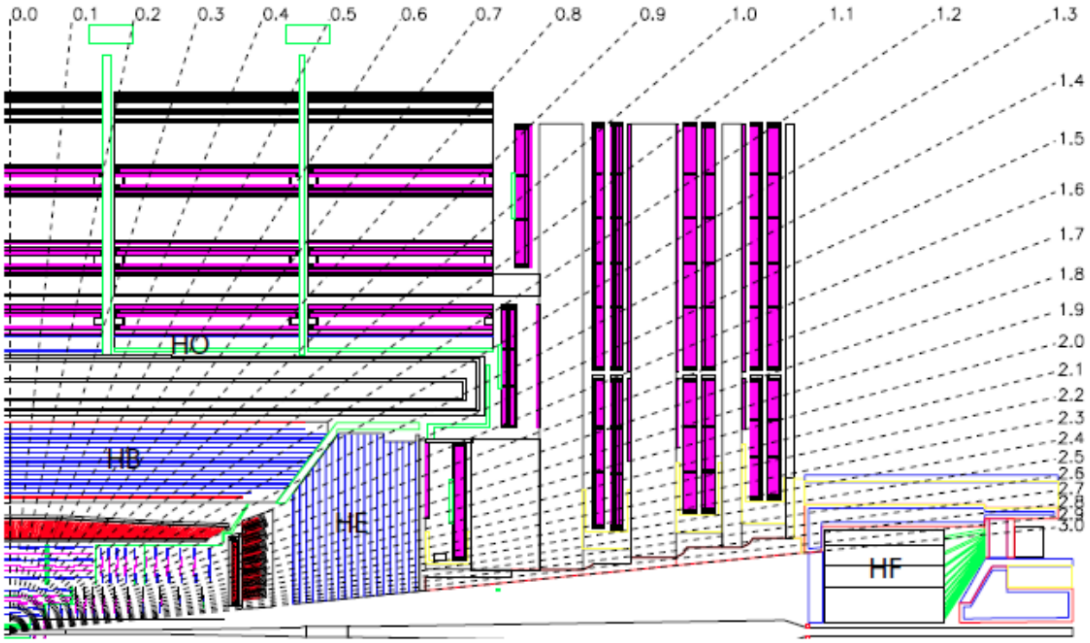

Subtitle: Diagram of the HCAL geometry.

Source: Figure extracted from CMS COLLABORATION, 2008, p. 123.

in the CMS Muon System, the drift tube chambers (DTs), the cathode strip chambers (CSCs) and the resistive plate chambers (RPCs).

- **DTs**: They are located in the barrel region covering a pseudorapidity region of $|\eta| < 1.2$. It is divided in 250 drift tube chambers into four stations with 12 wheel sectors. The DTs chambers are made of aluminum cells filled with a mixture of Ar and CO_2 gas, and in the center they have an anode wire to collect the electrons that are produced by the muon interaction with the gas mixture.

- **CSCs**: They are located in the endcap region covering a pseudorapidity region of $0.9 < |\eta| < 2.4$. It is composed of four disks in each side with three rings in the innermost disk and two rings in other 3. In the outer disk, each ring has 36 CSCs and in the other disks each ring has 18 CSCs. A CSC has 7 cathode strip planes intercalated with 6 gas (Ar, CO_2 and CF_4) gaps enveloped by a plane of anode wires. When a muon crosses the chamber it interacts with the gas causing an electron avalanche that creates a discharge in the wire.

- **RPCs**: They are located in the endcap (four disks each) and barrel regions (six wheels), in order to complement the measurement of the muon. It is composed of a gas mixture of $95.2\%C_2H_2F_4 - 4.5\%Iso - C_4H_{10} - 0.3\%SF_6$ placed in the gas gap.

Figure 13 - The CMS Muon Chamber System scheme.

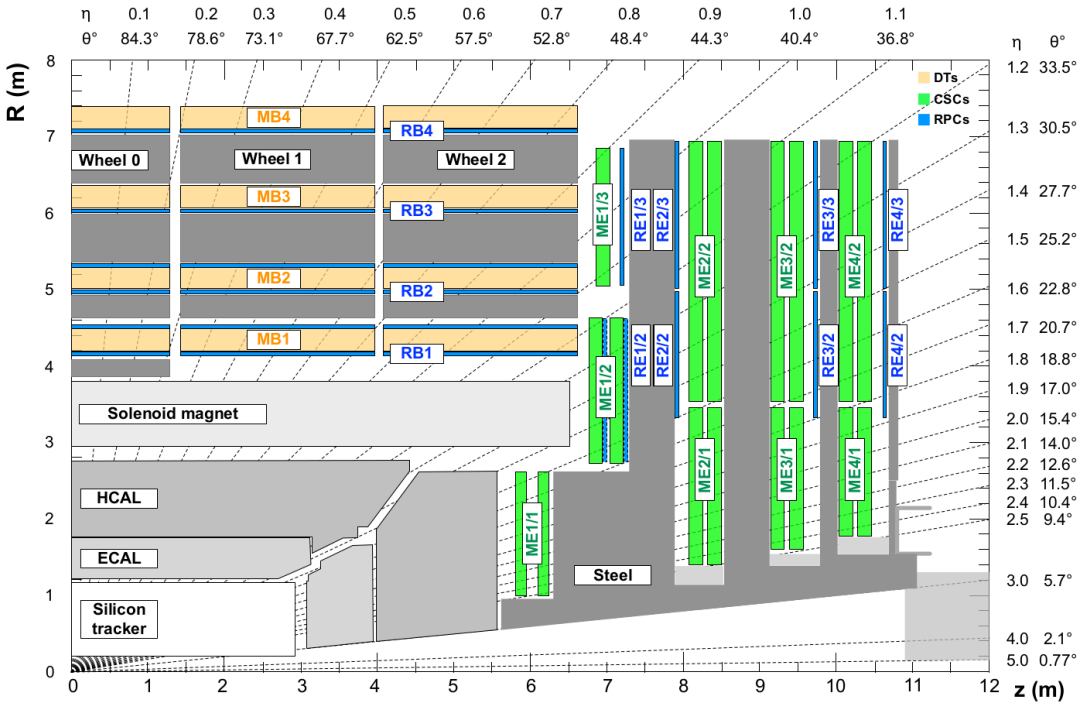

Subtitle: The Muon System design in a cross section of the CMS Experiment.
Source: Figure extracted from ABBIENDI, 2015, p. 2.

Each camera is composed of two gas gaps around a plane of copper strips.

In figure 13 there is a longitudinal view with the different parts of the Muon System.

2.2.2 Trigger System

The LHC delivers a high rate of collision to the experiments. The bunch crossings happen with a frequency of 40 MHz. As already mentioned, in each bunch crossing it can occur over 40 collisions (the pileup), therefore the collision rate can be over 1.6 GHz. This number makes it impossible to process and store all the events since a single raw event takes around 1—2 MB on disk, which means around 40 TB/s of data to be collected. If the full reconstruction is taken into account, this number could grow to several PB/s. Most of these events are not interesting for physics analyses, it includes basically low transverse momentum interactions so called minimum bias events.

To reduce this big amount of data without losing interesting events, CMS has a trigger mechanism. It consists of two levels: the L1 (Level-1 Trigger) and the HLT (High Level Trigger). The L1 is able to reduce the data taking rate from 40 MHz to 100 kHz,

then the HLT can reduce it further to 1 kHz.

2.2.2.1 Level-1 Trigger

The L1 is composed of a set of decisions based on the calorimeters and the muon system made by a hardware programmable system. The goal is to decide if an event should pass to the next processing step or it has to be rejected, it should happen in the maximum time of 4 μs.

Basically, the decision is taken by looking for a signal consistent with a muon in the DT, CSC, and RPC, or a signal consistent with taus, photons, electrons, jets or high missing transverse momentum by energy clusters in the HCAL and ECAL. The L1 system is composed of three subsystems: the L1 muon trigger, the L1 calorimeter trigger, and the L1 global trigger. The last one is responsible for the final decision.

2.2.2.2 High Level Trigger

The events accepted by the L1 are reconstructed by software in a more sophisticated process using all the detector subsystems. Many algorithms process the event in parallel looking for different kind of physic signatures. For each positive signature, the event receives an HLT tag that is used in the analysis level to identify the event.

For very common signatures the HLT tags are prescaled. For example, an HLT that tags events with at least one jet with transverse momentum of 400 GeV could have a prescale of 10, it means that in 10 events with this condition just one will receive the HLT tag. The prescale helps to reduce the data storage to a maximum rate of 100 Hz.

The organization of the HLT software consists of a layered structure. The first one is made using the calorimetry and muon information, called Level 2. The next layer uses the pixel information, called Level 2.5 and the last one uses all the tracking detectors, Level 3.

2.2.3 Physics event reconstruction

In order to build the physics objects (muon, electron, photon, tau, jet, missing transverse energy, etc) CMS uses several standard algorithms to perform its reconstruction and identification. They must be compact and carry all the information needed to do a physics analysis. A physics object is reconstructed using different subdetectors and to connect the information CMS uses a technique called Particle Flow.

The focus of this subsection will be the description of the Particle Flow technique and the reconstruction and identification of the useful physics objects for the analysis presented in this thesis: jets, muons and missing transverse energy.

2.2.3.1 Particle Flow

Particle Flow (PF) is the technique used in the CMS Collaboration for event reconstruction (SIRUNYAN et al., 2017). It makes possible the determination of the kinematical information, identification and reconstruction of the stable particles coming from the collision using all the CMS subdetectors. With the characterization of the individual particles, PF can build the jets and measure the missing transverse energy.

The idea of the PF algorithm consists on extrapolating the tracks (built in the Tracking System) through the calorimeters (electromagnetic and hadronic one) checking if they can be associated with boundaries of specific calorimeters clusters. A group of tracks associated with a cluster or clusters can be correlated with the presence of a charged hadron, for example after the identification of a charged hadron, the algorithm searches for other particles with the rest of the tracks and clusters information. The combination of all subdetectors is used to determine the four-momentum of the particles.

From a charged particle passing through the Tracking System layers, the track reconstruction is based on the Kalman Filter (FRüHWIRTH, 1987). The algorithm starts with a seed (initial tracks candidates in the first layer) that is used for the pattern recognition where the Kalman Filter helps to associate the seed with the hits in the next layers to reconstruct the particle trajectory. The next step is to estimate the track kinematic parameters from a fit of the track trajectory. In the final step, the tracks are selected using quality requirements. There are many refinements, for example, the resolution and efficiency of the detector, multiple scattering and limits in the number of layers.

The calorimeter clustering algorithm starts with a cluster seed (an activated calorimeter cell with energy over a specific threshold) then add the cells (also activated with energy over a specific threshold) with at least one side in common to build the topological clusters, which are used to build the particle flow clusters.

2.2.3.2 Muon reconstruction

The muons are reconstructed using the Muon System and the Tracking System. In the first one, a fit is used to build the muon trajectory from a seed (DT or CSC clusters). The trajectory is determined using all Muon System components (DT, CSC, and RPC). In the tracker, the muons are reconstructed if they have $p_t > 0.5$ GeV and $p > 2.5$ GeV

and if the track can be extrapolated to a cluster in the Muon System.

There are three types of reconstructed muons in the CMS. The *standalone muon* that is reconstructed only in the Muon System, the *tracker muon* that is reconstructed only in the Tracking System and the *global muon* that is built from a fit using both Muon and Tracking System.

CMS uses also a set of quality flags to characterize the reconstructed muons. The flag that will be used in this thesis is the *HighPtMuon*. It is defined as follows:

1. The candidate should be reconstructed as a global Muon.
2. The relative error of the muon best track p_T should be less than 30%.
3. At least one hit from the muon chamber must be included in the muon track fit.
4. The tracker track should be matched to a short sketch track made of DT or CSC hits in at least two muon stations.
5. The tracker track should have a transverse impact parameter smaller than 2 mm with respect to the primary vertex.
6. The longitudinal distance (along with the z-axis) of the tracker track to the primary vertex should be smaller than 5 mm.
7. Number of activated pixels greater than zero.
8. Number of tracker layers with hits greater than 5.

Another important quality selection for the muons produced in a W decay is the muon isolation. One way to require isolation is by using *Tracker-based Isolation* method. It is calculated with the sum of the p_T of the tracks from the primary vertex[1] of the event in a cone around the muon with a radius[2] of 0.3 divided by the p_T of the muon. If this value is smaller than 0.1 then the muon is said to be isolated with a *loose* flag; if it is smaller than 0.05 the flag is said *tight*.

2.2.3.3 Jet reconstruction

The LHC collisions give rise to a large number of particles. As it is known, quarks and gluons undergo a hadronization or fragmentation process producing many new particles in the event. Since a quark (or gluon) can be produced with a large momentum,

[1] The vertex that has the highest sum of the p_T of all tracks.

[2] $\Delta R = \sqrt{(\Delta\eta)^2 + (\Delta\phi)^2}$.

the particles produced from the hadronization (or fragmentation) process carry part of the initial particle momentum and they will be collimated around the initial particle direction. A jet can be defined as a narrow cone that includes all (or a big part) of these collimated particles.

The particles inside a jet are basically composed by charged and neutral hadrons. As it was discussed before, the charged ones are characterized in the Tracking and HCAL systems and the neutral ones only in the HCAL. There are several types of jet reconstruction algorithms. In the following analysis, the *particle-flow jet* (PF Jet) was used. The reconstruction quality of the PF Jet is better than the others because it uses all the information built from the Particle Flow algorithm, in other words, it uses all the subdetectors information.

There are many algorithms to cluster particles inside a jet, the PF Jet uses the anti-k_T algorithm (CACCIARI; SALAM; SOYEZ, 2008) which uses two main variables: the distance between the objects i and j (d_{ij}), and the distance between object i and the beam (d_{iB}). They are defined by:

$$d_{ij} = min(k_{ti}^{-2}, k_{tj}^{-2})\frac{\Delta_{ij}^2}{R^2} \tag{17}$$

and

$$d_{iB} = k_{ti}^{-2} \ , \tag{18}$$

where k_{ti} is the transverse momentum of the particle i, $\Delta_{ij}^2 = (y_i - y_j)^2 + (\phi_i - \phi_j)^2$, y_i and ϕ_i are respectively the rapidity and azimuthal angle of the particle i and R is the radial parameter. The algorithm starts calculating d_{ij} for all particles combinations and d_{iB} for all particles. If d_{ij} is the smallest distance, the particles i and j are combined into a new particle and the algorithm starts the calculation again. If d_{iB} is the smallest distance, the particle i is considered a jet, it is removed from the particle list and the algorithm starts again. The procedure is repeated until no more particles are left. For the 2016 data, the jet collections are built with a radius of 0.4 and 0.8.

In a high pile-up collision, there are many particles inside the jet that do not come from the jet vertex. To remove these particles from the jet clustering, the technique Charged Hadron Subtraction (CHS) is used. It removes the charged particles that do not come from the primary vertex before the jet clustering.

Also, as it was mentioned for muons, there are quality flags for jets. The interesting flag for the thesis is the *loose jet* one, in the region of $|\eta| \leq 2.7$ the requirement for this flag is:

1. Neutral hadron fraction < 0.99.

2. Photons and electrons fraction < 0.99.

3. Number of Constituents > 1.

4. If the jet is in the region of $|\eta| \leq 2.4$:

   - Charged hadron fraction > 0.
   - At least one charged constituent.

Even with these requirements, a single isolated muon can be reconstructed as a *loose jet*, then it is important to exclude these "muon jets".

For the process where a jet pair could come from high boosted particles (for example a W produced in the aQGCs process), a big fraction of the particles from both jets is overlapped in the same region which makes it impossible to reconstruct these two jets separately. To investigate these kinds of processes it is usual to use a bigger jet that clusters all the particles from the two original jets. Two variables can be used over these big jets to identify if it comes from highly boosted particles.

- **Pruned jet mass**: The idea of pruning is reclustering the constituents of the big jet applying additional veto conditions. The particle with the smaller transverse momentum of a pair of two particles to be merged is vetoed if:

$$\frac{min(k_{t_i}, k_{t_j})}{k_{t_{i+j}}} < z_{cut} \tag{19}$$

  and

$$\Delta R_{ij} > \alpha \times \frac{m_J}{k_{t_J}}, \tag{20}$$

  where $k_{t_{i+j}}$ is the transverse momentum of the two merged particles, m_J and k_{t_J} are the mass and transverse momentum of the big jet respectively. The parameters z_{cut} and α are chosen to be 0.1 and 0.5 respectively. The pruned jet mass is the invariant mass of the pruned jet.

- **Subjettiness ratio**: Given a subjet N (inside the big jet), the N-subjettiness is the sum of the angular distances of the jet constituents with respect to their subjet axis. The N-subjettiness is given by:

$$\tau_N = \frac{1}{d_0} \sum_k k_{t_k} min(\Delta R_{1,k}, \Delta R_{2,k}, ..., \Delta R_{N,k}), \tag{21}$$

  where k runs over the jet constituents, $d_0 = \sum_k k_{t_k} R_0$ and R_0 is the radius of the jet and $\Delta R_{i,k}$ is the angle between the jet constituent k and the subjet candidate i. The subjettiness ratio $(\frac{\tau_2}{\tau_1})$ is an important discriminator between boosted particles jets and QCD jets.

Figure 14 - The b-tagging CSV discriminator distribution.

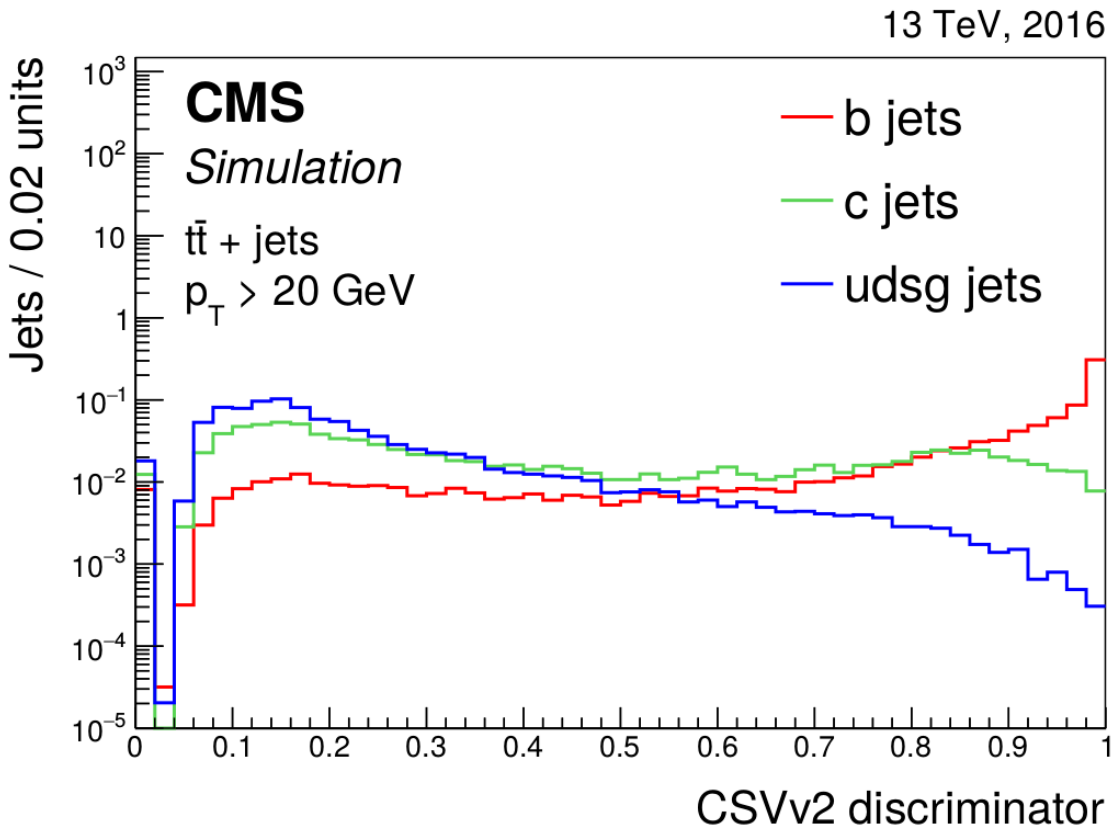

Subtitle: The CSVv2 discriminator for b, c, and uds flavors (plus gluons) in a sample of $t\bar{t}$ simulated events.

Source: Figure extracted from SIRUNYAN et al., 2018, p. 20.

Processes with the presence of bottom quark jets (b-jets), as for example top quark production, are very common in high energy collisions. The identification of these jets is very important to characterize the background since the W decay into quarks has a very low branching ratio to bottom and top quarks.

There are several algorithms to identify b-jets, the main idea is to explore the long lifetime of the b quark hadrons (originated from b-quark hadronization). Since it decays in a position displaced from the primary vertex, this position is called secondary vertex. The algorithm used in the analysis presented in this thesis is the Combined Secondary Vertex (CSV). It consists in combining the primary vertex, impact parameter and secondary vertex information using a neural network. The algorithm has a discriminator output that varies between 0 and 1. On figure 14 it is presented the distribution of the discriminator for a sample of $t\bar{t}+jets$ simulation with the 2016 CMS conditions. There is also a misidentification tag for the CSV algorithm, it can be loose, medium or tight that corresponds respectively to 10%, 1% and 0.1% of efficiency.

The object reconstruction is not perfect, several problems might happen due to the response of the subdetectors, electronic noises, pile-up, etc. A correction of the jet reconstruction is needed to have a better description of the physics process. CMS has the *Jet Energy Correction* (JEC) procedure to do that. It consists of a series of steps applied in sequence to compute the multiplicative factor $\mathcal{C}$. The correction of each component of the jet four-momentum is given by:

$$p_{\mu}^{cor} = \mathcal{C} \cdot p_{\mu}^{raw}. \tag{22}$$

The factor $\mathcal{C}$ is obtained from the sequential steps by the equation:

$$\mathcal{C} = \mathcal{C}_{offset}(p_T^{raw}) \cdot \mathcal{C}_{MC}(p_T^{'}, \eta) \cdot \mathcal{C}_{rel}(\eta) \cdot \mathcal{C}_{abs}(p_T^{''}), \tag{23}$$

where each factor represents a step:

- $\mathcal{C}_{offset}$ is the offset correction. It is obtained from the estimation of the energy contribution of the events that are not associated with the hard scattering in the event and electronic noise.
- $\mathcal{C}_{MC}$ is the Monte Carlo calibration correction. It is computed based on simulation and corrects the energy using the energy of the generated jets.
- $\mathcal{C}_{rel}$ is the relative jet energy scale. It is estimated using simulation and data to correct imperfections of the detector modeling as a function of η.
- $\mathcal{C}_{abs}$ is the absolute jet energy scale. It is calculated using simulation and data to correct imperfections of the detector modeling as a function of p_T.

2.2.3.4 Missing Transverse Energy

The design of CMS experiment and its subdetectors were done having in mind the ability to characterize a set of particles. But there are particles that do not interact with the detector, such as neutrinos and some potential Beyond Standard Model particles, because they do not interact with the material of the subdetectors. On the other hand, it is possible to estimate their transverse momentum by imposing the momentum conservation, since before the collision, it is practically zero. The transverse momentum of the invisible particles ($\vec{p}_T^{miss}$) can be written as the negative of the vectorial sum of the transverse momentum of all reconstructed particles:

$$\vec{p}_T^{miss} = -\sum_{PFobj} \vec{p}_T^{PFobj}. \tag{24}$$

The $\vec{p}_T^{miss}$ modulus is called missing transverse energy (E_T^{miss}).

Figure 15 - Interactions per crossing (pileup) for 2011-2012 and 2015-2018

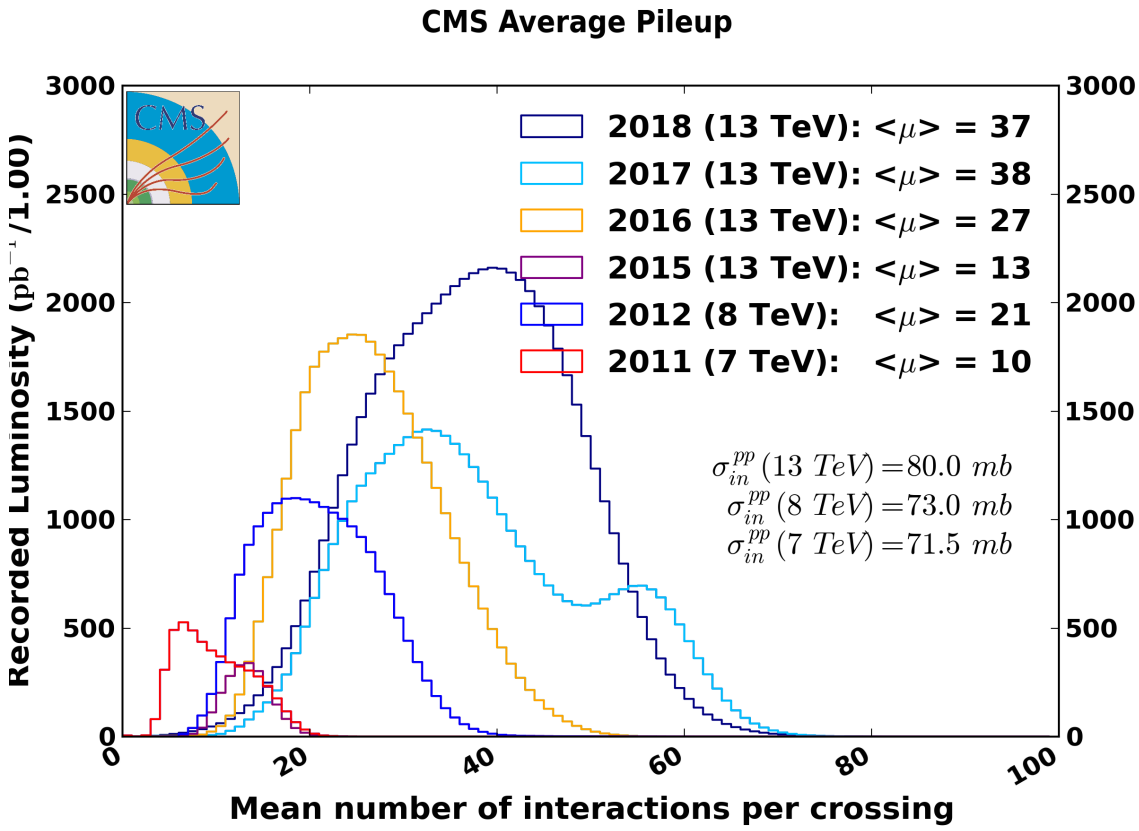

Subtitle: Distribution of the average number of interactions per bunch crossing for pp collisions in several data taking periods. The overall mean values and the inelastic cross sections are also shown.

Source: CMS COLLABORATION, 2018b.

2.3 Precision Proton Spectrometer

The high multiplicity of collisions in each bunch crossing during the Run II period of LHC, as can be seen in figure 15, makes it impossible to apply the usual strategy to study Central Exclusive Production and Diffractive Processes, where the rapidity gaps in the central detector are used. The solution implemented by the CMS Collaboration (in partnership with the TOTEM Collaboration) was to build a detector to measure the scattered protons that remain intact after the collision and correlate their kinematic information with the measurements in the other central CMS subdetectors.

The Precision Proton Spectrometer — initially named CMS-TOTEM Precision Proton Spectrometer (CT-PPS) — is a subdetector of the CMS experiment designed to measure protons scattered at the Interaction Point with small angles and the fractional momentum loss (ξ) between ~ 0.02 and ~ 0.15 and it started to collect data for analysis during the 2016 data taking. It has two arms, located in both sides of CMS at LHC sectors

Figure 16 - Layout of PPS in sector 56

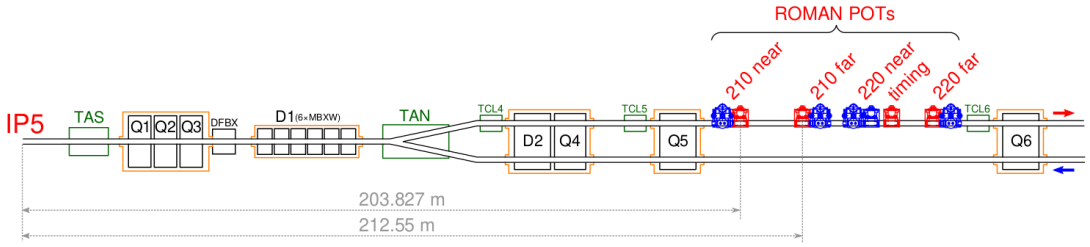

Subtitle: Layout of PPS detector in the LHC beam line at sector 56 as seen from above (not to scale) as the 2016 detector configuration. In the figure it is represented the magnets dipoles (D1, D2), the quadrupoles (Q1-Q6), the collimators (TCL4-TCL6), the absorbers (TAS, TAN), the quadrupole feedboxes (DFBX), the TOTEM RPs (in blue), the PPS RPs (in red), the incoming (in blue) and outgoing (in red) beam (the arrows on the right). The 2016 configuration.

Source: Figure extracted from CMS COLLABORATION et al., 2018, p. 3.

45 (positive z direction) and 56 (negative z direction), each sector can also be called arm left (sector 45) and arm right (sector 56). In 2016 data taking, each side of PPS was composed of two tracking stations, called “210 near” (210N) and “210 far” (210F), and a timing station used for preliminary studies. The tracking stations were placed at 203.8 m and 212.6 m away from the IP respectively.

The PPS detector sensors are located inside “Roman Pots” (RP), devices installed close to the beam that allow the insertion of the sensors to a distance of few millimeters from the beam. The main purpose of an RP is to insert the sensors without effect in the vacuum, in the stability of the beam and the accelerator operation. In the 2016 configuration, each tracking RP station was composed by 10 planes[3] of silicon strip sensors with each plane containing 512 individual strips. Each tracking RP has a resolution of about 12 μm.

The schematic representation of the PPS detector and the LHC beam line at sector 56 is presented in figure 16, sector 45 is symmetric with respect to the IP. The silicon strips in an RP are represented in figure 17.

[3] 5 planes oriented at $-45°$ angle with respect to the bottom of the RP and 5 planes oriented at $+45°$ angle.

Figure 17 - Layout of PPS silicon strip sensors in a RP.

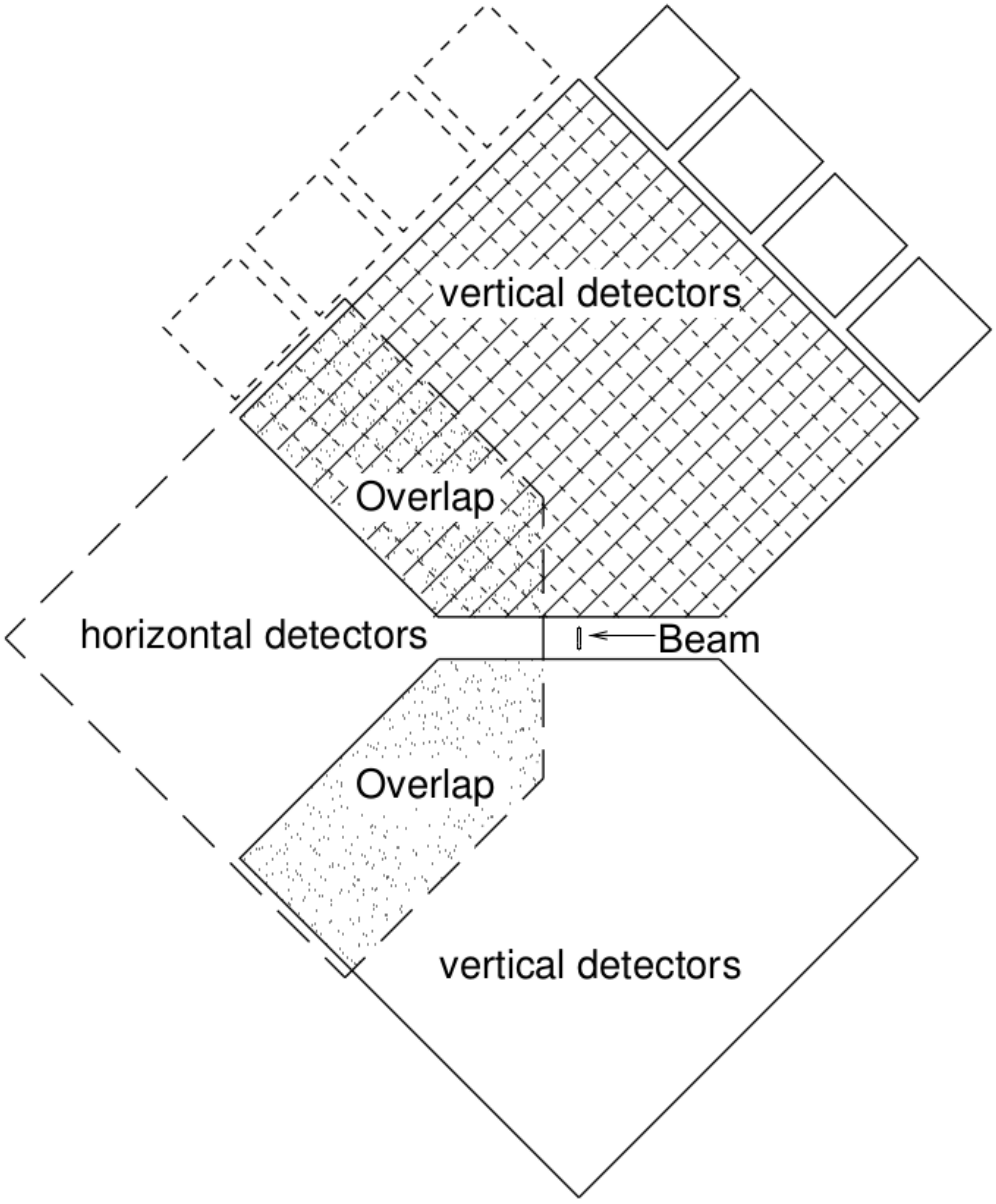

Subtitle: Schematic representation of PPS silicon strip sensors in different RPs. It is shown the horizontal and vertical RP, which are used for calibration; in the top RP the stripes oriented at $-45°$ and $+45°$ are shown.

Source: Figure extracted from CMS COLLABORATION et al., 2018, p. 4.

Figure 18 - Residual minimizing procedure of the RP relative alignment.

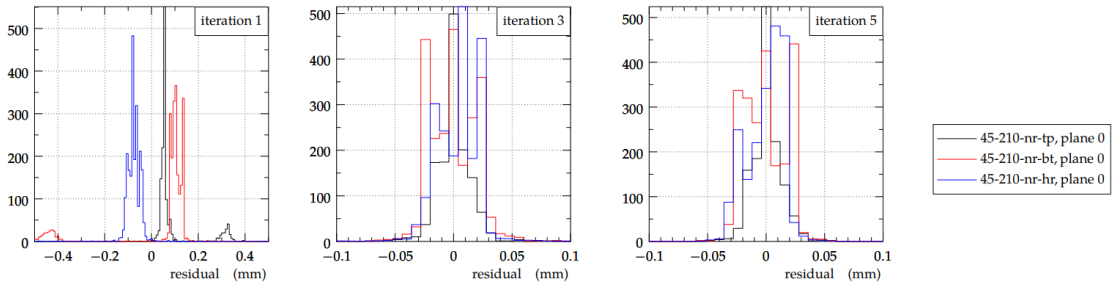

Subtitle: The residual distribution for the track-hit with different sensors. It is presented the distribution before optimization (left), after shift optimization (middle) and after shift and rotation optimization (right).

Source: Figure extracted from KASPAR, 2017, p. 3.

2.3.1 Alignment procedure

The fractional momentum loss of the proton is correlated with its hit position in the PPS sensors with respect to the beam center. To measure this position it is important to determine the location of the sensors relative to each other and also their positions with respect to the center of the beam. This is done by the alignment procedure.

The LHC provides a set of special runs with low-luminosity for calibration that are used by the PPS alignment procedure. During these runs, the sensors were inserted at about 5σ from the beam, where a σ is the standard deviation of the beam transverse dimension at the RP position. The alignment procedure uses the TOTEM RPs and PPS vertical RPs in the special runs. The resulting estimations of sensor positions are then used in the regular high-luminosity runs.

The collimators have a sharp edge facing the beam, then the RP are slowly approached to the beam (in steps of approximately 10 μm). When the rate in the beam-loss monitors has a rapid increase, it means that the RP had contact with the edge of the beam and it has the same position as the collimator. This position is used for the alignment.

The relative position of all the RPs in each side of CMS are determined by minimizing the residuals between hits and track fits in each RP, optimizing position and rotation. In figure 18 it is presented an example of the procedure.

The absolute alignment (RP position relative to the beam) is performed using elastic-scattering $pp \rightarrow pp$ events. The magnets in the beam line cause an elliptical shape of the hit distribution centered around the beam position. The absolute position of the RP is determined exploiting this symmetry. After the relative and absolute alignment procedure, the RP position is found with an uncertainty of 75 μm for vertical shifts, 50 μm for horizontal shifts and 5 $mrad$ for tilts on the x-y plane.

Figure 19 - Alignment procedure for physics fills.

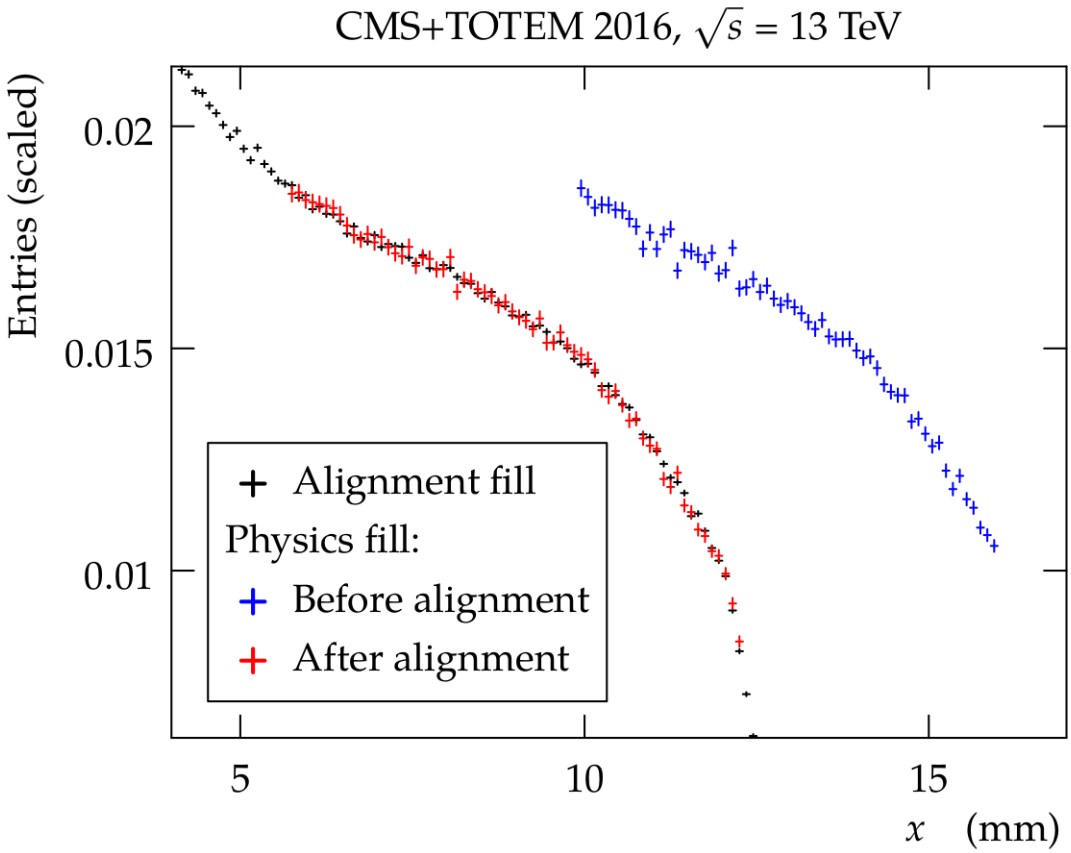

Subtitle: Distribution of the horizontal coordinate of the impact points of the tracks for the alignment and physics fills before and after the alignment.

Source: Figure extracted from CMS COLLABORATION et al., 2018, p. 5.

The RP and the beam positions can change for different fills, then for each physics fill the alignment has to be redetermined. The basic differences between physics and alignment fills are the high luminosity and the RP insertion, that is around 15σ for the physics runs. The kinematics of the scattered protons have a similar distribution in the two types of fills, then the alignment is done matching these distributions with the same in the alignment fill. In figure 19 there is an example of this procedure. The uncertainty for the horizontal alignment in the physics runs is about 150 μm.

2.3.2 Proton reconstruction

Reconstruction of the scattered protons depends on the track reconstruction in the RP and on the LHC beam optics. The latter is necessary, since it is needed to know the magnetic field description between the IP and the RP in order to describe the proton

Figure 20 - Track impact point distribution.

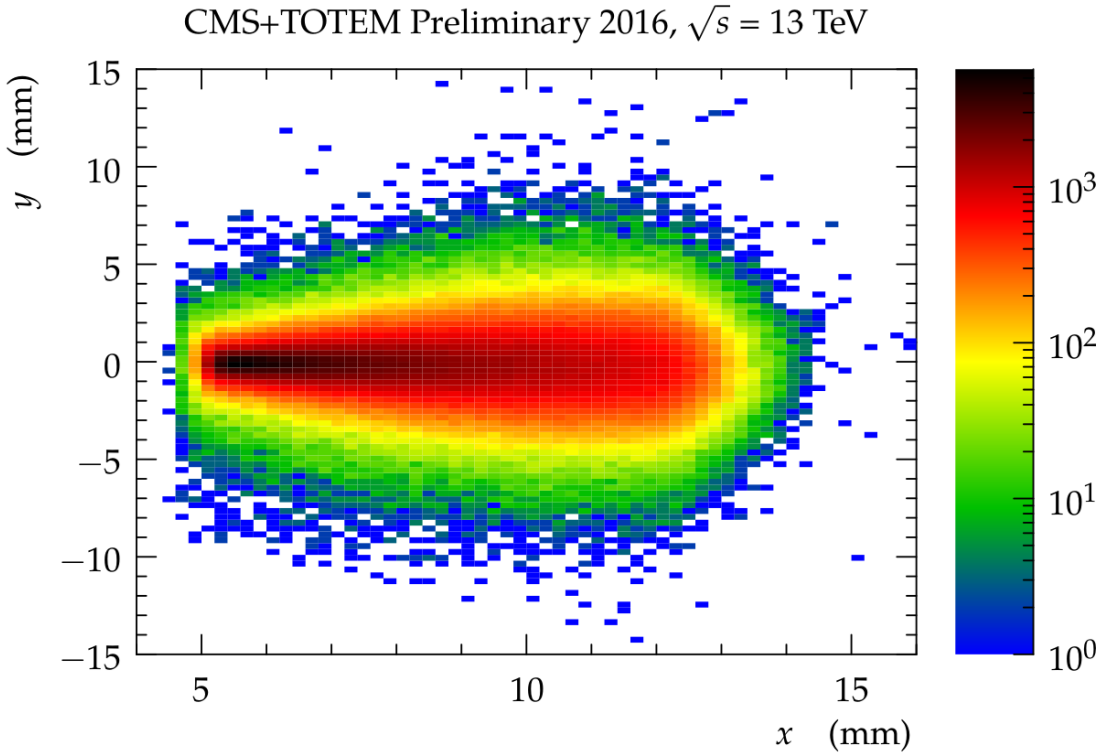

Subtitle: The track impact point distribution in RP 210F at sector 45, 2016 data.
Source: Figure extracted from CMS COLLABORATION et al., 2018, p. 8.

trajectory. Once determined the beam optics and the track reconstruction made, the proton ξ can be associated with the hit position in the RP.

2.3.2.1 Track reconstruction in the Roman Pots

The trajectory of the protons in the RP can be considered as a straight line since there is no significant magnetic field there. The tracking reconstruction requires hits in at least 3 planes in each of the two strip orientations. The reconstruction starts looking for linear patterns along z among the detected hits. The patterns in both strip orientations are associated and a fitted track produces a "track impact point", with x and y coordinates, at the center of the RP (z direction). In figure 20 there is an example of the track impact point distribution in RP 210F at sector 45.

A detector made of strips can only reconstruct the protons in events where only one proton hit the detector, otherwise ambiguities appear which turns impossible to associate the hits to the corresponding track. In events with high pileup many scattered protons

can arrive in the RP, therefore there is an inefficiency in the track reconstruction related to the multi-tracking in the RP. This inefficiency goes from 15 to 40% in the 2016 data.

Another inefficiency in the tracking reconstruction is given by the radiation damage effect. The RPs are not designed to be exposed to high radiation doses and, as expected, the sensor planes suffer large radiation damage after collecting about 10 fb^{-1}. Before the radiation damage, the efficiency per plane was estimated to be higher than 97% and after, this effect has to be reevaluated. As it is shown in the figure 20, it is possible to see that the hit distribution decreases with x, e.g. the hits are concentrated closer to the beam, which explains why the radiation damage has a dependence with x. In the analysis chapter, the strategy to avoid the radiation damage impact will be described.

There is also, with smaller impact, reconstruction inefficiency due to the production of showers in the interaction between the protons and the detector material. It is estimated to be around 3%.

2.3.2.2 LHC beam optics

The track impact point has a strong dependence on the magnetic set between the IP and the RPs. The description of this dependence can be parameterized by the beam optics using the optical functions to determine the proton path. In this parameterization, the elements in the beam line are treated as optical lenses. The proton trajectory (consequently its kinematics) can be described by:

$$\mathbf{d}(s) = T(s,\xi)\cdot\mathbf{d}^* \ , \tag{25}$$

where $\mathbf{d} = (x, \theta_x, y, \theta_y, \xi)$, s is distance from the IP, '*' denotes the proton variables in the IP and T is the single-pass transport matrix given by:

$$T = \begin{pmatrix} v_x & L_x & m_{13} & m_{14} & D_x \\ \frac{dv_x}{ds} & \frac{dL_x}{ds} & m_{23} & m_{24} & \frac{dD_x}{ds} \\ m_{31} & m_{32} & v_y & L_y & D_y \\ m_{41} & m_{42} & \frac{dv_y}{ds} & \frac{dL_y}{ds} & \frac{dD_y}{ds} \\ 0 & 0 & 0 & 0 & 1 \end{pmatrix} \tag{26}$$

where $L_{x,y}$ is the effective length, $v_{x,y}$ is the magnification, $D_{x,y}$ is the dispersion and m_{ij} are the coupling coefficients that are 0 for the LHC nominal optics by design. The horizontal dispersion can be written by:

$$D_x = \frac{\partial x}{\partial \xi} \ . \tag{27}$$

Figure 21 - Correlation between x coordinate of the track impact point and ξ

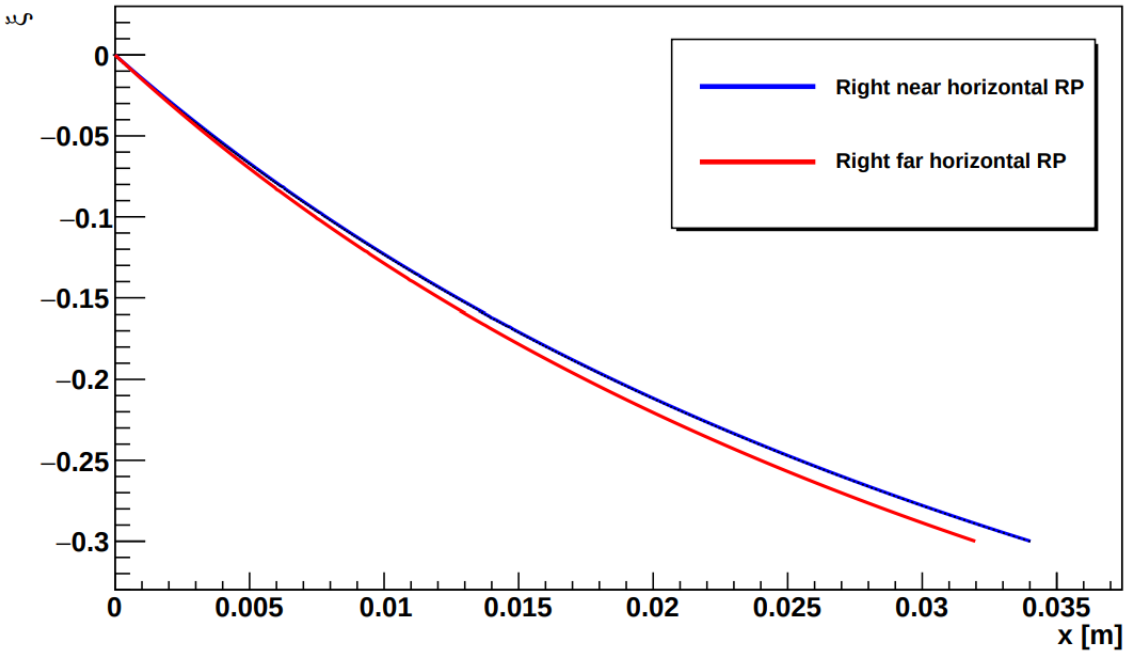

Subtitle: Derived correlation between x and ξ for one of the LHC beams for the 2016 configuration.

Source: Figure extracted from NEMES, 2017, p. 10.

From equations 25 and 27 and for low-ξ, it is possible to write:

$$x \approx D_x \cdot \xi \ . \tag{28}$$

From the full simulation of the LHC beam between IP and the RPs, Nemes (NEMES, 2017) has derived a correlation between x and ξ, which is shown in figure 21.

2.3.2.3 ξ determination

ξ, the fractional momentum loss, is the main proton variable for CEP and diffractive processes. With PPS, its reconstruction can be done (see figure 21) by measuring x and corralating it to the value of ξ. The main uncertainty in this procedure is related with the dispersion (D_x) calibration (that is around 5.5%) and the neglected terms in equation 27. There is also an uncertainty related to the horizontal alignment of about 150 μm, as already mentioned.

2.4 **Work for the CMS Collaboration**

During the stay at CERN, some activities were performed by the author together with the CMS and TOTEM collaborations for the PPS commissioning and shifts in the operation of the CMS experiment. A brief description of these activities will be given bellow.

The activities were performed in the year of 2017 using the PPS configuration of that year. The configuration of the detector is described on appendix A.

2.4.1 Alignment studies

An alternative method for the RPs alignment procedure was investigated. The method, called "dynamic alignment" is based on (AALTONEN et al., 2012). It consists of applying several shifts in the RP position and calculating the four-momentum transfer squared of the proton, t. The t distribution has an exponential shape, and the slope of the distribution has its minimum when the shift is closer to the negative misaligned position.

This study was performed on simulated samples and the idea was tested by putting the RP in a misaligned position and try to find the correct relative and absolute position using the method. In figure 22 it is presented the case where a misalignment was introduced only on RP 210N in the horizontal direction with a value of +0.5 mm. Using the new method a relative misaligned position of +0.499 mm with 0.136 mm of standard deviation was found. On the other hand, this method was not able to find the absolute alignment, since there is not enough sensitivity on t when the new method is used applying shifts on the RPs together (considering the relative alignment done).

2.4.2 Radiation damage effect

During 2017 the impact of the radiation damage on the strip sensors in the PPS RPs was monitored by comparing the track impact point distribution of the CMS runs with a reference run. The reference run was chosen as a run at the beginning of the data taking when the sensors were not affected by the radiation damage. When the damage reached a level considered relevant, the high voltage on the sensors was increased to recover its performance.

In figure 23 there is an example of the sensor performance recovery. In Run 299593, it is possible to see a high impact of the radiation damage after 5 fb^{-1} of collected data. The impact in the sensor is concentrated in the region close to the beam. After this run, the high voltage was increased from 150 V to 200 V and it is possible to see a recovery of

Figure 22 - Dynamic alignment applied on the PPS simulation.

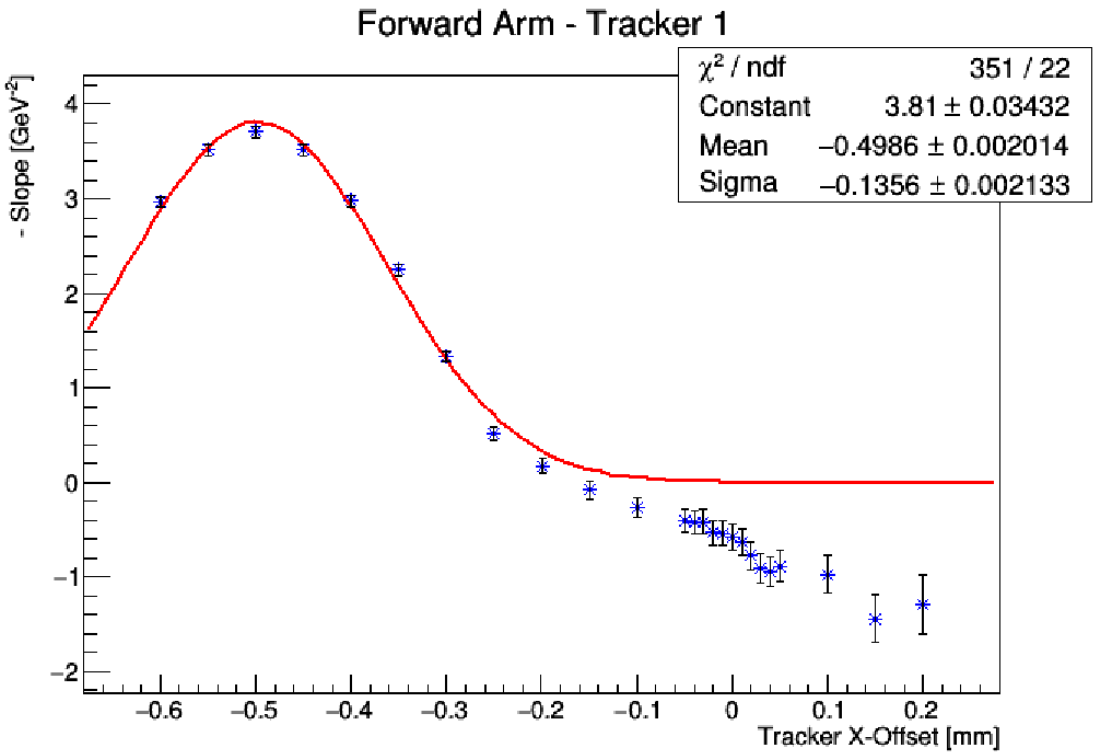

Subtitle: It is presented the slopes of the t distributions for several displacements applied on the x position of the RP.

Source: The author, 2019.

Figure 23 - The radiation damage impact in the PPS strip sensors.

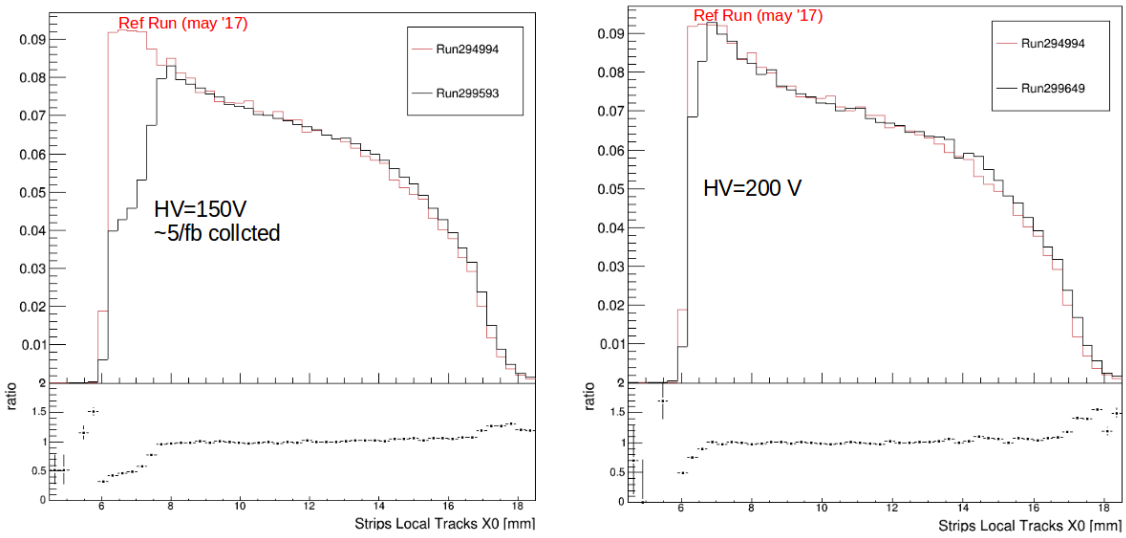

Subtitle: The x coordinate distribution of the track impact point in the runs 299593 (left) and 299649 (right) compared with the reference run. The distribution was normalized to one in the range $10mm$ to $16mm$.

Source: The author, 2019.

the sensor efficiency.

2.4.3 Multi-tracking inefficiency

The correlation between the average number of pileup and the inefficiency of the proton track reconstruction in the strip sensors was investigated. As mentioned before, the strip sensors are not able to reconstruct more than one proton per event.

In figure 24 there is the relation between the average number of pileup and the multi-tracking inefficiency for different beam conditions. Each point represents data collected in one lumisection[4] and different beam conditions were considered. As expected, it is possible to see a linear correlation between the average number of pileup and the multi-tracking inefficiency.

[4] A lumisection is the data taking period of 23 seconds.

Figure 24 - Multiple track inefficiency in the proton reconstruction.

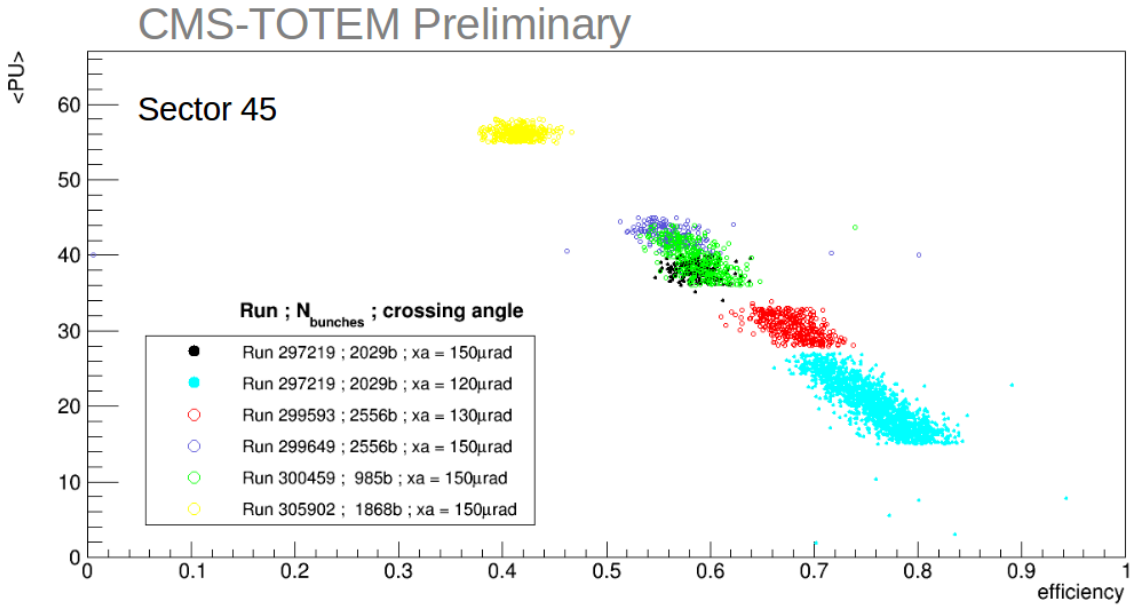

Subtitle: Relation between the pileup average number and the multi-tracking efficiency for different beam conditions. Each point represents a lumisection data taking.

Source: The author, 2019.

2.4.4 Timing detector stability

The PPS timing detector was commissioned to collect data for the first time in 2017. Commissioning is very important to understand its operation. In the 2017 configuration, the timing detector consisted of three scCVD[5] diamond planes and one Ultra Fast Silicon Detector (SADROZINSKI et al., 2016) plane in RP at 216m away from the IP. Each plane is divided into 12 segments for proton tagging, each segment is connected to an HPTDC[6] electronic module channel to measure the absolute Time Of Arrival (ToA) with respect to a trigger giving by CMS L1 and the hit in the sensor.

The stability of the ToA measurement was obtained comparing the average ToA in both sides of the detector with the vertex z-position per lumisection. In figure 25 an example of this study for plane 2, channel 1 is presented. This study has been done for all planes and all channels and it has been found a correspondence between the leading edge and the vertices movements.

The ToA has a fluctuation correlated with the z-position and the fluctuations are often just on Beam 2, which means that the LHC clock is synchronized with Beam 1.

[5] single-crystal Chemical Vapor Deposition.

[6] High Performance Time-to-Digital Converter

Figure 25 - ToA measurement stability for plane 2 channel 1.

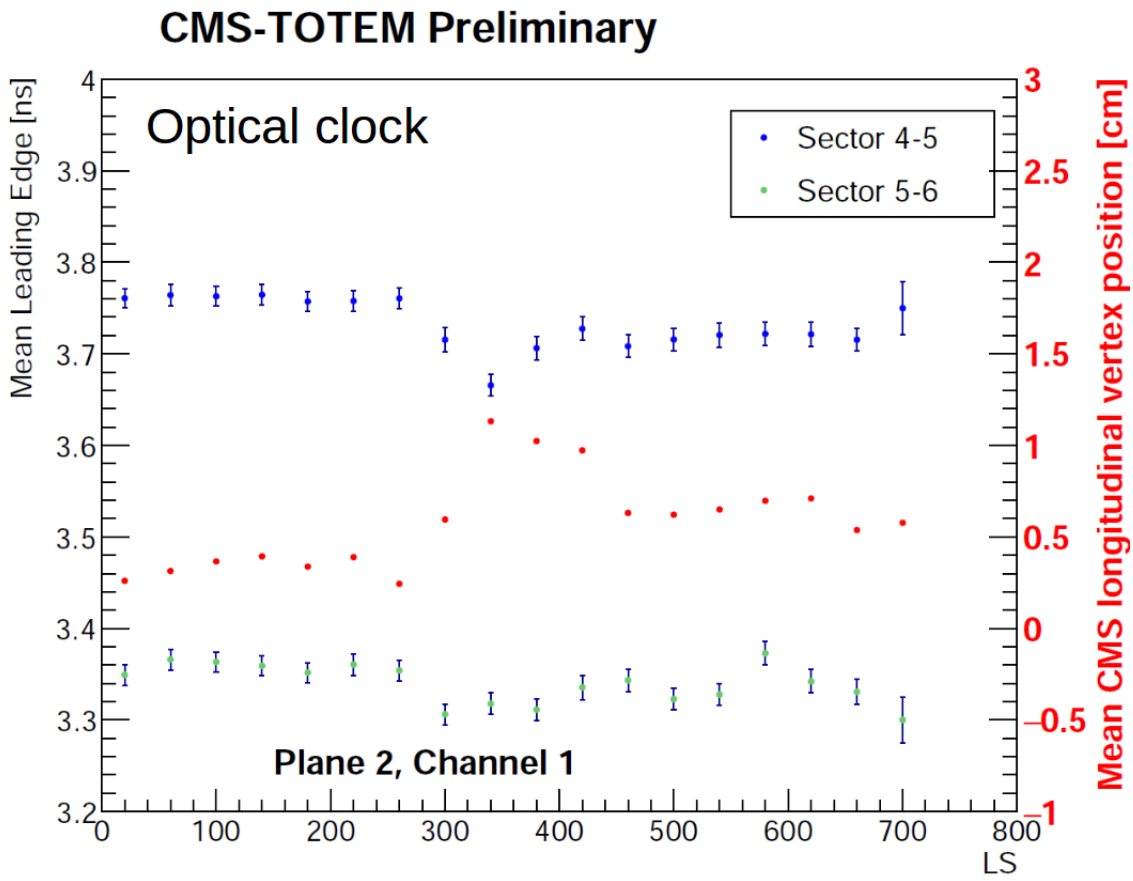

Subtitle: Mean ToA measured for sector 45 (blue) and sector 56 (green) and the mean z-position (red) evaluated per lumisection.

Source: Extracted from internal communication CMS COLLABORATION, 2017.

Large non-linearities were not found.

2.4.5 Shifts on detector operation

As part of the service for the CMS Collaboration, in the 2017 data taking, shifts for the CMS operation were also done, including many online Data Quality Monitoring (DQM) shifts and a few weeks of PPS Detector expert On-Call (DOC) shifts. In the following, a brief description of the idea of these shifts is presented.

- **DQM:** To be certain that the CMS subdetectors are taking data efficiently, the shifter monitors, at P5, their operation. The goal is to identify possible problems in the detector performance or integrity and notify the experts. The shifter also has to write a summary of all CMS Runs reporting any issues.

- **PPS DOC:** The on-call expert is the first contact in case of any problems and questions related to the PPS. The shifter is also the representative person for the subdetector in the run coordination to summarize the subdetectors operation and make any requests.

3 SIGNAL AND BACKGROUND SIMULATION

The data analysis requires a good understanding of the signal and background processes. To perform it, a set of simulated events was used, which should be able to reproduce the data as realistic as possible.

The event simulation can be basically divided into three steps: generation, simulation and reconstruction. The event generator has to be able to produce high energy collision processes with a set of parameters called *tunes* and conditions. An event can be generated using different Monte Carlo (MC) techniques. In the next subsection, the MC generators used for the background processes of the analysis presented in this thesis will be discussed briefly.

Once the events are generated, the next step is to simulate the interaction of the particles passing through matter and electronic response of the detector. After the simulation, the MC events have the same structure as when the data are collected, then the reconstruction step is the same for both, where the building of the physical objects is performed as discussed in the previous chapter. In figure 26, a diagram of the steps in the procedure to generate MC events and to process data for analysis is shown.

3.1 **Event generators**

As can be seen in figure 27, the event generation can be separated in subprocesses: the parton distribution functions (PDFs) that describe the proton structure in the interactions which are used as an input in the generators; the hard interaction between two partons inside the protons; the parton showers that describe how the partons produced in the previous step ramify in other partons; the hadronization that creates the hadrons taking into account the color confinement. Different Monte Carlo generators were used to perform these steps.

Pythia 8 (SJOSTRAND; MRENNA; SKANDS, 2008) is used to generate many different kinds of processes. It can be used either as a matrix element generator or to produce parton showers and hadronization when interfaced with other matrix element generators. It can generate Standard Model and Beyond Standard Model processes. Pythia is also able to produce events at leading order QCD which are used in the minimum bias event generation, this is important for the pileup description.

A combination of the MadGraph5 (ALWALL et al., 2011) and MC@NLO (ALWALL et al., 2014) event generators, referred to as MadGraph5_MC@NLO, is also used in the analysis. The first one is a matrix element generator used to generate several different processes, but it does not provide the parton shower that is computed by the second one.

Figure 26 - Diagram of the steps to have MC events and data ready for analysis.

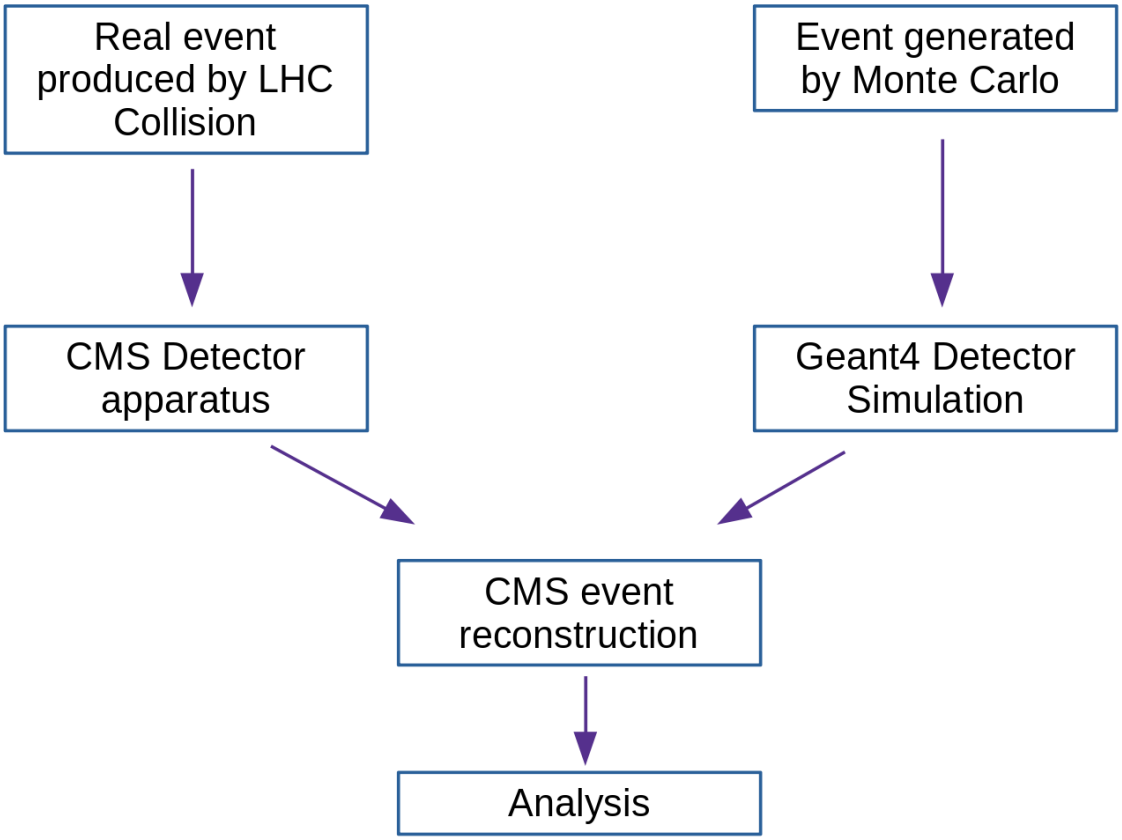

Subtitle: Description to have MC events and data from the generation (for MC events) or collision (for data) to the reconstruction structure.

Source: The author, 2019.

Figure 27 - Diagram of the generation steps.

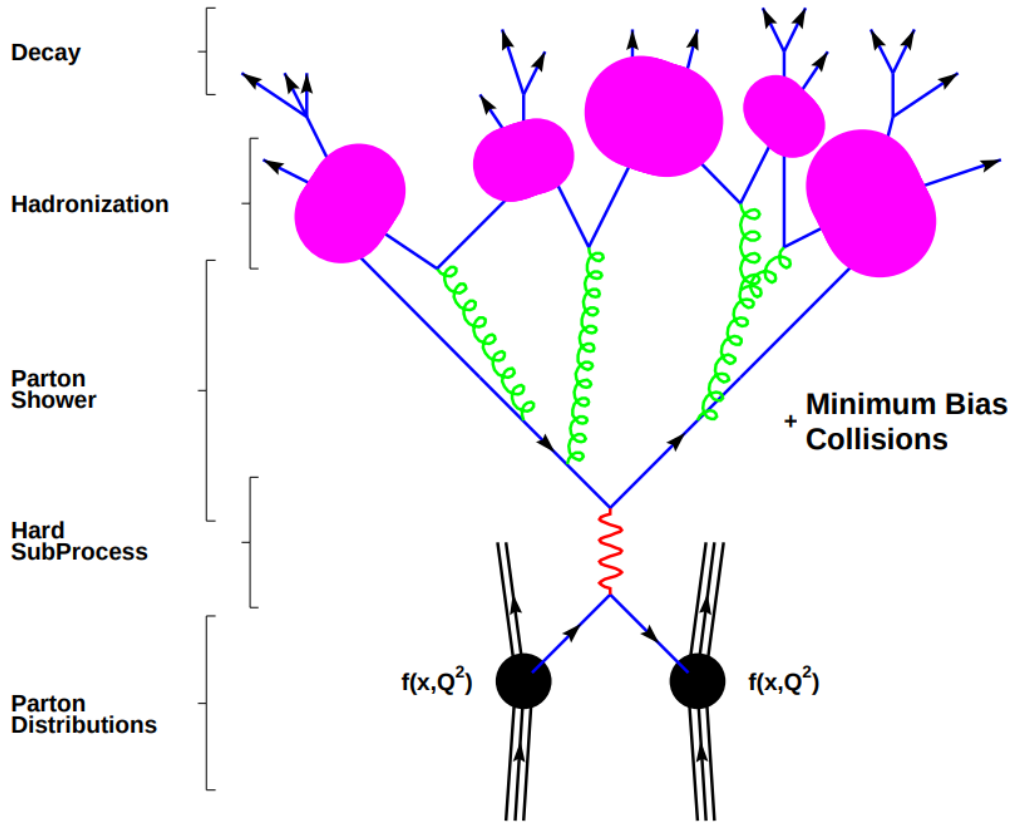

Subtitle: It is shown the different steps of the generation. The parton distribution in the *pp* interaction, the hard subprocess, the parton shower, the hadronization and finally the decay.

Source: Figure extracted from DOBBS et al., 2004, p. 26.

This combined generator can produce events in next-to-leading order approximation with the parton shower.

Another generator used is the Powheg (RE, 2011), that is a next-to-leading order QCD event generator that provides an easy interface with parton showers generators. It is important in order to produce vector boson fusion processes.

Finally, to generate the signal events the Forward Physics Monte Carlo generator (FPMC) (BOONEKAMP et al., 2011) was used. It is an extension of the DPEMC generator (BOONEKAMP; KúCS, 2005) and it is built inside the Herwig generator framework (CORCELLA et al., 2001). FPMC is devoted to generating the so called forward processes such as Central Exclusive Production, single diffraction, double pomeron exchange, and two-photon exchange processes with an easy interface to select the scattered protons kinematic parameters.

3.2 The Detector simulation

Once the generation step is done, the final state particles have to pass through the simulation of their interaction with the detector material, where the components of each subdetector have to be simulated. The GEANT4 package (AGOSTINELLI et al., 2003) is used to perform this step. To simulate the pileup effect on the events, minimum bias simulated events are superimposed on the main event.

The simulation should be able to describe the interaction of the particles with the different detector materials and their response as well as the active and dead material regions, the geometry, the magnet field, and finally the electronic signal.

The CMS simulation software for the central detector has been developed in the past decades (BANERJEE, 2012). The PPS simulation has been developed separately in more recent years as detailed in (SOUZA, 2017) and will be briefly described in the next subsection.

3.2.1 The PPS simulation

The goal of the PPS simulation is to calculate the position of the proton detection signals in the PPS RPs by estimating the transport of them from the IP — taking in account the dipole and quadrupole magnets, collimators and aperture devices — and simulate the hits in the detector sensors. The PPS simulation was developed initially for the PPS Technical Design Report studies, therefore it has the possibility to implement different customizations such as the z position of the RPs, the width and height of the sensors, their insertion distance with respect to the beam center and the angular and energy smearing of the protons. To produce the signal samples, the values that describe the 2016 configuration were used.

The transport of the protons from the IP to the RPs is computed by the Hector[7] code (FAVEREAU; ROUBY; PIOTRZKOWSKI, 2007) using the LHC beamline files that contain the description of the accelerator optics. To produce the signal simulation, the realistic optics parameters for 2016 were used.

The simulation of the hits in the sensors is performed when the propagated protons pass at the z coordinate position of the RPs. The RPs are simulated as a single plane and the hit is smeared to mimic the detector resolution effects. The simulation of the hit is done by applying a Gaussian smearing to the simulated hit position and limited according to the dimension of the sensor.

[7] Hector is a simulator to propagate particles in the beam line.

3.3 The signal and background processes

3.3.1 The Signal

The signal is composed of the W pair production by photon exchange in the CEP topology. In the final state, there is one W decaying into a muon and neutrino, while the other W decays into a quark pair that gives origin to a single high p_T jet. Several signal samples using different sets of anomalous couplings parameters as well as a Standard Model WW CEP sample were generated. The SM one is used to investigate if it could interfere in the aQGCs analysis.

The events were generated with the range of ξ between 0.022 and 0.15 because of the PPS acceptance and the proton transferred momentum squared t in the range between 0 and 4 GeV^2. For the aQGC signal samples, different parameter values were used, which are listed in table 5, as well as their cross sections and the number of generated events.

3.3.2 The Background

The signal final state can be imitated by many Standard Model processes. The background processes that are considered in the analysis are listed here.

- **W+Jets** is the main background. It is produced by parton-parton fusion with a W production ($qg \rightarrow Wq'$ or $qq' \rightarrow Wg$) where the W decays into a lepton-neutrino pair and the parton (quark or gluon) gives origin to a jet. It is generated by MadGraph5_aMC@NLO in next-to-leading order approximation with different ranges of the W p_T. A control region to verify the compatibility between data and the simulated events for this background will be defined.

- $t\bar{t}$ is the second main background since the top quark always decays into a W plus an additional quark (>99% being bottom quark), the $t\bar{t}$ production gives origin to a process with two W's. The inclusive generation was made by Powheg. A control region for this process will be also defined. It is also produced by parton-parton fusion ($q\bar{q} \rightarrow t\bar{t}$ or $gg \rightarrow t\bar{t}$).

- **QCD** is a multijet process produced by parton-parton fusion. The QCD samples are generated with a filter to accept events with at least one muon with $p_T > 5$ GeV. The events are generated by Pythia 8 with different ranges of the outgoing parton p_T.

- **Drell-Yan** is a lepton pair final state produced in a $q\bar{q}$ fusion. The process has additional jets from the proton fragmentation that can mimic the signal. It is

Table 5 - List of signal samples.

Sample	α_0/Λ^2 (GeV^{-2})	α_C/Λ^2 (GeV^{-2})	Λ_{cutoof} (GeV)	$\sigma \times BR$(fb)	number of events
WW_exc_SM	0	0	—	1.78	45000
WW_exc_AC_A0W1.1e-6_ACW0.0	1.1×10^{-6}	0.0	∞	2.01	45000
WW_exc_AC_A0W2.5e-6_ACW0.0	2.5×10^{-6}	0.0	∞	2.95	45000
WW_exc_AC_A0W5.0e-6_ACW0.0	5.0×10^{-6}	0.0	∞	6.42	45000
WW_exc_AC_A0W0.0_ACW4.1e-6	0.0	4.1×10^{-6}	∞	2.03	45000
WW_exc_AC_A0W0.0_ACW10.0e-6	0.0	10.0×10^{-6}	∞	3.17	45000
WW_exc_AC_A0W0.0_ACW15.0e-6	0.0	15.0×10^{-6}	∞	4.84	45000
WW_exc_AC_CUTOFF500_A0W0.9e-4_ACW0.0	0.9×10^{-4}	0.0	500	4.38	45000
WW_exc_AC_CUTOFF500_A0W5.0e-4_ACW0.0	5.0×10^{-4}	0.0	500	78.89	45000
WW_exc_AC_CUTOFF500_A0W10.0e-4_ACW0.0	10.0×10^{-4}	0.0	500	308.67	45000
WW_exc_AC_CUTOFF500_A0W0.0_ACW3.6e-4	0.0	3.6×10^{-4}	500	5.09	45000
WW_exc_AC_CUTOFF500_A0W0.0_ACW10.0e-4	0.0	10.0×10^{-4}	500	25.31	45000
WW_exc_AC_CUTOFF500_A0W0.0_ACW15.0e-4	0.0	15.0×10^{-4}	500	53.90	45000

Subtitle: Summary of the signal samples used for the analysis as well as its aQGC parameters, cross section and number of events.

Source: The author, 2019.

generated by MadGraph5_aMC@NLO in next-to-leading order approximation for different ranges of p_T.

- **Single top** can be produced in 3 different ways: in the t-channel in the $qb \to qt$ scattering mediated by a virtual W, it is generated by Powheg; in the tW-channel by a gluon-bottom quark scattering ($bg \to Wt$) which is also generated using Powheg; and in the s-channel when a quark-antiquark scattering gives origin to a top-anti-bottom final state ($q\bar{q} \to \bar{b}t$), it is generated by MadGraph5_aMC@NLO using a next-to-leading order approximation. In the following, the contribution of all these processes is considered just as a single top process.

- **Inclusive WW and WZ** processes are considered as background even with their small cross sections because they are the Standard Model processes closer to the signal topology. They are also produced by parton-parton fusion ($q\bar{q} \to WW(Z)$ or $gg \to WW(Z)$). For WZ, the MadGraph5_aMC@NLO generator was used and for WW, the Powheg generator.

The background simulated samples are listed in table 6 with their respective cross sections and the number of generated events. Official samples produced by CMS Collaboration for the 2016 analysis were used. When these samples were produced, the PPS simulation was not integrated with the standard CMS simulation procedure. Since the correlation between the central system and the proton information from PPS is important for the analysis and it is not available for the official background samples, the *ZeroBias* method was used. The method consists of mixing simulated events information with data information for scattered protons. For the analysis in this thesis, the simulated central system was mixed with PPS information from the 2016 dataset (same one used to perform the analysis) with no selection and no bias, therefore called "Zero Bias".

Table 6 - List of background samples.

MC Sample	σ(pb)	number of events
WjetsToLNu_Wpt-50To100_TuneCUETP8M1_13TeV-amcatnloFXFX-pythia8	3241.33	67082709
WJetsToLNu_Pt-100To250_TuneCUETP8M1_13TeV-amcatnloFXFX-pythia8	677.82	120124110
WJetsToLNu_Pt-250To400_TuneCUETP8M1_13TeV-amcatnloFXFX-pythia8	24.083	12022587
WJetsToLNu_Pt-400To600_TuneCUETP8M1_13TeV-amcatnloFXFX-pythia8	3.056	1939947
WJetsToLNu_Pt-600ToInf_TuneCUETP8M1_13TeV-amcatnloFXFX-pythia8	0.46	1974609
TT_TuneCUETP8M2T4_13TeV-powheg-pythia8	831.700	77081156
QCD_Pt-170to300_MuEnrichedPt5_TuneCUETP8M1_13TeV_pythia8	8654.493	17350231
QCD_Pt-300to470_MuEnrichedPt5_TuneCUETP8M1_13TeV_pythia8	797.3	48995686
QCD_Pt-470to600_MuEnrichedPt5_TuneCUETP8M1_13TeV_pythia8	79.025	19362943
QCD_Pt-600to800_MuEnrichedPt5_TuneCUETP8M1_13TeV_pythia8	25.09	9981311
QCD_Pt-800to1000_MuEnrichedPt5_TuneCUETP8M1_13TeV_pythia8	4.723	19767439
QCD_Pt-1000toInf_MuEnrichedPt5_TuneCUETP8M1_13TeV_pythia8	1.613	13599938
ST_t-channel_antitop_4f_inclusiveDecays_13TeV-powhegV2-madspin-pythia8_TuneCUETP8M1	80.95	38811017
ST_t-channel_top_4f_inclusiveDecays_13TeV-powhegV2-madspin-pythia8_TuneCUETP8M1	136.02	67240808
ST_s-channel_4f_leptonDecays_13TeV-amcatnlo-pythia8_TuneCUETP8M1	3.365	1000000
ST_tW_antitop_5f_inclusiveDecays_13TeV-powheg-pythia8_TuneCUETP8M1	35.85	6933094
ST_tW_top_5f_inclusiveDecays_13TeV-powheg-pythia8_TuneCUETP8M1	35.85	6952830
WWToLNuQQ_13TeV-powheg	49.997	18973950
WZTo1L1Nu2Q_13TeV_amcatnloFXFX_madspin_pythia8	10.73	24221923
DYJetsToLL_Pt-100To250_TuneCUETP8M1_13TeV-amcatnloFXFX-pythia8	81.22	83686174
DYJetsToLL_Pt-250To400_TuneCUETP8M1_13TeV-amcatnloFXFX-pythia8	2.991	21185045
DYJetsToLL_Pt-400To650_TuneCUETP8M1_13TeV-amcatnloFXFX-pythia8	0.388	1625936
DYJetsToLL_Pt-650ToInf_TuneCUETP8M1_13TeV-amcatnloFXFX-pythia8	0.037	1627882

Subtitle: Summary of the background samples used for the analysis as well as their cross sections and number of events.

Source: The author, 2019.

4 DATA ANALYSIS

For the analysis, it was used part of the 2016 CMS dataset. The data were collected from proton-proton collisions with 13 TeV center-of-mass energy and only certified data with PPS sensors inserted were considered. The data samples used in this study and their correspondent integrated luminosities are listed in table 7.

The analysis was split into two stages: in the inclusive stage the selection of the central objects considering the anomalous couplings scenario was performed using the analysis strategy from (CMS COLLABORATION, 2016b) as reference. The exclusive stage was performed to ensure the CEP topology of the process, it was done using mainly the tracking multiplicity in the central detector and the proton information in the PPS RPs. For the proton treatment the analysis procedures developed in the first PPS and joint CMS-TOTEM publication (CMS COLLABORATION et al., 2018), the internal note (CMS COLLABORATION., 2019), and the study (CMS AND TOTEM COLLABORATIONS, 2018) were followed.

4.1 **Inclusive Selection**

As mentioned above, the inclusive selection is based on the analysis (CMS COLLABORATION, 2016b), and the efficiencies, scale factors and some other cuts are based in the CMS Physics Object Groups recommendations for 2016 data. Also, a comparison between data and MC background in different regions was done to ensure the MC agreement with data.

Table 7 - 2016 data samples used in the analysis.

Dataset	data taking period	$\mathcal{L}(fb^{-1})$
`SingleMuon` RunB	11 May — 21 Jun	4.55
`SingleMuon` RunC	24 Jun — 4 Jul	1.59
`SingleMuon` RunG	14 Aug — 9 Sep	3.65
Total	—	9.79

Subtitle: Data samples and their respective data taking periods and integrated luminosities.
Source: The author, 2019.

4.1.1 Trigger

The data used in this analysis are required to pass in the High Level Trigger `HLT_Mu50_v*`, which selects events with at least one muon candidate with $p_T > 50$ GeV. This HLT is seeded by the Level 1 triggers `L1_SingleMu22` or `L1_SingleMu25`, which require events with at least one muon candidate with $p_T > 22$ GeV or $p_T > 25$ GeV respectively. The turn-on curve of the trigger efficiency was measured by the Muon POG[8], the minimum value of the muon p_T on the plateau was found to be 53 GeV.

The measured efficiency of the trigger is not 1 and not constant, therefore the Monte Carlo samples were corrected with scale factors (SF) binned in p_T and η. The SFs are also calculated by the CMS Collaboration.

4.1.2 Jets

As mentioned in section 2.2.3, the analysis used jets reconstructed with the anti-k_T algorithm and the CHS clustering technique. The jets are divided into two categories: AK4 and AK8 with a radius in the $\eta - \phi$ plane of 0.4 and 0.8 respectively. The AK8 jets are used to reconstruct the W bosons that decay hadronically and the AK4 jets are used to apply the b-tag veto.

The jets are required to have $p_T > 200$ GeV for the AK8 and $p_T > 30$ GeV for the AK4. Both jets categories are required to have $|\eta| < 2.4$ and pass the loose jet identification (jetId) as defined in section 2.2.3.3. A correction for the jet energy was applied, as it was also mentioned in section 2.2.3.3, with an additional residual correction for the data. Since the resolution of the jet energy is worse in data than in MC, a smearing was applied in the jet energy for the MC samples. The jets are also "cleaned" from muons with the geometric distance of $\Delta R \geq 1.0$. The parameters and the procedure to apply the kinematic selection, the jet Id selection, the jet energy correction, the jet energy smearing and the jet cleaning were made following the CMS JetMET POG[9] instructions.

To decrease the presence of $t\bar{t}$ events, the Combined Secondary Vertex algorithm was used to identify events with b-jets. Events with b-tagged AK4 jets were excluded, where only AK4 jets outside the hardest AK8 jet were considered. The tight working point of 0.935 for the discriminator (see figure 14 in section 2.2.3.3) was considered.

Due to the high energy of the W bosons in the aQGCs process, the jet substructure variables "pruned mass" and subjetiness (τ_{21}), described in section 2.2.3.3 were used. The selection of $\tau_{21} < 0.6$ was applied to select events where the jets come from highly boosted

[8] CMS Muon Physics Object Group. Obtained on the internal CMS web page.

[9] CMS Jet and Missing ET Physics Object Group. Obtained on the internal CMS web page.

particles as recommended by the JetMET POG. The pruned mass was also used to delimit the different control regions for background processes.

4.1.3 Muons

Events with one muon passing in the *HighPtMuon* identification criteria and an isolation requirement of 0.1, as described in the section 2.2.3.2, were selected. The muon has to pass the requiriments of $|\eta| < 2.4$ and $p_T > 53$ GeV (in order to be on the trigger efficiency plateau). To exclude events from Drell-Yan process, events with additional muons with the same selection but $p_T > 20$ GeV were vetoed.

Since the muon identification and isolation selection have different efficiency in data and Monte Carlo, scale factors to make the MC closer to the data description were applied. The SF are provided by the Muon POG of the CMS Collaboration.

4.1.4 Missing Transverse Energy (MET)

A cut of $E_T^{miss} > 40$ GeV was applied, where E_T^{miss} is defined in section 2.2.3.4. This selection is motivated by the reduction of QCD events. To remove events with noise effect or badly reconstructed, a set of filters were applied in data and Monte Carlo samples following the CMS Collaboration recommendations. The jet energy correction was also propagated to correct E_T^{miss}. This correction is called Type-I correction.

4.1.5 Baseline Event Selection

Additionally to the selection already listed, a set of cuts on the reconstructed W bosons were also applied. For the hadronic W reconstruction, the AK8 jet was used since it contains the full product of the W decay. For the leptonic W, the information of the MET and the muon were combined. The four-momentum of the leptonic W is defined as the vector sum of the muon and neutrino four-momentuma. The muon kinematic is known from the reconstruction, however, since the neutrinos are not directly detected in CMS, the MET was assumed to be entirely due to transverse momentum of the neutrinos. To estimate the longitudinal momentum of the neutrinos the W mass was used as a constraint, defined by:

$$m_W^2 = (p_\mu + p_\nu)^2 \ , \tag{29}$$

Table 8 - Inclusive baseline selection list.

Selection	value
Muon $p_T >$	53 GeV
Muon $\|\eta\| <$	2.4
Jet $p_T >$	200 GeV
Jet $\|\eta\| <$	2.4
$\tau_{21} <$	0.6
$E_T^{miss} >$	40 GeV
$m_{WW} >$	500 GeV
W leptonic $p_T >$	200 GeV
$\Delta\Phi(W_{hadronic}, W_{leptonic}) >$	2.0
$\Delta\Phi(jet, MET) >$	2.0

Subtitle: Summary of the selection applied in the analysis.
Source: The author, 2019.

where p_μ is the muon four-momentum defined by $p_\mu = (E_\mu, \mathbf{p}_\mu^T, p_\mu^z)$ and p_ν is the neutrino four-momentum defined by $p_\nu = (\sqrt{\mathbf{p}_\nu^{T2} + p_\nu^{z2}}, \mathbf{p}_\nu^T, p_\nu^z)$. Neglecting the muon mass, it is possible to write:

$$m_W^2 = 2p_\mu.p_\nu \ . \tag{30}$$

Taking the product and simplifying the expression, the equation 30 can be written as:

$$p_\nu^{z2}(p_\mu^{z2} - E_\mu^2) + 2kp_\mu^z p_\nu^z - E_\mu^2 \mathbf{p}_\nu^{T2} + k = 0 \ , \tag{31}$$

where, $k = \frac{m_W^2}{2} + \mathbf{p}_\mu^T.\mathbf{p}_\nu^T$. Solving the quadratic equation for p_ν^z and replacing p_ν^T for E_{miss}^T:

$$p_\nu^z = \frac{k.p_\mu^z}{p_\mu^{T2}} \pm \sqrt{\frac{k^2.p_\mu^{z2}}{p_\mu^{T4}} - \frac{E_\mu^2.E_{miss}^{T2} - k}{p_\mu^{T2}}} \ . \tag{32}$$

For a complex solution, only the real part is used. In case of two real solutions, the smaller one is used.

Once both W bosons are reconstructed, it is possible to define a cut on the invariant mass of the diboson final state, m_{WW}. Due to the high energy expected for the aQGCs WW production, a requirement of $m_{WW} > 500$ GeV was used. A selection on the leptonic W was also done, it was required the $p_T > 200$ GeV.

Due the back-to-back topology in the aQGCs WW process, a $\Delta\Phi(jet, MET) > 2.0$ and $\Delta\Phi(W_{hadronic}, W_{leptonic}) > 2.0$ requirement was also used. The complete set of selection cuts used is summarized in table 8.

Figure 28 - The control and WW regions.

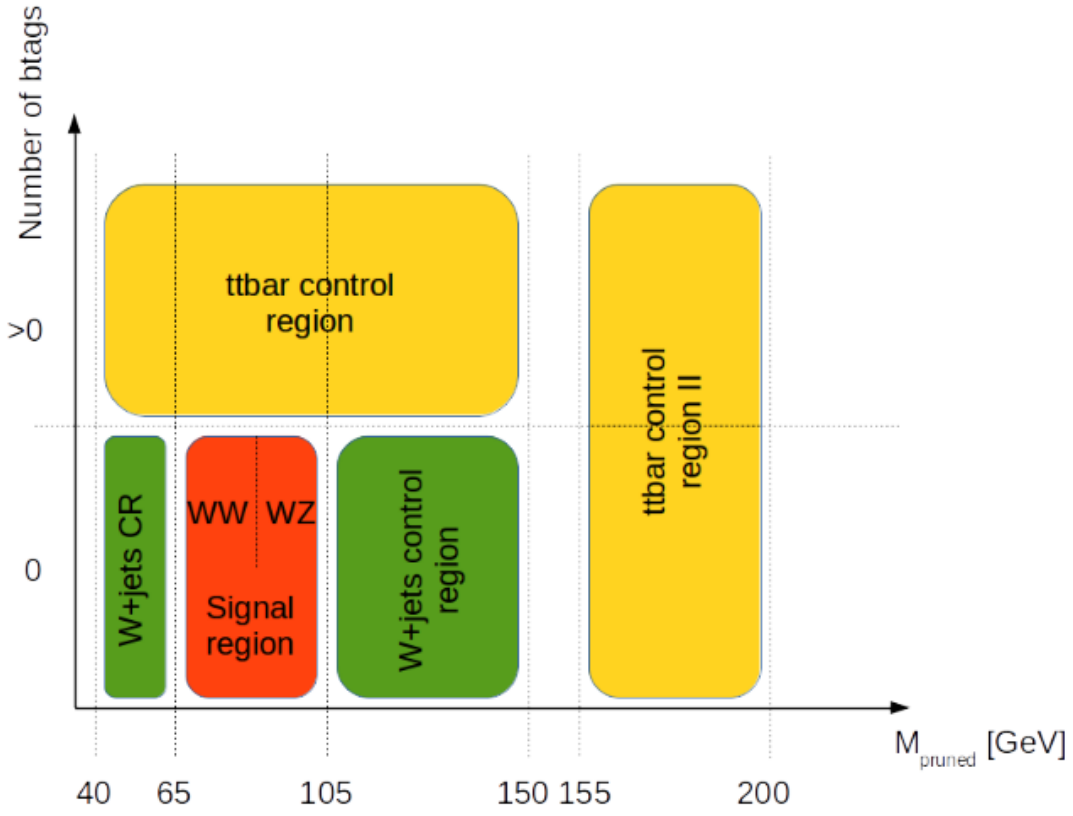

Subtitle: Schematic representation of the control and WW regions.

Source: Figure extracted from CMS COLLABORATION, 2016b, p. 9.

4.1.6 Pileup reweighting

Monte Carlo samples and data do not have the same pileup conditions. To correct this, a procedure to bring the MC to the same level of pileup as data is applied. This procedure, called "reweighting" follows standard recommendations from the CMS Collaboration.

4.1.7 Data and MC Comparison

The events were split into different regions in order to check the description of the two main backgrounds, $W + Jets$ and $t\bar{t}$, and the region where the signal is contained. The division of these regions can be seen in figure 28. To define these regions the pruned mass and b-tagging discriminant were used.

The agreement between data and MC is observed in the kinematic distributions

of jet p_T, muon p_T, missing transverse energy, WW central mass, jet τ_{21} and jet pruned mass. Additional kinematic distributions for all control regions are shown in appendix B. Only statistical uncertainty is included in the plots.

The data and MC comparison for the $W + Jets$ control region is shown in figure 29. The selection described in section 4.1 was used in these plots with pruned mass sideband selection (40 GeV $< M_{pruned} <$ 65 GeV or 105 GeV $< M_{pruned} <$ 150 GeV) and no b-tagged events.

The plots of $t\bar{t}$ control region I are shown in figure 30. For these plots the selection described in section 4.1 was used with the pruned mass window 40 GeV $< M_{pruned} <$ 150 GeV and one or more b-tagged jets.

The plots of $t\bar{t}$ control region II can be seen in figure 31. The selection described in section 4.1 was used in these plots with pruned mass window 155 GeV $< M_{pruned} <$ 200 GeV and no b-tagging requirements.

The inclusive WW region is the most important since it includes the signal and the inclusive WW events, which is the process with the topology closer to the signal. The data and MC comparison for this region is shown in figure 32. The selection described in section 4.1 was used in these plots with pruned mass window 65 GeV $< M_{pruned} <$ 105 GeV and zero b-tagged events.

Table 9 shows the expected number of events for background and the number of events in data after the selection described in section 4.1.

4.2 **Central Exclusive Production**

The samples listed in the table 5 were used for the signal study. The kinematic distributions for signal samples are presented in figure 33. Four sets of aQGC parameters were used for the plots.

To discriminate signal and background, the extra track multiplicity, the information of the scattered protons and the p_T of the Ws were used as follows.

4.2.1 Track Multiplicity

In inclusive processes one (or both) of the interacting protons fragments, giving origin to many particles that may be eventually identified by the detector as tracks or even forming jets. In CEP processes with the requirement of double proton tag this does not happen, then the track multiplicity has to be much smaller than in the inclusive case.

An extra track is defined as a track coming from the primary vertex (or close) and outside the centrally produced objects: the AK8 jet and a cone with a radius equal to

Figure 29 - Data and MC comparison for $W + Jets$ Control Region.

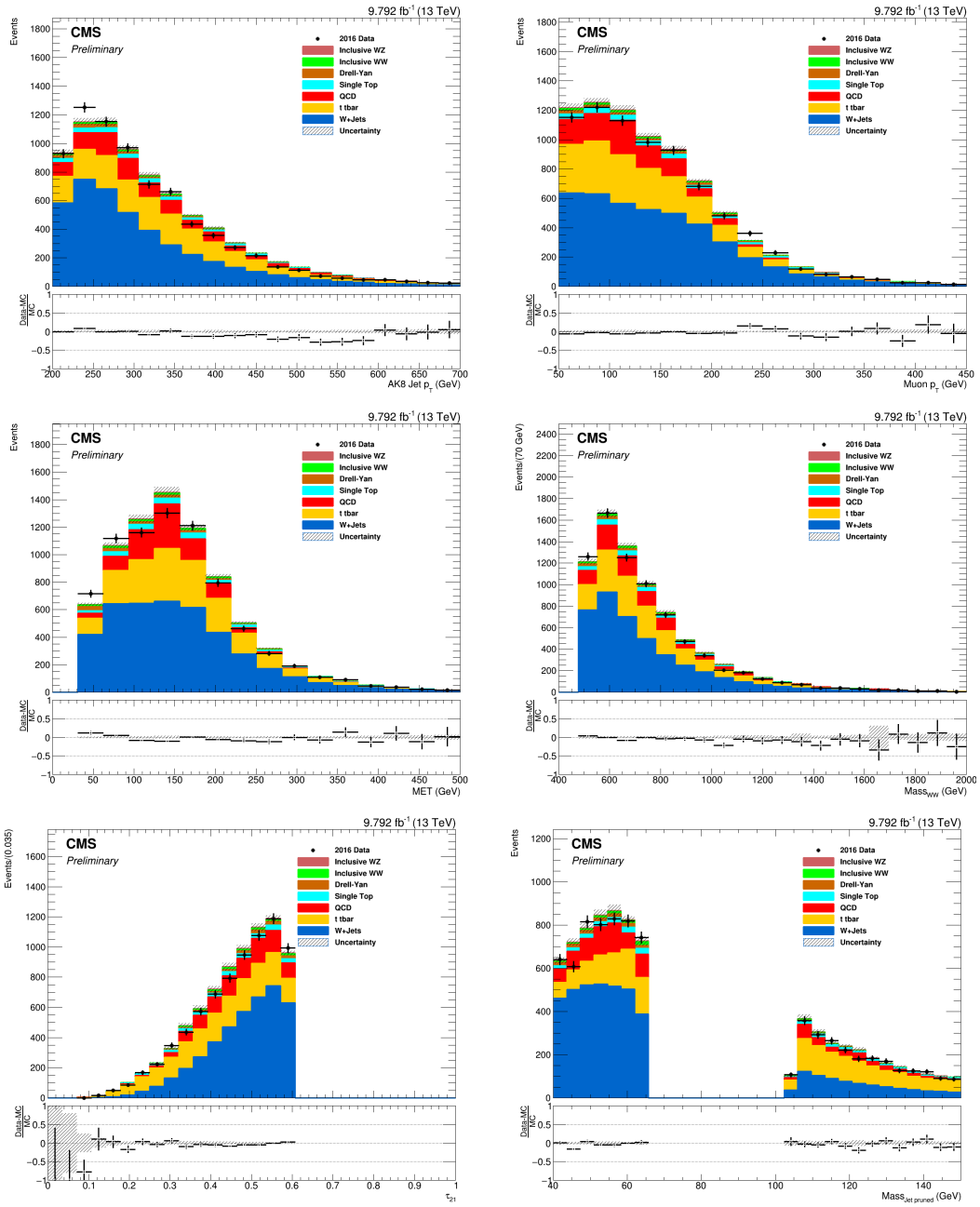

Subtitle: Comparison between data and MC of jet p_T (top left), muon p_T (top right), missing transverse energy (middle left), WW central mass (middle right), the jet τ_{21} (bottom left) and the jet pruned mass (bottom right).

Source: The Author, 2019.

Figure 30 - Data and MC comparison for $t\bar{t}$ Control Region I.

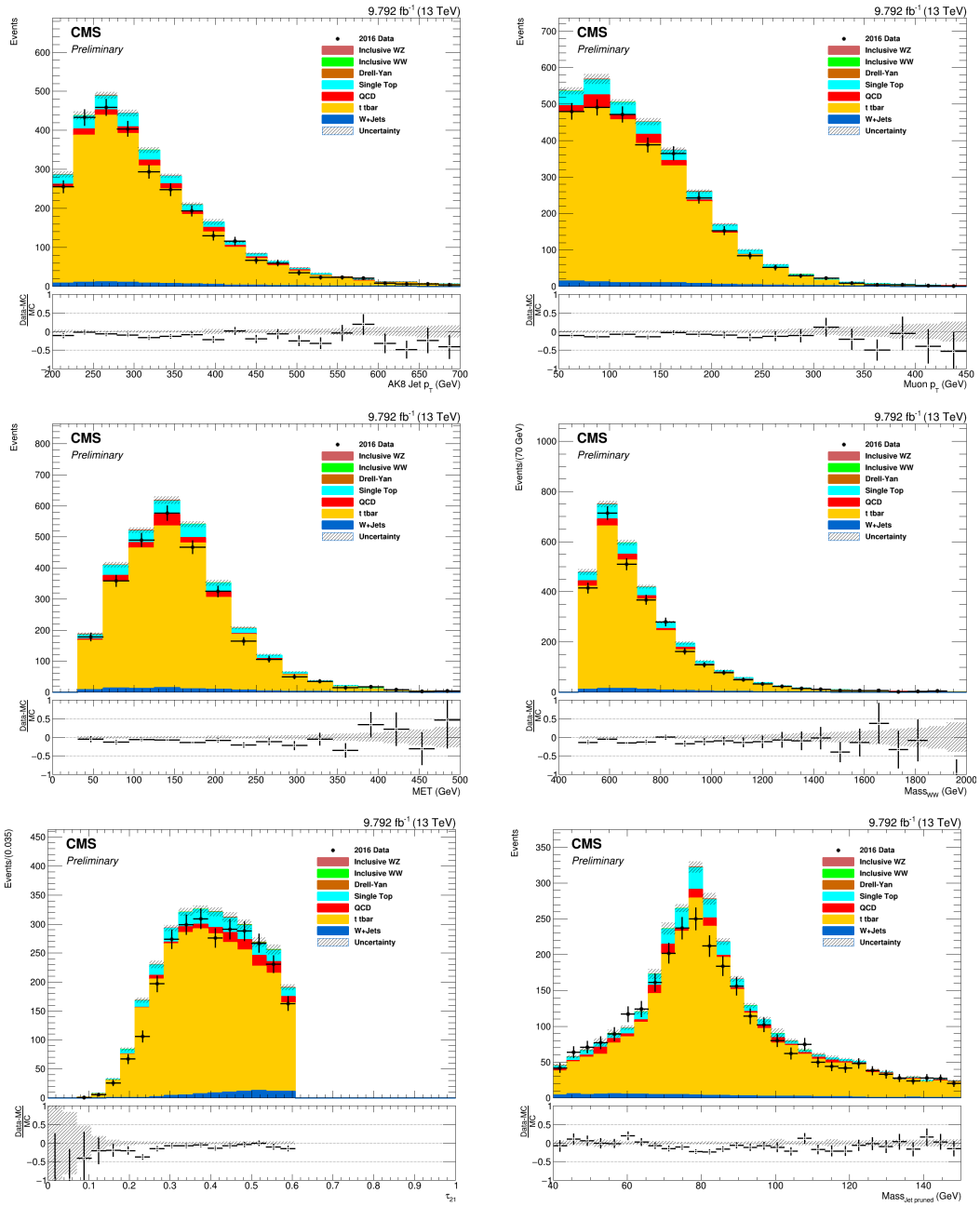

Subtitle: Comparison between data and MC of jet p_T (top left), muon p_T (top right), missing transverse energy (middle left), WW central mass (middle right), the jet τ_{21} (bottom left) and the jet pruned mass (bottom right).

Source: The author, 2019.

Figure 31 - Data and MC comparison for $t\bar{t}$ Control Region II.

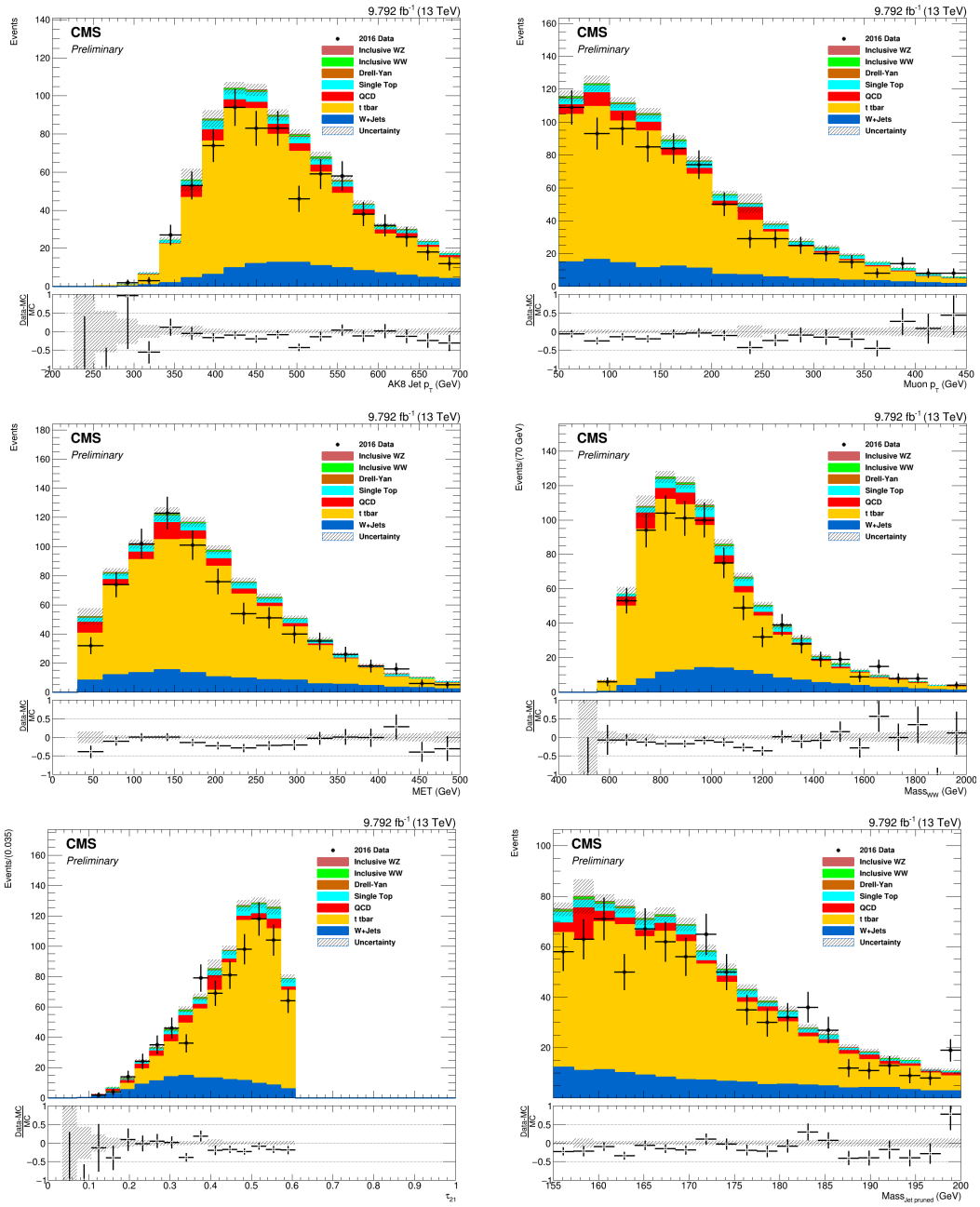

Subtitle: Comparison between data and MC of jet p_T (top left), muon p_T (top right), missing transverse energy (middle left), WW central mass (middle right), the jet τ_{21} (bottom left) and the jet pruned mass (bottom right).

Source: The author, 2019.

Table 9 - Number of events in each control region.

	$W + jets$ CR	$t\bar{t}$ CR I	$t\bar{t}$ CR II	WW inclusive region
$W + jets$	4388 ± 22	90 ± 3	138 ± 4	3311 ± 19
$t\bar{t}$	2123 ± 15	2735 ± 17	664 ± 9	3632 ± 20
QCD	1021 ± 68	125 ± 20	51 ± 10	910 ± 64
Single t	279 ± 7	251 ± 1	45 ± 2	563 ± 9
Drell-Yan	165 ± 2	5.0 ± 0.2	5.1 ± 0.2	125 ± 1
Inclusive WW	109 ± 2	4.1 ± 0.3	6.2 ± 0.4	312 ± 3
Inclusive WZ	41.6 ± 0.5	5.4 ± 0.2	3.7 ± 0.1	105 ± 1
Total MC	8126 ± 116	3215 ± 47	913 ± 24	8959 ± 116
Data	7880	2899	789	9130

Subtitle: Expected number of events for each background process and data in each control region using the integrated luminosity of 9.79 fb^{-1}. The statistical uncertainty is also presented.

Source: The author, 2019.

Figure 32 - Data and MC comparison for inclusive WW region.

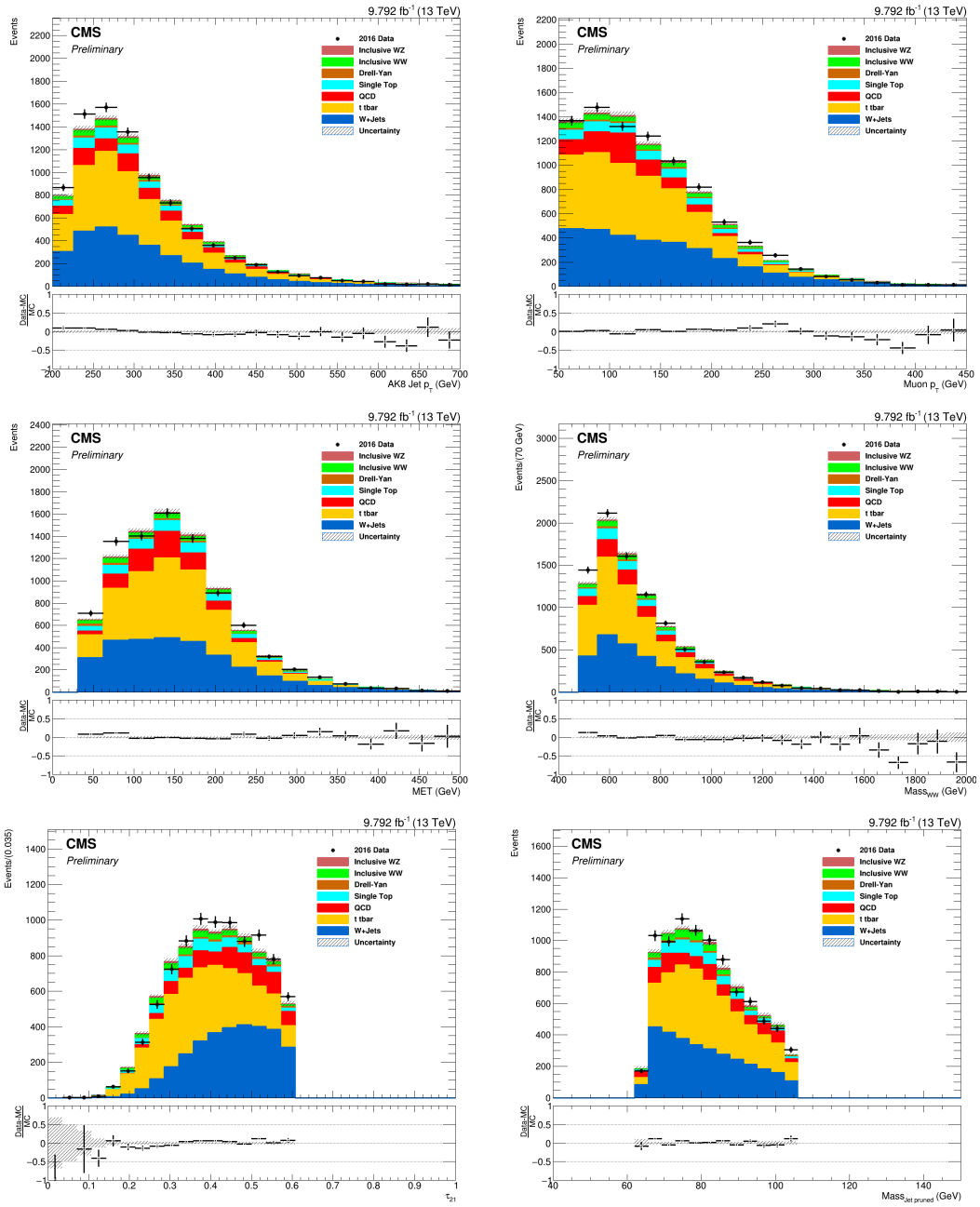

Subtitle: Comparison between data and MC of jet p_T (top left), muon p_T (top right), missing transverse energy (middle left), WW central mass (middle right), the jet τ_{21} (bottom left) and the jet pruned mass (bottom right).

Source: The author, 2019.

Figure 33 - AQGCs signal MC distributions.

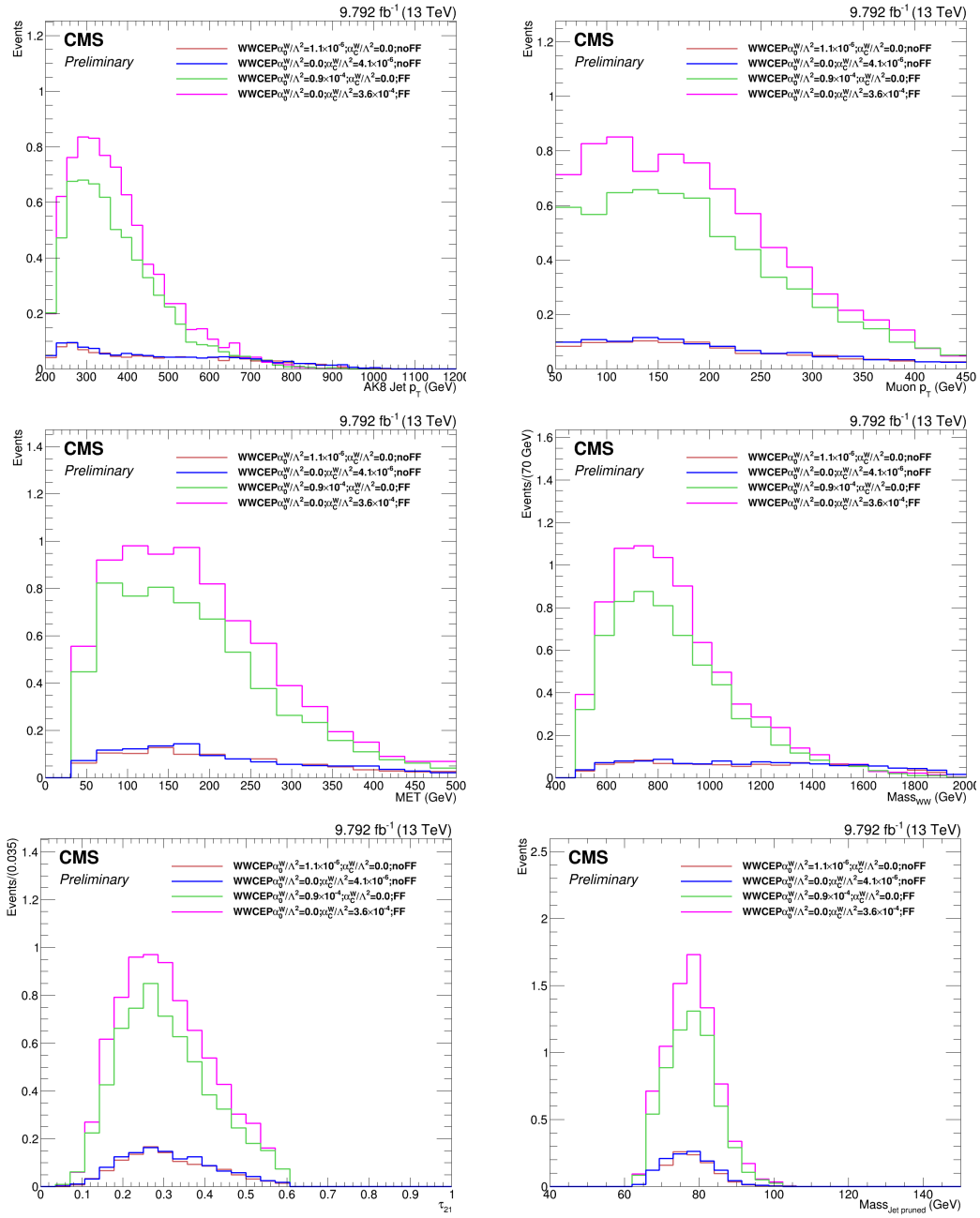

Subtitle: Distribution for signal events: jet p_T (top left), muon p_T (top right), missing transverse energy (middle left), WW central mass (middle right), the jet τ_{21} (bottom left) and the jet pruned mass (bottom right).

Source: The author, 2019.

Figure 34 - Extra track multiplicity distribution before the reweighting.

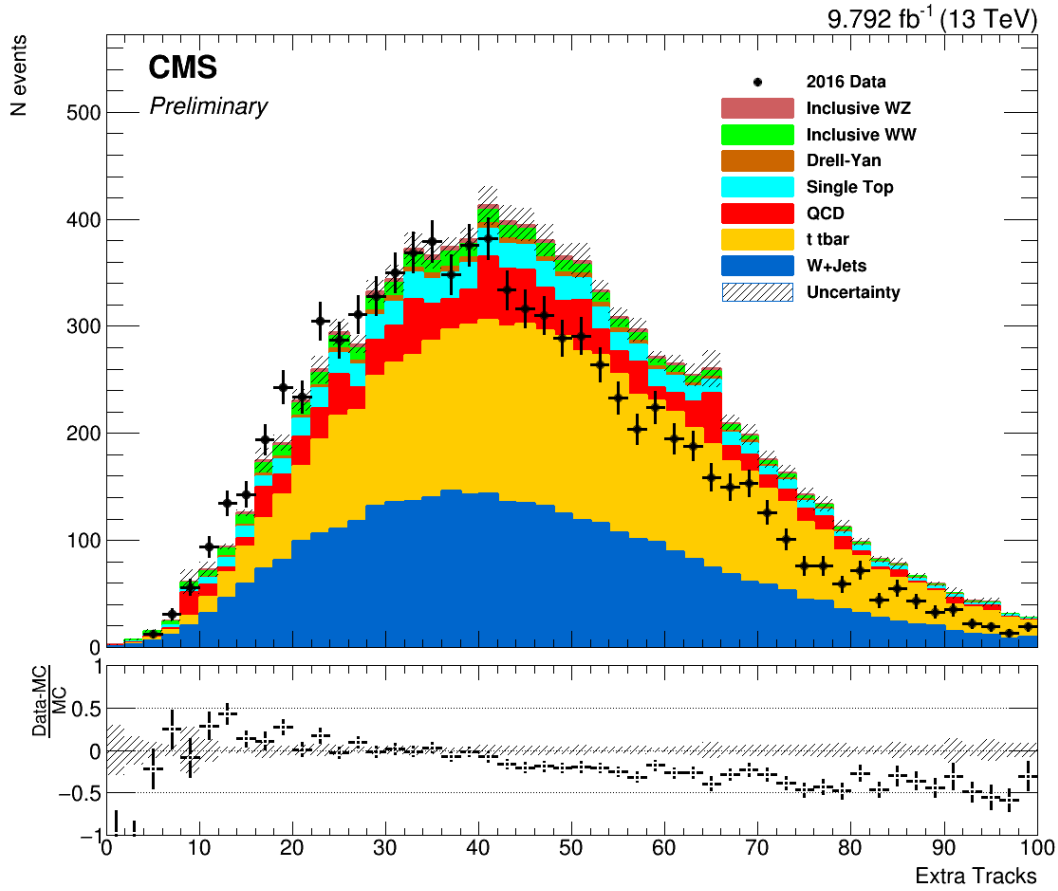

Subtitle: Comparison between data and background MC before the extra track multiplicity reweighting. Data in the signal region is kept blinded.

Source: The author, 2019.

0.3 around the muon. Only the tracks identified as charged particles and the tracks that were used for the fit of the primary vertex were considered in the analysis.

The signal region is defined as having less than 5 extra tracks. The data in the signal region are kept blinded to avoid eventual bias. In figure 34 there is a comparison between data and MC in the extra track distribution. It is possible to see a considerable discrepancy between data and MC. A study on the dependence of this discrepancy with the p_T of the tracks and the distance between the track and the primary vertex in z coordinate was performed and no correlation was found, the plots of this study are presented in the appendix B.

The background MC events were reweighted taking into account the extra track distribution to correctly describe the data. The data and MC comparison is showed in figure 35 in addition to four signal samples. It is possible to observe that the signal events are concentrated in the low extra track multiplicity region.

Figure 35 - Extra track multiplicity distribution after the reweighting.

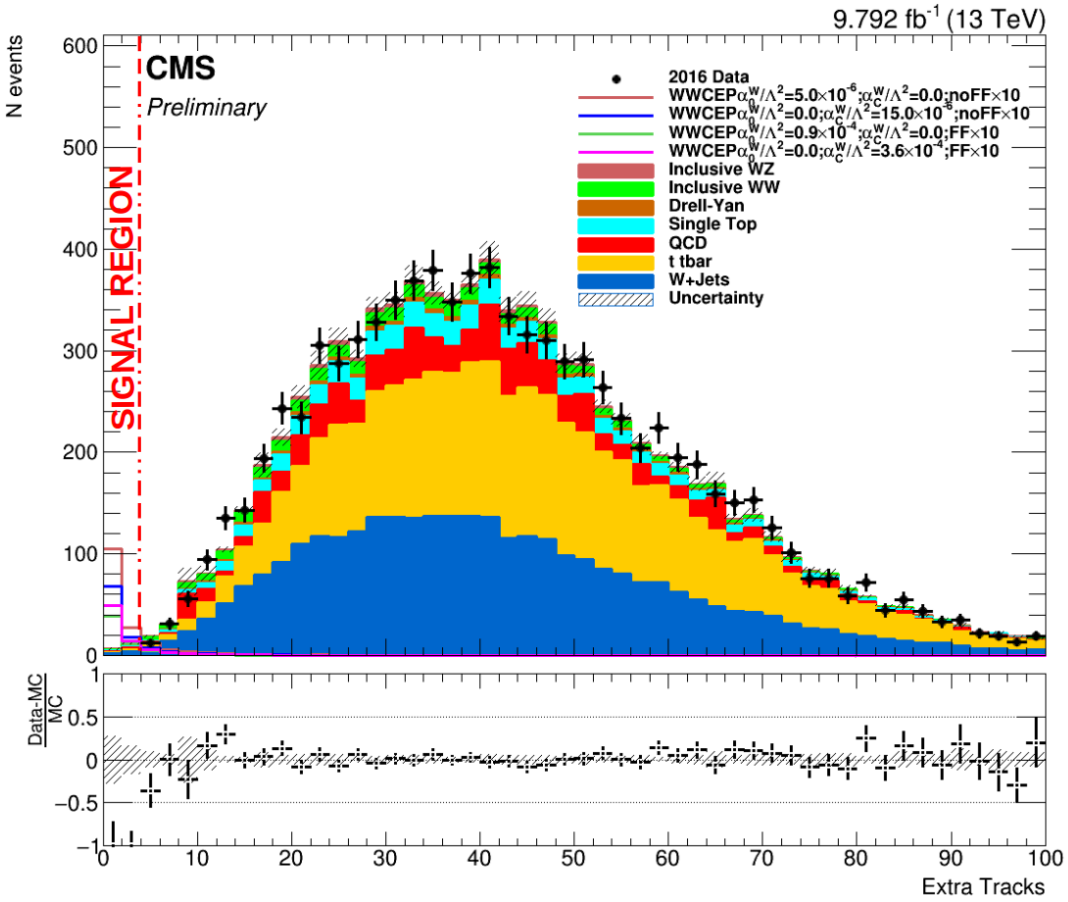

Subtitle: Comparison between data and background MC after the extra track multiplicity reweighting, four signal samples were included. Data in the signal region is kept blinded. The signal samples were multiplied by a factor of 10.

Source: The author, 2019.

Figure 36 - Generated ξ distributions.

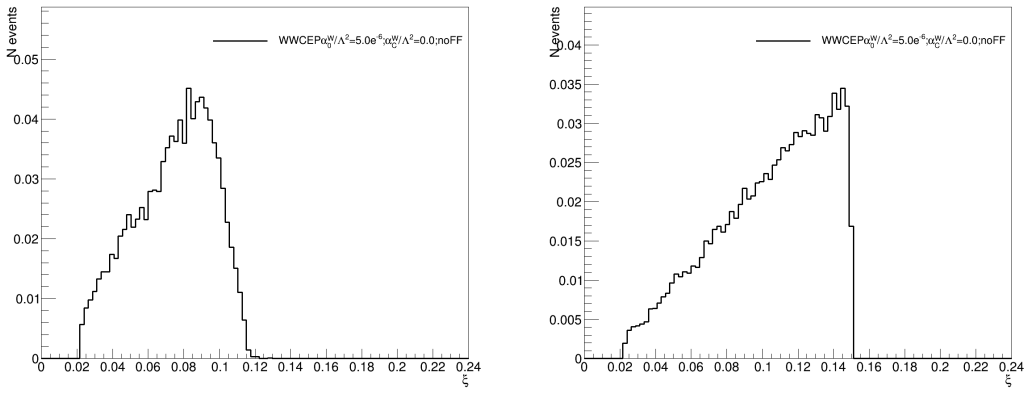

Subtitle: Signal sample generated ξ distribution corresponding to sector 45 (left) and sector 56 (right).

Source: The author, 2019.

4.2.2 The fractional momentum loss of the scattered protons

As mentioned in section 1.3, it is possible to estimate the mass of the central system (M_X) using the proton fractional momentum loss, ξ. For CEP WW processes, the ratio between the central mass calculated with the central objects (M_{WW}) and the central mass estimated with the proton information, $\frac{M_{WW}}{M_X}$, should be around one.

Since the tagged proton information in the background processes comes from random pileup protons, the mass ratio is a good signal-background discriminator. The understanding of the proton information in the data is very important for an accurate signal-background discrimination. This analysis follows the proton treatment developed in the analysis (CMS COLLABORATION et al., 2018).

The generator level ξ distributions for both PPS arms are shown in figure 36. For these distributions the sample with $\alpha_0^W/\Lambda^2 = 5.0 \times 10^{-6}$ GeV^{-2},$\alpha_C^W/\Lambda^2 = 0.0$ and no form factor was used. As mentioned before, the ξ range used in the generation was 0.02 to 0.15, and it is possible to observe for sector 45 that the ξ goes up to around 0.12. This happens due to the acceptance of the detector (the simulation keeps the proton generated information if it is reconstructed). The reconstruction level ξ distributions for all RPs are shown in figure 37. The same sample as for generator level plots was used.

The ξ correlation between generation and reconstruction level, using the same signal sample as before, for all RPs is presented in the figure 38.

As mentioned in section 2.4.2, after some data taking period the sensors started to present an inefficiency in the proton reconstruction. This inefficiency is higher when the track impact point is closer to the beam position. In other words, the inefficiency is high for low values of ξ. Since the signal simulation does not include this effect, it

Figure 37 - Reconstructed ξ distributions.

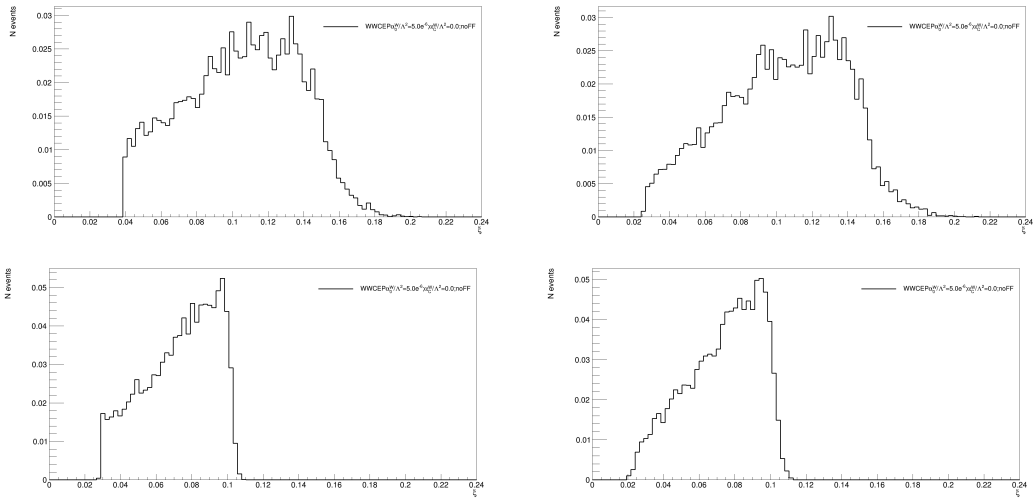

Subtitle: Signal sample reconstructed ξ distribution corresponding to sector 56 near (top left), sector 56 far (top right), sector 45 near (bottom left) and sector 45 far (bottom right).

Source: The author, 2019.

Figure 38 - Generated versus reconstructed ξ distribution.

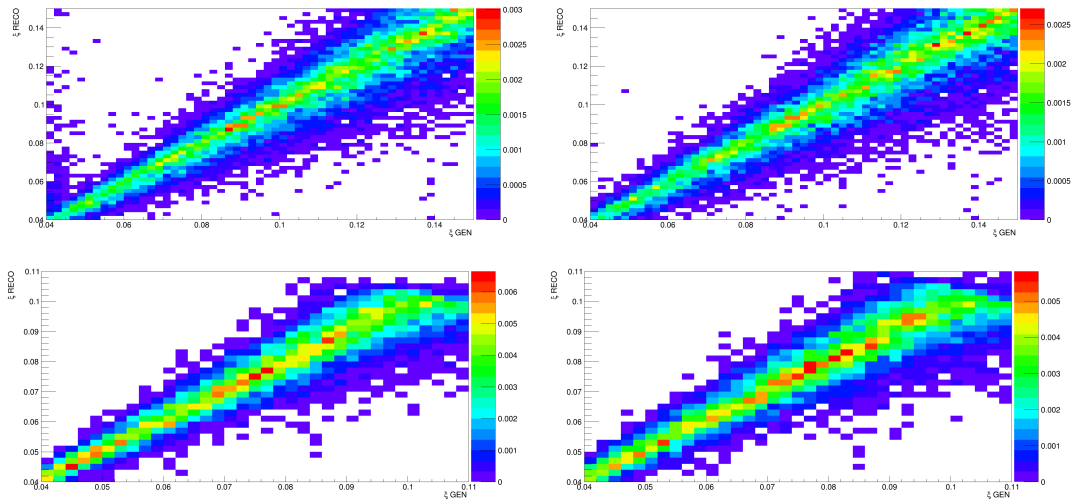

Subtitle: Signal sample Generated versus reconstructed ξ distribution corresponding to sector 56 near (top left), sector 56 far (top right), sector 45 near (bottom left) and sector 45 far (bottom right).

Source: The author, 2019.

Table 10 - Cuts on the proton ξ.

Roman Pot	minimum value of ξ
Sector 45, near	0.067
Sector 45, far	0.066
Sector 56, near	0.070
Sector 56, far	0.061

Subtitle: ξ cut values extracted from (CMS COLLABORATION., 2019) to decrease the radiation damage impact to less than 10%.

Source: The author, 2019.

Figure 39 - 2016 data multi-tracking inefficiency.

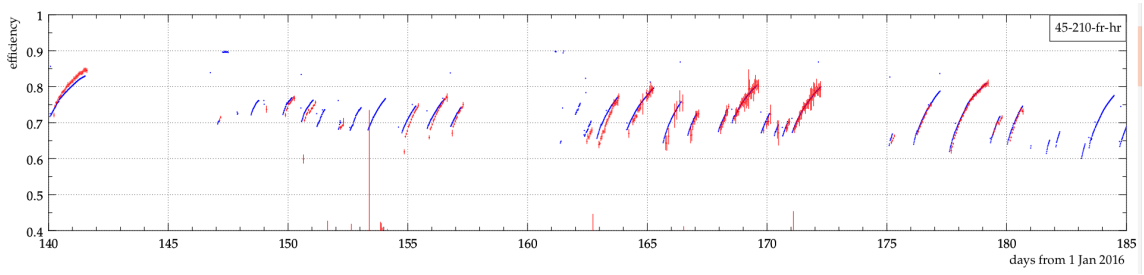

Subtitle: Comparison between the multi-tracking efficiency (in red) and the primary vertices multiplicity (in blue). The blue dots are a linear transformation of the mean primary vertex multiplicity in the time slice.

Source: Figure extracted from CMS AND TOTEM COLLABORATIONS, 2018, p. 4.

is important to avoid it on data analysis. A set of cuts on ξ was found to decrease the radiation damage inefficiency to less than 10% in the study (CMS COLLABORATION., 2019). These values are presented in table 10.

The inefficiency due to the multi-tracking in the RPs for 2017 data was discussed briefly in section 2.4.3. The comparison between the multi-tracking efficiency and the primary vertex multiplicity for 2016 data can be seen in figure 39, which it was extracted from (CMS AND TOTEM COLLABORATIONS, 2018), it is possible to note a correlation between the multi-tracking efficiency and the primary vertex multiplicity. Based on this, the efficiency was assumed as constant around 70% and applied for each PPS arm in the signal samples.

The M_X distribution is presented in figure 40, comparing background simulation with data and four signal simulated samples for different combinations of anomalous couplings. The mass ratio distribution is presented in figure 41. For both plots the selection described in section 4.1 with pruned mass window 65 GeV $< M_{pruned} <$ 105 GeV and no b-tagged events were used. Again, the data is kept blinded in the signal

Figure 40 - M_X distribution.

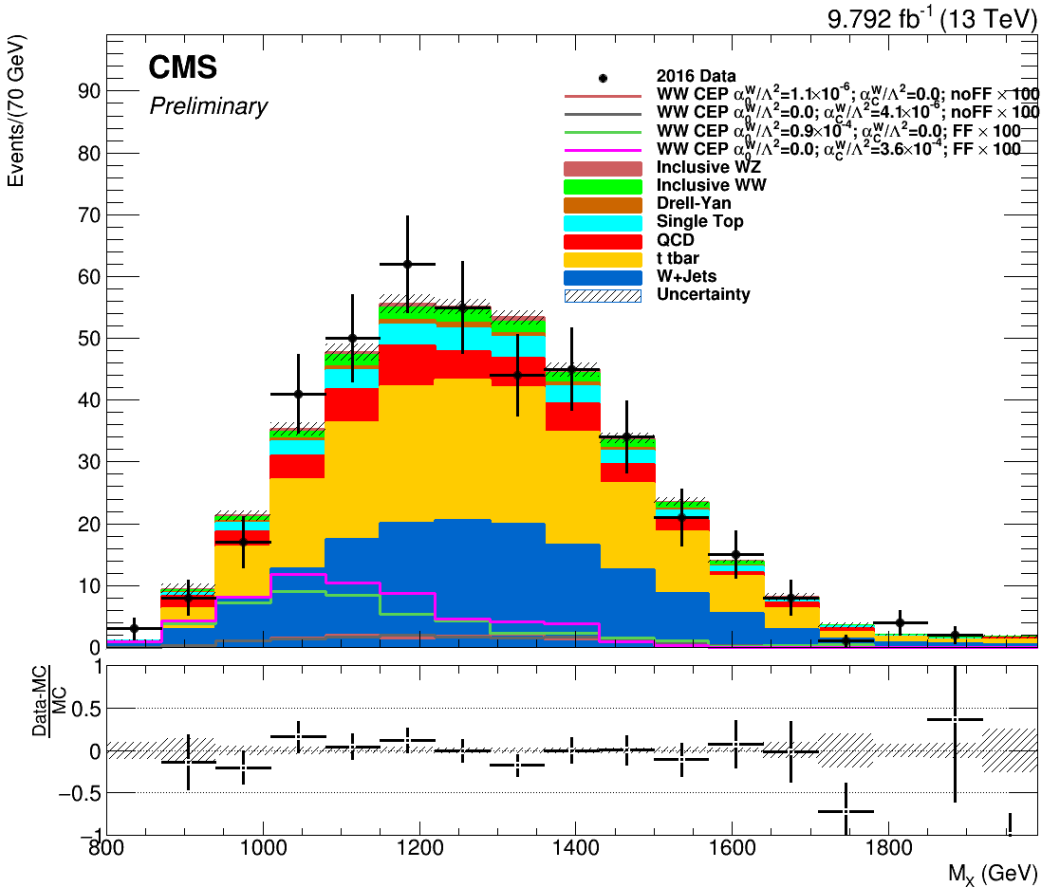

Subtitle: Comparison between data and MC for M_X in the inclusive WW region, four signal samples included. The signal samples were multiplied by a factor of 100.

Source: The author, 2019.

region which is defined as $\frac{M_{WW}}{M_X} > 0.8$. Using also the extra track selection, the $\frac{M_{WW}}{M_X}$ distribution for background and signal simulation is presented in figure 42. The signal correction for proton multi-tracking inefficiency and the selection to decrease the radiation damage impact was considered.

4.3 **Final Selection**

Using the signal region defined before, it is possible to observe the distribution of the p_T of the leptonic and hadronic W bosons in figures 43 and 44, respectively. There could be an additional way to discriminate signal and background: since the p_T of the W bosons are not correlated in the background, but on the other hand they present a great correlation in the signal, a cut on W p_T was defined as higher than 350 GeV for both W

Figure 41 - $\frac{M_{WW}}{M_X}$ distribution.

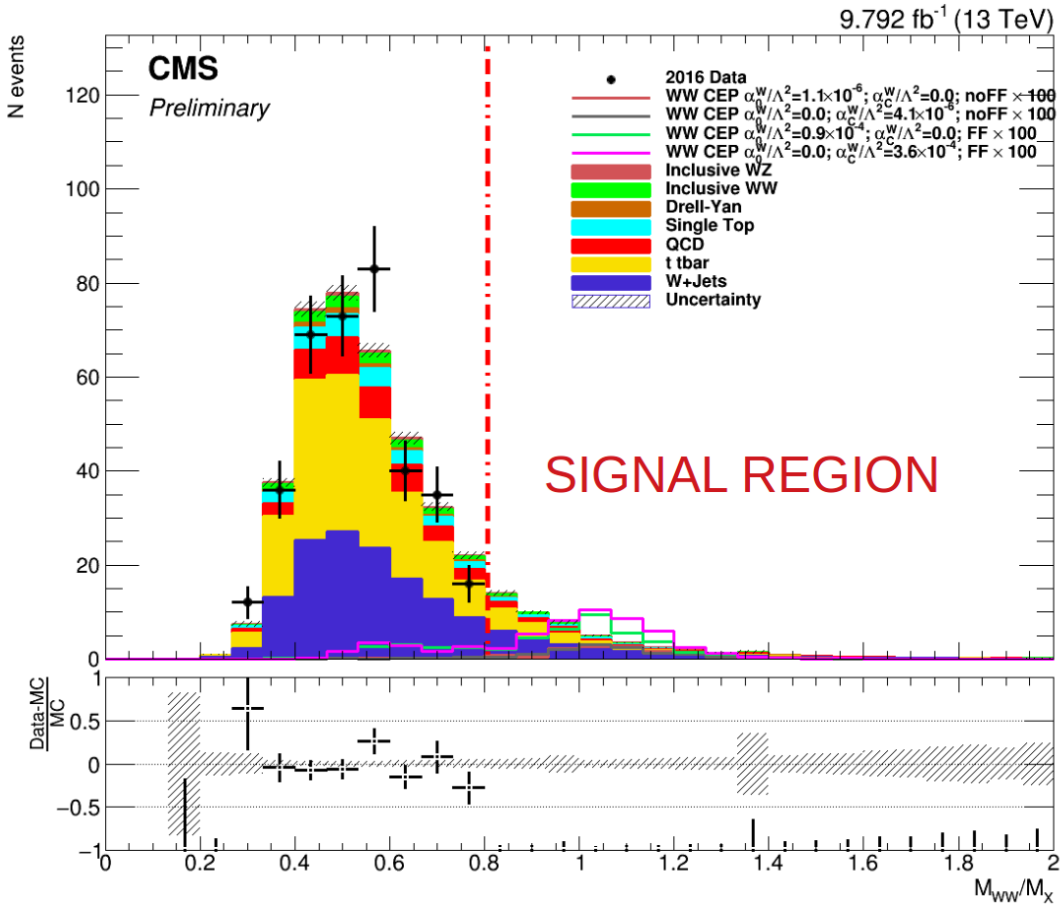

Subtitle: Comparison between data and MC for $\frac{M_{WW}}{M_X}$ in the inclusive WW region, four signal samples included. Data in the signal region is kept blinded. The signal samples were multiplied by a factor of 100.

Source: The author, 2019.

Figure 42 - $\frac{M_{WW}}{M_X}$ distribution after extra track selection.

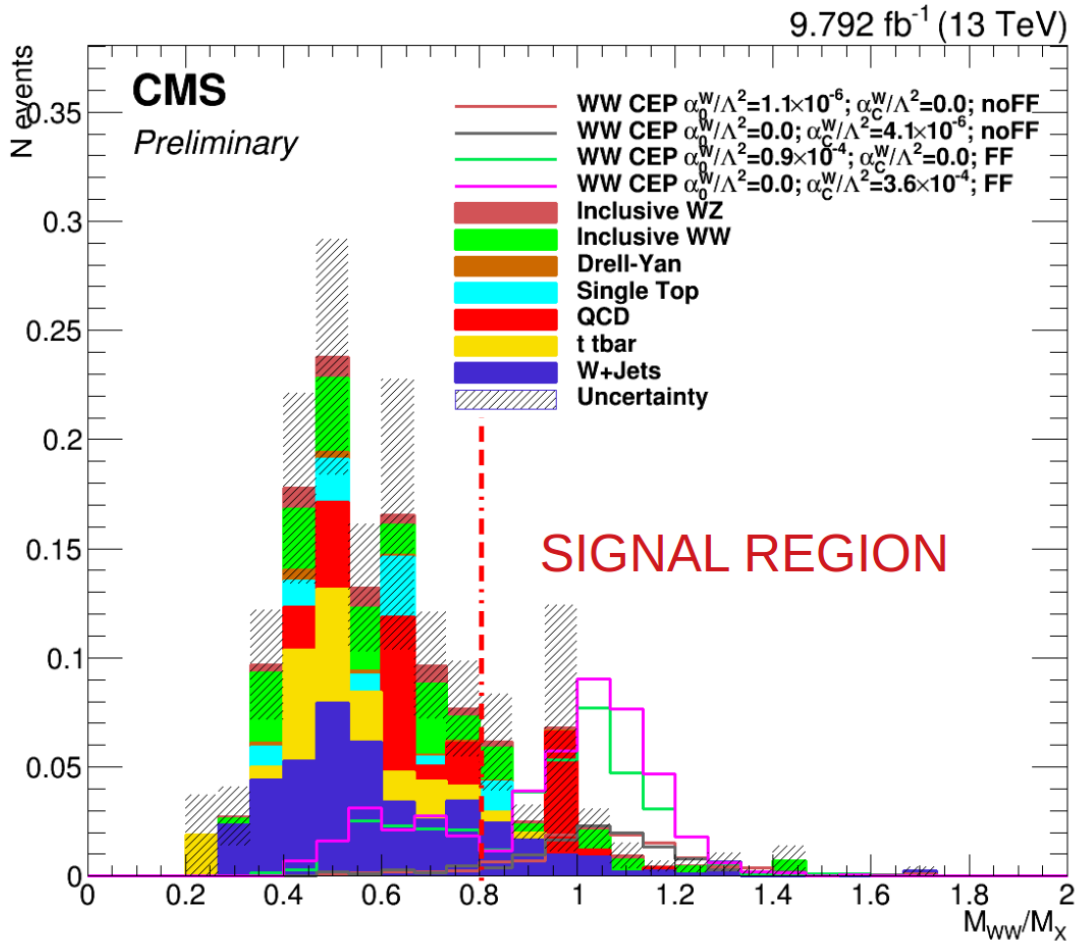

Subtitle: Distribution of $\frac{M_{WW}}{M_X}$ in the inclusive WW region with extra tracks ≤ 4, for four signal samples and background MC.

Source: The author, 2019.

Figure 43 - p_T distribution for the W leptonic decay.

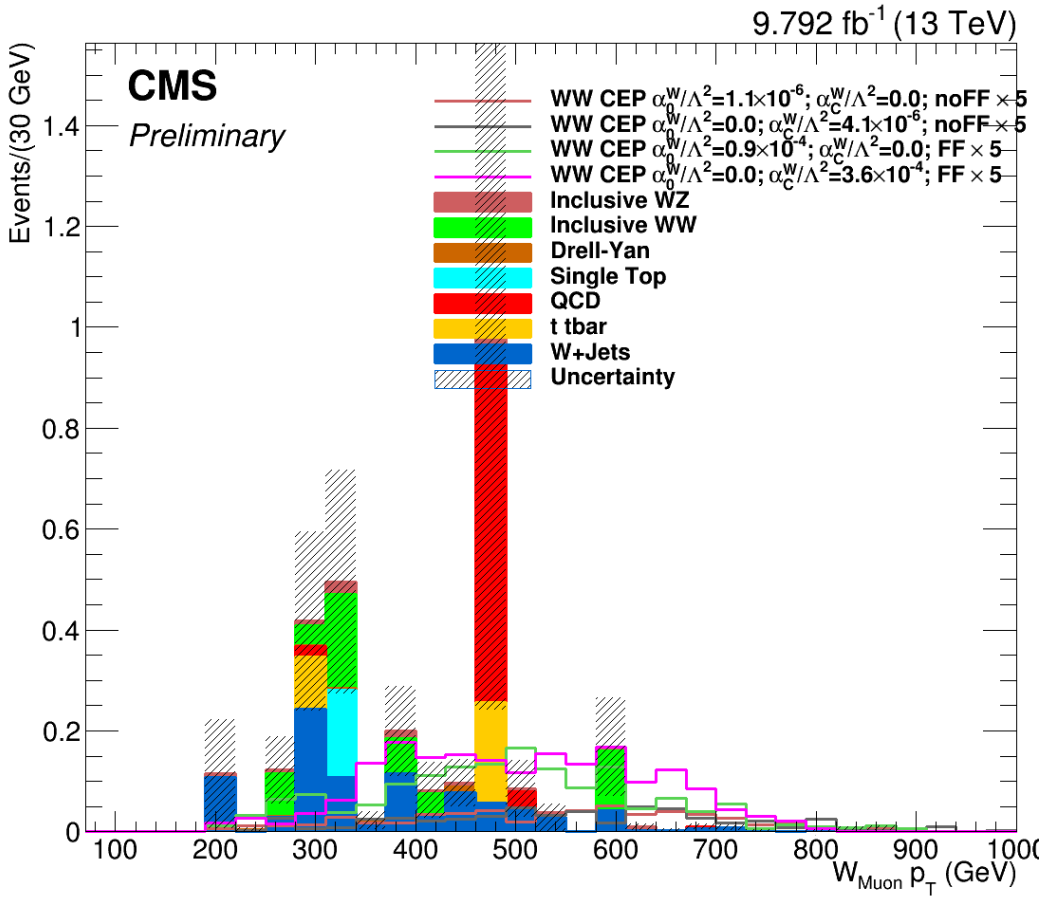

Subtitle: Distribution of the leptonic W p_T in the inclusive WW region with extra tracks ≤ 4 and $\frac{M_{WW}}{M_X} > 0.8$, for four signal samples and background MC. The signal samples were multiplied by a factor of 5.

Source: The author, 2019.

bosons as the final selection.

The expected number of events for signal and background is presented in table 11, where the expected number after each final selection is shown, the numbers in each column are for the cumulative cuts. The statistical uncertainty is also presented. For data, no event is left after all the selection cuts are applied.

4.4 **Results**

Since the analysis was made to study the viability of the WW aQGCs search for the LHC Run II, is important to understand how to evaluate limits for the aQGC parameters. The Poisson law description can be used to describe a counting experiment with a small

Figure 44 - Hadronic W p_T distribution.

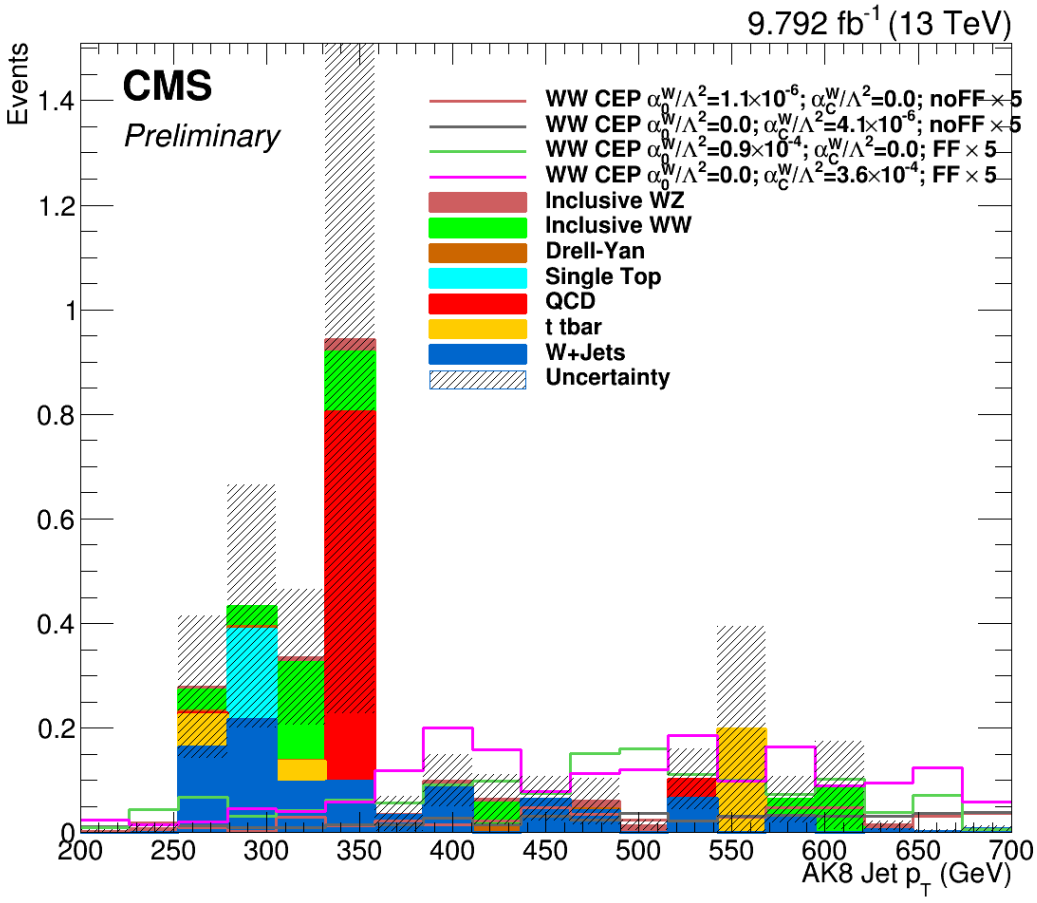

Subtitle: Distribution of the hadronic W p_T in the inclusive WW region with extra tracks ≤ 4 and $\frac{M_{WW}}{M_X} > 0.8$, for four signal samples and background MC. The signal samples were multiplied by a factor of 5.

Source: The author, 2019.

Table 11 - Expected number of events.

	WW region	extra track multiplicity ≤ 4	$\frac{M_{WW}}{M_X} > 0.8$	Ws $p_T > 350$ GeV
Background	8959 ± 117	28 ± 5	0.2 ± 0.1	0.07 ± 0.04
WW CEP SM	0.43 ± 0.01	0.35 ± 0.01	0.020 ± 0.003	0.010 ± 0.002
WW CEP aQGC ; no FF $\alpha_0^W/\Lambda^2 = 1.1 \times 10^{-6}$ GeV^{-2} , $\alpha_C^W/\Lambda^2 = 0.0$	1.16 ± 0.03	0.97 ± 0.02	0.10 ± 0.01	0.09 ± 0.01
WW CEP aQGC ; no FF $\alpha_0^W/\Lambda^2 = 2.5 \times 10^{-6}$ GeV^{-2} , $\alpha_C^W/\Lambda^2 = 0.0$	4.42 ± 0.06	3.74 ± 0.06	0.51 ± 0.02	0.46 ± 0.02
WW CEP aQGC ; no FF $\alpha_0^W/\Lambda^2 = 5.0 \times 10^{-6}$ GeV^{-2} , $\alpha_C^W/\Lambda^2 = 0.0$	16.6 ± 0.2	14.1 ± 0.2	2.20 ± 0.06	2.01 ± 0.06
WW CEP aQGC ; no FF $\alpha_0^W/\Lambda^2 = 0.0$, $\alpha_C^W/\Lambda^2 = 4.1 \times 10^{-6}$ GeV^{-2}	1.27 ± 0.03	1.09 ± 0.03	0.11 ± 0.01	0.10 ± 0.01
WW CEP aQGC ; no FF $\alpha_0^W/\Lambda^2 = 0.0$, $\alpha_C^W/\Lambda^2 = 10.0 \times 10^{-6}$ GeV^{-2}	5.1 ± 0.1	4.3 ± 0.1	0.62 ± 0.02	0.57 ± 0.02
WW CEP aQGC ; no FF $\alpha_0^W/\Lambda^2 = 0.0$, $\alpha_C^W/\Lambda^2 = 15.0 \times 10^{-6}$ GeV^{-2}	10.9 ± 0.1	9.3 ± 0.1	1.39 ± 0.04	1.30 ± 0.04
WW CEP aQGC ; FF $\alpha_0^W/\Lambda^2 = 0.9 \times 10^{-4}$ GeV^{-2} , $\alpha_C^W/\Lambda^2 = 0.0$	6.3 ± 0.1	5.3 ± 0.1	0.29 ± 0.02	0.25 ± 0.02
WW CEP aQGC ; FF $\alpha_0^W/\Lambda^2 = 5.0 \times 10^{-4}$ GeV^{-2} , $\alpha_C^W/\Lambda^2 = 0.0$	181 ± 2	154 ± 2	9.3 ± 0.5	8.2 ± 0.4
WW CEP aQGC ; FF $\alpha_0^W/\Lambda^2 = 10.0 \times 10^{-4}$ GeV^{-2} , $\alpha_C^W/\Lambda^2 = 0.0$	741 ± 8	629 ± 7	38 ± 2	35 ± 2
WW CEP aQGC ; FF $\alpha_0^W/\Lambda^2 = 0.0$, $\alpha_C^W/\Lambda^2 = 3.6 \times 10^{-4}$ GeV^{-2}	8.0 ± 0.1	6.8 ± 0.1	0.37 ± 0.02	0.32 ± 0.02
WW CEP aQGC ; FF $\alpha_0^W/\Lambda^2 = 0.0$, $\alpha_C^W/\Lambda^2 = 10.0 \times 10^{-4}$ GeV^{-2}	56 ± 1	48 ± 1	3.0 ± 0.1	2.7 ± 0.1
WW CEP aQGC ; FF $\alpha_0^W/\Lambda^2 = 0.0$, $\alpha_C^W/\Lambda^2 = 15.0 \times 10^{-4}$ GeV^{-2}	125 ± 1	106 ± 1	5.9 ± 0.3	5.2 ± 0.3

Subtitle: Expected number of events for each final selection steps. Is presented the numbers for different signal samples points and the total background.

Source: The author, 2019.

number of events, then the probability of observing n events with $(s+b)$ expected events is:

$$P(n;s,b) = \frac{(s+b)^n}{n!} e^{-(s+b)} \ , \tag{33}$$

where n is the number of observed events in the experiment, s is the expected number of events for signal and b is the expected number of events for background.

For the case of the current analysis, the probability of the observation of zero events given a model that predicts 0.07 background events and s signal events can be written as:

$$P(0;s,0.07) = e^{-(s+0.07)} \ . \tag{34}$$

This model would be excluded at 95% confidence level if the probability of observing 1 or more events with was higher than 95%. This can be expressed by the inequality:

$$P(0;s,0.07) < 1 - 0.95 \ , \tag{35}$$

using (34),

$$e^{-(s+0.07)} < 0.05 \ , \tag{36}$$

or finally:

$$s > 2.93 \ . \tag{37}$$

This means that a set of aQGC parameters that predicts more than 2.93 expected events for the current selection can be excluded at 95% of C.L.. Looking at table 11, it is possible to exclude the aQGC parameters: $\alpha_0^W/\Lambda^2 > 5.0 \times 10^{-4}$ GeV^{-2} and $\alpha_C^W/\Lambda^2 > 15.0 \times 10^{-4}$ GeV^{-2}, considering a form factor of 500 GeV with 95% C.L..

CONCLUSIONS AND PROSPECTS

The WW Central Exclusive Production analysis using the CMS 2016 data with an integrated luminosity of 9.79 fb^{-1} was presented. The semileptonic decay channel was used considering the muon as the lepton. The study showed that with the data collected in 2016 is not possible to improve the aQGC limits already established.

In spite of the mentioned limited sensitivity, it is possible to conclude that they can be reached considering all Run II dataset, about 100 fb^{-1} of integrated luminosity with the PPS Roman Pots inserted. Moreover for this kind of analysis, the electron as the lepton in the semileptonic channel can be considered. Another improvement for 2017 and 2018 data analyses is the presence of new technologies introduced in the PPS apparatus.

A very simple approximation can give an idea about how much more data will be needed in order to improve the limits on this analysis. On table 11, in the values for aQGCs of the current limits, $\alpha_C^W/\Lambda^2 = 3.6 \times 10^{-4}$ GeV^{-2} and $\alpha_0^W/\Lambda^2 = 0.9 \times 10^{-4}$ GeV^{-2}, the expected number of events for 9.79 fb^{-1} are 0.32 and 0.25 respectively. With Run II data with the PPS sensors inserted (around 100 fb^{-1}), a simple multiplication by 10 on the aQGCs current limits the expected number of events shows that it could be possible to explore the physics beyond these limits.

In additional, the electron channel could be used combined with the muon one. It could provide up to a maximum of two times the number of expected events compared to only using the muon channel. As it is known, the electron has more noise in its identification than the muon, then the electron channel probably will be less effective than the muon one. But even so it could improve the search for aQGCs in the semileptonic channel.

As presented in appendix A, different technologies were introduced in the PPS apparatus after the 2016 dataset. In 2017, two Roman Pots, one in each side, had the strip sensors replaced by pixel sensors, which have better ξ resolution and they are more resistant to radiation damage and with a multi-track identification capability. Also in 2017, timing detectors were included in both PPS arms, which give another method to discriminate signal and background using the protons time-of-flight. In 2018, all tracking RPs used the pixel technology and the timing detector was improved. With the PPS upgrade, considering the smaller impact of the radiation damage and the time-of-flight discriminator, the WW CEP analysis could have more significant results, since the proton characterization is the key to identify a CEP process.

The fact of the expected number of background events being smaller than one, even when projecting to the total luminosity for Run II, is another interesting point for this analysis, even more, compared with the previous analysis that were performed with fewer data. It shows how this kind of analysis can be important to improve the searches

for anomalous couplings for the WW production.

A complete analysis with 2016+2017 data is being performed, using both muon and electron channel, with the purpose of making the results public in 2019. The viability to perform the WW CEP aQGCs search with this kind of analysis opens the possibility also to use the same idea on the ZZ CEP aQGCs search, which will be performed by the CMS Collaboration.

REFERENCES

AALTONEN, T. et al. Diffractive dijet production in $\overline{p}p$ collisions at $\sqrt{s}$=1.96 TeV. *Phys. Rev. D*, American Physical Society, [s. l.], v. 86, p. 032009, Aug 2012.

ABBIENDI, Giovanni. The CMS muon system in Run2: preparation, status and first results. *PoS*, [s. l.], EPS-HEP2015, p. 237, 2015.

ACHARD, P. et al. Study of the W+W process and limits on anomalous quartic gauge boson couplings at LEP. *Physics Letters B*, [s. l.], v. 527, n. 1, p. 29 – 38, 2002. ISSN 0370-2693.

AGOSTINELLI, S. et al. Geant4—a simulation toolkit. *Nuclear Instruments and Methods in Physics Research Section A: Accelerators, Spectrometers, Detectors and Associated Equipment*, [s. l.], v. 506, n. 3, p. 250 – 303, 2003. ISSN 0168-9002.

ALBROW, M et al. *CMS-TOTEM Precision Proton Spectrometer*. [s. l.], 2014.

ALEPH COLLABORATION. A precise determination of the number of families with light neutrinos and of the Z boson partial widths. *Physics Letters B*, [s. l.], v. 235, n. 3, p. 399 – 411, 1990. ISSN 0370-2693.

ALICE COLLABORATION. The ALICE experiment at the CERN LHC. *Journal of Instrumentation*, IOP Publishing, [s. l.], v. 3, n. 08, p. S08002–S08002, aug 2008.

ALWALL, J. et al. The automated computation of tree-level and next-to-leading order differential cross sections, and their matching to parton shower simulations. *Journal of High Energy Physics*, [s. l.], v. 2014, n. 7, p. 79, Jul 2014. ISSN 1029-8479.

ALWALL, Johan et al. MadGraph 5 : Going Beyond. *JHEP*, [s. l.], v. 06, p. 128, 2011.

ATLAS COLLABORATION. The ATLAS Experiment at the CERN Large Hadron Collider. *Journal of Instrumentation*, IOP Publishing, [s. l.], v. 3, n. 08, p. S08003–S08003, aug 2008.

_____. Observation of a new particle in the search for the Standard Model Higgs boson with the ATLAS detector at the LHC. *Physics Letters B*, [s. l.], v. 716, n. 1, p. 1 – 29, 2012. ISSN 0370-2693.

_____. Measurement of exclusive $\gamma\gamma$ -> W+W- production and search for exclusive *H*iggs boson production in pp collisions at sqrts=8 TeV using the ATLAS detector. *Phys. Rev. D*, American Physical Society, [s. l.], v. 94, p. 032011, Aug 2016.

BANERJEE, S. CMS Simulation Software. *Journal of Physics: Conference Series*, IOP Publishing, [s. l.], v. 396, n. 2, p. 022003, dec 2012.

BEHN, W. A. *The CMS Detector and the Token Bit Manager*. [S.l.]: Online Material; https://www.phys.ksu.edu/reu2014/wabehn/, 2014. [Online; Accessed 2019-03-01].

BENAGLIA, A. The CMS ECAL performance with examples. *Journal of Instrumentation*, [s. l.], v. 9, n. 02, p. C02008, feb 2014.

BERINGER, J. et al. Review of Particle Physics. *Phys. Rev. D.*, American Physical Society, [s. l.], v. 86, p. 1528, 2012.

BOONEKAMP, M. et al. FPMC: A Generator for forward physics. [s. l.], 2011.

BOONEKAMP, M.; KúCS, T. DPEMC: A Monte Carlo for double diffraction. *Computer Physics Communications*, [s. l.], v. 167, n. 3, p. 217 – 228, 2005. ISSN 0010-4655.

BUCHMULLER, W.; WYLER, D. Effective Lagrangian Analysis of New Interactions and Flavor Conservation. *Nucl. Phys.*, [s. l.], B268, p. 621–653, 1986.

BéLANGER, G.; BOUDJEMA, F. Probing quartic couplings of weak bosons through three vector production at a 500 GeV NLC. *Physics Letters B*, [s. l.], v. 288, n. 1, p. 201 – 209, 1992. ISSN 0370-2693.

CACCIARI, Matteo; SALAM, Gavin P; SOYEZ, Gregory. The anti-ktjet clustering algorithm. *Journal of High Energy Physics*, Springer Nature, [s. l.], v. 2008, n. 04, p. 063–063, apr 2008.

CERN. *The CERN accelerator complex*. [S.l.]: Online Material; https://cds.cern.ch/record/1260465, 2008. [Online; Accessed 2019-03-01].

CMS AND TOTEM COLLABORATIONS. Efficiency of Si-strips sensors used in Precision Proton Spectrometer. [s. l.], Sep 2018.

CMS COLLABORATION. The CMS Experiment at the CERN LHC. *Journal of Instrumentation*, [s. l.], v. 3, n. 08, p. S08004, 2008.

_____. Observation of a new boson at a mass of 125 *GeV* with the CMS experiment at the LHC. *Physics Letters B*, [s. l.], v. 716, n. 1, p. 30 – 61, 2012. ISSN 0370-2693.

_____. Study of exclusive two-photon production of W+W in pp collisions at sqrts=7 TeV and constraints on anomalous quartic gauge couplings. *Journal of High Energy Physics*, [s. l.], v. 2013, n. 7, p. 116, Jul 2013. ISSN 1029-8479.

_____. Evidence for exclusive $\gamma\gamma$ -> W+W production and constraints on anomalous quartic gauge couplings in pp collisions at sqrts=7 and 8 TeV. *Journal of High Energy Physics*, [s. l.], v. 2016, n. 8, p. 119, Aug 2016a. ISSN 1029-8479.

_____. *Search for anomalous couplings in semileptonic WW and WZ decays at sqrt(s) = 13 TeV*. Geneva, 2016b.

_____. *PPS Commissioning 2017*. [S.l.]: Online Material; https://indico.cern.ch/event/688548/contributions/2826086/, 2017. [Online; Accessed 2019-03-01].

_____. *CMS Detector Design*. [S.l.]: Online Material; https://cms.cern/news/cms-detector-design, 2018a. [Online; Accessed 2019-03-01].

_____. *CMS Luminosity - Public Results*. [S.l.]: Online Material; https://twiki.cern.ch/twiki/bin/view/CMSPublic/LumiPublicResults, 2018b. [Online; Accessed 2019-03-01].

CMS COLLABORATION. *Limits on anomalous triple and quartic gauge couplings*. [S.l.]: Online Material; https://twiki.cern.ch/twiki/bin/view/CMSPublic/PhysicsResultsSMPaTGC, 2018c. [Online; Accessed 2019-03-01].

_____. Diphoton production via photon-photon fusion with forward protons in CT-PPS at 13 TeV . [s. l.], Feb 2019.

CMS COLLABORATION et al. Observation of proton-tagged, central (semi)exclusive production of high-mass lepton pairs in pp collisions at 13 TeV with the CMS-TOTEM precision proton spectrometer. *Journal of High Energy Physics*, [s. l.], v. 2018, n. 7, p. 153, Jul 2018. ISSN 1029-8479.

CORCELLA, Gennaro et al. HERWIG 6: an event generator for hadron emission reactions with interfering gluons (including supersymmetric processes). *Journal of High Energy Physics*, Springer Nature, [s. l.], v. 2001, n. 01, p. 010–010, jan 2001.

D0 COLLABORATION. Search for anomalous quartic WW->$\gamma\gamma$ couplings in dielectron and missing energy final states in $p\overline{p}$ collisions at sqrts=1.96TeV. *Phys. Rev. D*, American Physical Society, [s. l.], v. 88, p. 012005, Jul 2013.

DOBBS, M. A. et al. Les Houches guidebook to Monte Carlo generators for hadron collider physics. In: *Physics at TeV colliders. Proceedings, Workshop, Les Houches, France, May 26-June 3, 2003*. [s. l.]: [s.n.], 2004. p. 411–459.

ENGLERT, François; BROUT, Robert. Broken Symmetries and the Mass of Gauge Vector Mesons. *Phys. Rev. Lett.*, [s. l.], v. 13, n. 9, p. 321–323, 1964.

FAVEREAU, J. de; ROUBY, X.; PIOTRZKOWSKI, K. Hector: A Fast simulator for the transport of particles in beamlines. *JINST*, [s. l.], v. 2, p. P09005, 2007.

FRüHWIRTH, R. Application of Kalman filtering to track and vertex fitting. *Nuclear Instruments and Methods in Physics Research Section A: Accelerators, Spectrometers, Detectors and Associated Equipment*, [s. l.], v. 262, n. 2, p. 444 – 450, 1987. ISSN 0168-9002.

GARGAMELLE NEUTRINO COLLABORATION. Observation of neutrino like interactions without muon or electron in the Gargamelle neutrino experiment. *Phys. Rev. Lett.*, [s. l.], v. 46, n. 1, p. 138–140, 1973.

GLASHOW, Sheldon L. Partial-symmetries of weak interactions. *Nuclear Physics*, [s. l.], v. 22, n. 4, p. 579 – 588, 1961. ISSN 0029-5582.

GRZADKOWSKI, B. et al. Dimension-six terms in the Standard Model Lagrangian. *Journal of High Energy Physics*, [s. l.], v. 2010, n. 10, p. 85, Oct 2010. ISSN 1029-8479.

HALZEN, F.; MARTIN, Alan D. *Quarks and leptons: an introductory course in modern particle physics*. [s. l.]: [s.n.], 1984. ISBN 0471887412, 9780471887416.

HIGGS, P. Broken Symmetries and the Masses of Gauge Bosons. *Phys. Rev. Lett.*, [s. l.], v. 13, n. 16, p. 508–509, 1964.

KASPAR, J. Alignment of CT-PPS detectors in 2016, before TS2. [s. l.], Mar 2017.

LANGACKER, Paul. Grand Unified Theories and Proton Decay. *Phys. Rept.*, [s. l.], v. 72, p. 185, 1981.

LHCB COLLABORATION. The LHCb Detector at the LHC. *Journal of Instrumentation*, IOP Publishing, [s. l.], v. 3, n. 08, p. S08005–S08005, aug 2008.

LHCF COLLABORATION. The LHCf detector at the CERN Large Hadron Collider. *Journal of Instrumentation*, IOP Publishing, [s. l.], v. 3, n. 08, p. S08006–S08006, aug 2008.

LOCCI, E. Status of W and Z physics in the UA1 and UA2 experiments. [s. l.], n. CERN-EP-86-159, p. 24, 1986.

MARTIN, STEPHEN P. A SUPERSYMMETRY PRIMER. In: *Perspectives on Supersymmetry*. [s. l.]: [s.n.], 1998. p. 1–98.

NEMES, F. LHC optics determination with proton tracks measured in the CT-PPS detectors in 2016, before TS2. [s. l.], Mar 2017.

PIERZCHAŁA, T.; PIOTRZKOWSKI, K. Sensitivity to anomalous quartic gauge couplings in photon-photon interactions at the LHC. *Nuclear Physics B - Proceedings Supplements*, [s. l.], v. 179-180, p. 257 – 264, 2008. ISSN 0920-5632. Proceedings of the International Workshop on High-Energy Photon Collisions at the *LHC*.

PINFOLD, J L. The MoEDAL Experiment at the LHC –a New Light on the Terascale Frontier. *Journal of Physics: Conference Series*, IOP Publishing, [s. l.], v. 631, p. 012014, jul 2015.

RANDALL, Lisa; SUNDRUM, Raman. Large Mass Hierarchy from a Small Extra Dimension. *Phys. Rev. Lett.*, American Physical Society, [s. l.], v. 83, p. 3370–3373, Oct 1999.

RE, Emanuele. Single-top Wt-channel production matched with parton showers using the POWHEG method. *The European Physical Journal C*, [s. l.], v. 71, n. 2, p. 1547, Feb 2011. ISSN 1434-6052.

SADROZINSKI, H.F.-W. et al. Ultra-fast silicon detectors (UFSD). *Nuclear Instruments and Methods in Physics Research Section A: Accelerators, Spectrometers, Detectors and Associated Equipment*, [s. l.], v. 831, p. 18 – 23, 2016. ISSN 0168-9002. Proceedings of the 10th International "Hiroshima" Symposium on the Development and Application of Semiconductor Tracking Detectors.

SALAM, Abdus. Weak and Electromagnetic Interactions. *Conf. Proc.*, [s. l.], C680519, p. 367–377, 1968.

SIRUNYAN, A.M. et al. Particle-flow reconstruction and global event description with the CMS detector. *Journal of Instrumentation*, IOP Publishing, [s. l.], v. 12, n. 10, p. P10003–P10003, oct 2017.

SIRUNYAN, A. M. et al. Identification of heavy-flavour jets with the CMS detector in pp collisions at 13 TeV. *JINST*, [s. l.], v. 13, n. 05, p. P05011, 2018.

SJOSTRAND, Torbjorn; MRENNA, Stephen; SKANDS, Peter Z. A Brief Introduction to PYTHIA 8.1. *Comput. Phys. Commun.*, [s. l.], v. 178, p. 852–867, 2008.

SOUZA, Sandro Fonseca De. *Development and Integration of the CT-PPS Fast Simulation in the CMS Software*. Geneva, 2017.

TOTEM COLLABORATION. The TOTEM Experiment at the CERN Large Hadron Collider. *Journal of Instrumentation*, IOP Publishing, [s. l.], v. 3, n. 08, p. S08007–S08007, aug 2008.

WEINBERG, Steven. A Model of Leptons. *Phys. Rev. Lett.*, American Physical Society, [s. l.], v. 19, p. 1264–1266, Nov 1967.

APPENDIX A – PPS Apparatus

Different PPS configurations were used in each 2016, 2017 and 2018 data taking where it was recorded around 10 fb^{-1}, 40 fb^{-1} and 46 fb^{-1} of integrated luminosity with the Roman Pots inserted respectively.

A.1 **PPS Apparatus on 2017**

In 2017 the PPS apparatus was composed by tree Roman Pots in each arm. The tracking RPs was placed at 213 m (near station) and 220 m (far station), a Timing RP was placed at 216 m. In the near station it was used the Silicon Strip sensors, similar to 2016 configuration, and in the far station it was used the 3D Pixel Silicon sensors, which is more resistant to radiation damage and able to distinguish multi-track events.

For the first time PPS took data for physical analysis with timing of flight measurements. The timing sensors were composed by three planes of single scCVD Diamonds (single-crystal Chemical Vapor Deposition Diamond) technology and one plane with Ultra Fast Silicon Detectors technology.

A.2 **PPS Apparatus on 2018**

In 2018, the RPs were placed in the same position as 2017, however in the near RP, the silicon strip sensors were replaced by the Pixel one. The timing configuration was replaced by two single plus two double scCVD Diamonds planes, which resulted in a better timing resolution.

APPENDIX B – Additional Plots

On this appendix, additional plots of kinematics quantities are presented. Data and MC comparison for all control regions and signal MC distributions are presented in figures 45 to 49. The plots of the extra track multiplicity study using a cut on the track p_T or dz is presented in the figures 50 and 51 respectively.

Figure 45 - Data and MC comparison for the $t\bar{t}$ control region I.

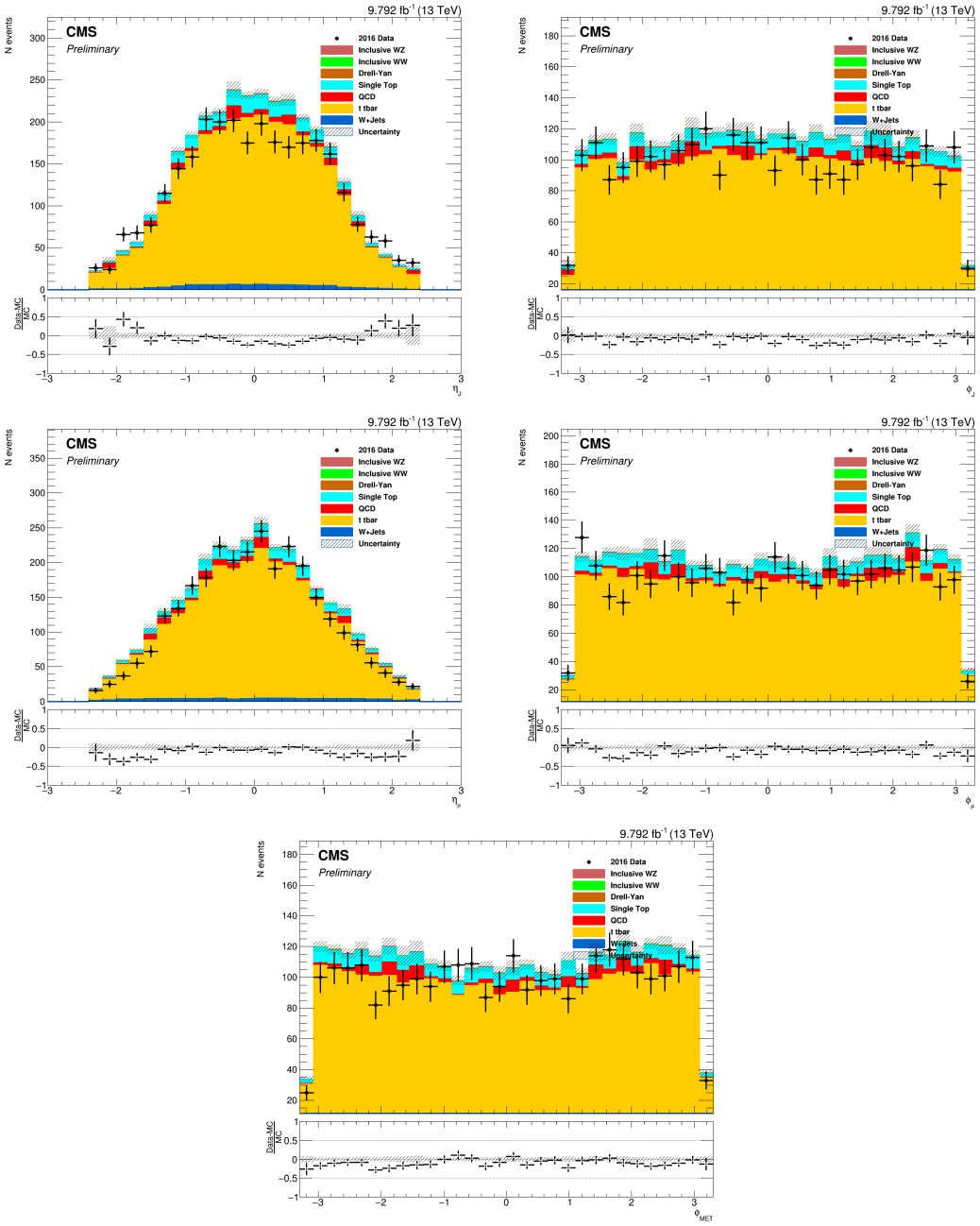

Subtitle: Comparison between data and MC of jet η (top left), jet ϕ (top right), muon η (middle left), muon ϕ (middle right), the missing transverse energy ϕ (bottom).

Source: The author, 2019.

Figure 46 - Data and MC comparison for the $t\bar{t}$ control region II.

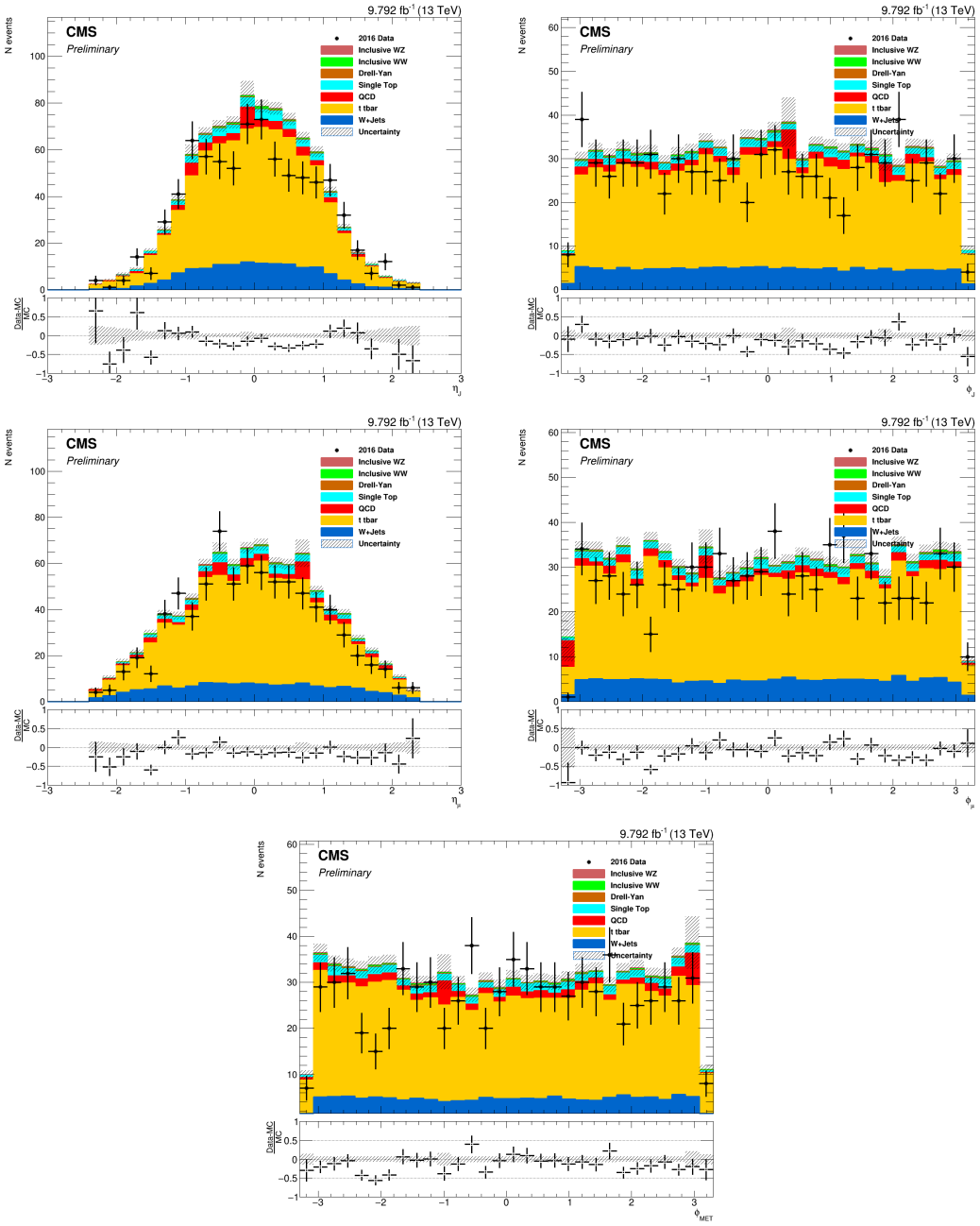

Subtitle: Comparison between data and MC of jet η (top left), jet ϕ (top right), muon η (middle left), muon ϕ (middle right), the missing transverse energy ϕ (bottom).

Source: The author, 2019.

Figure 47 - Data and MC comparison for the $W + jet$ control region.

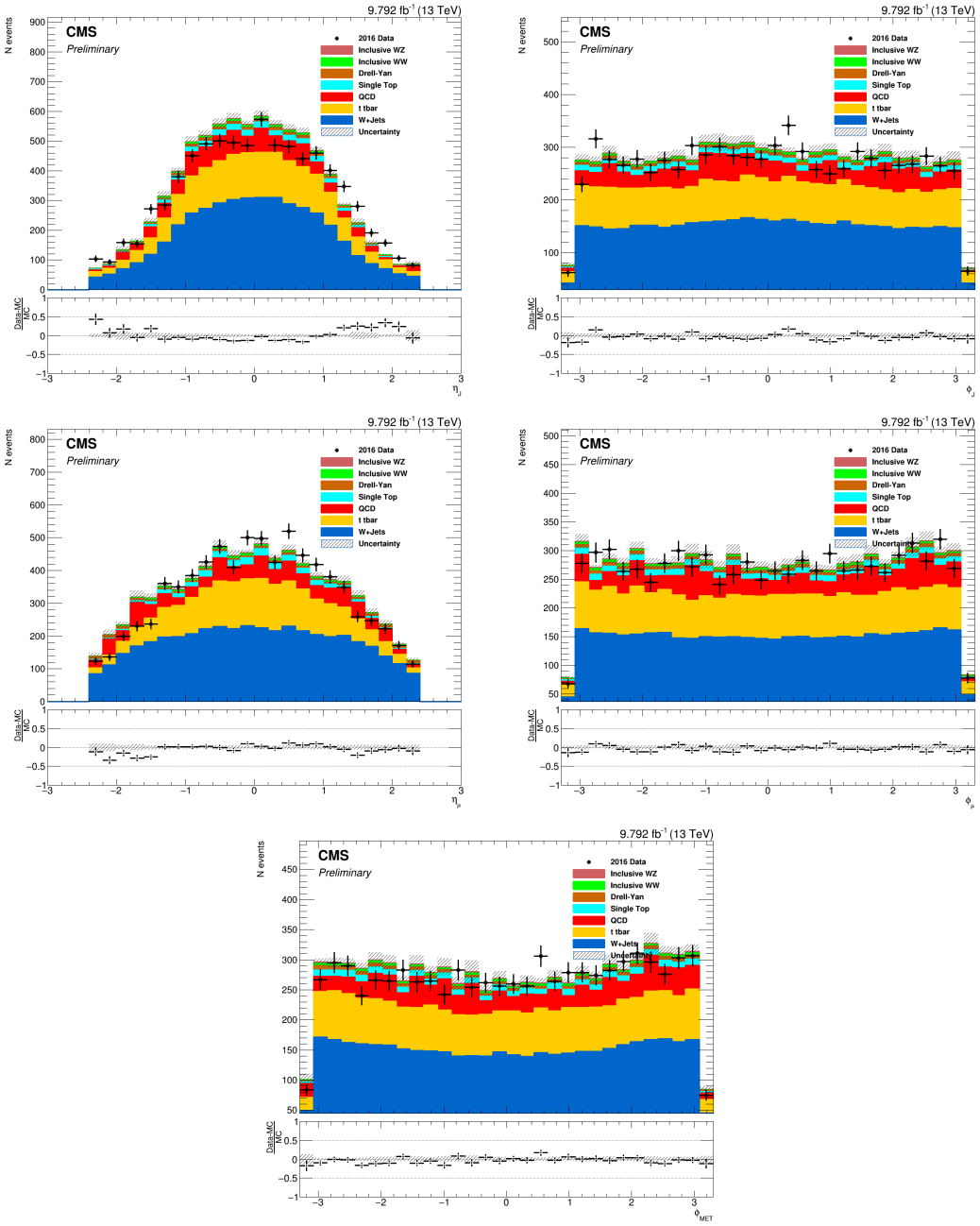

Subtitle: Comparison between data and MC of jet η (top left), jet ϕ (top right), muon η (middle left), muon ϕ (middle right), the missing transverse energy ϕ (bottom).

Source: The author, 2019.

Figure 48 - Data and MC comparison for inclusive WW region.

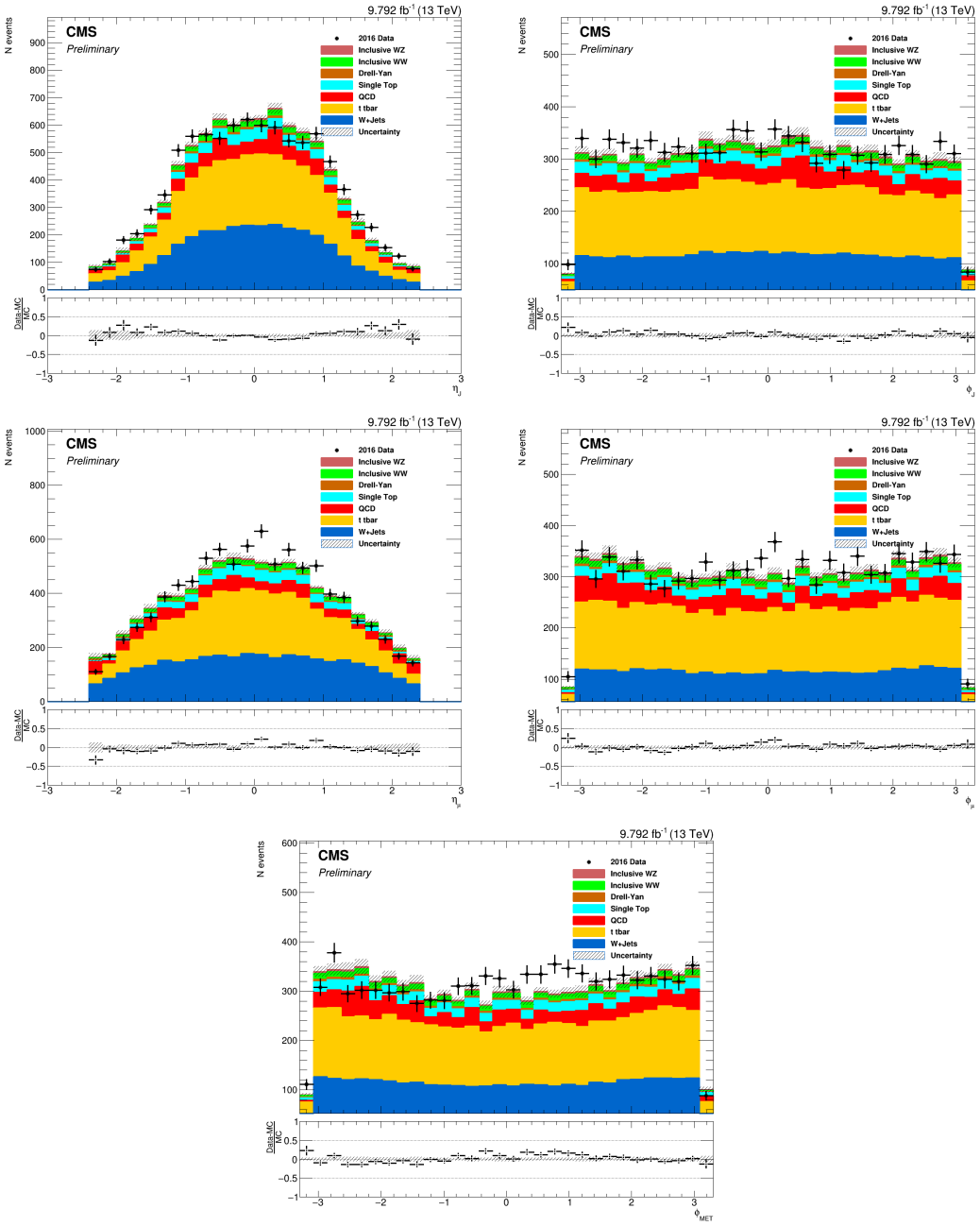

Subtitle: Comparison between data and MC of jet η (top left), jet ϕ (top right), muon η (middle left), muon ϕ (middle right), the missing transverse energy ϕ (bottom).

Source: The author, 2019.

Figure 49 - Signal MC distributions in the inclusive WW region.

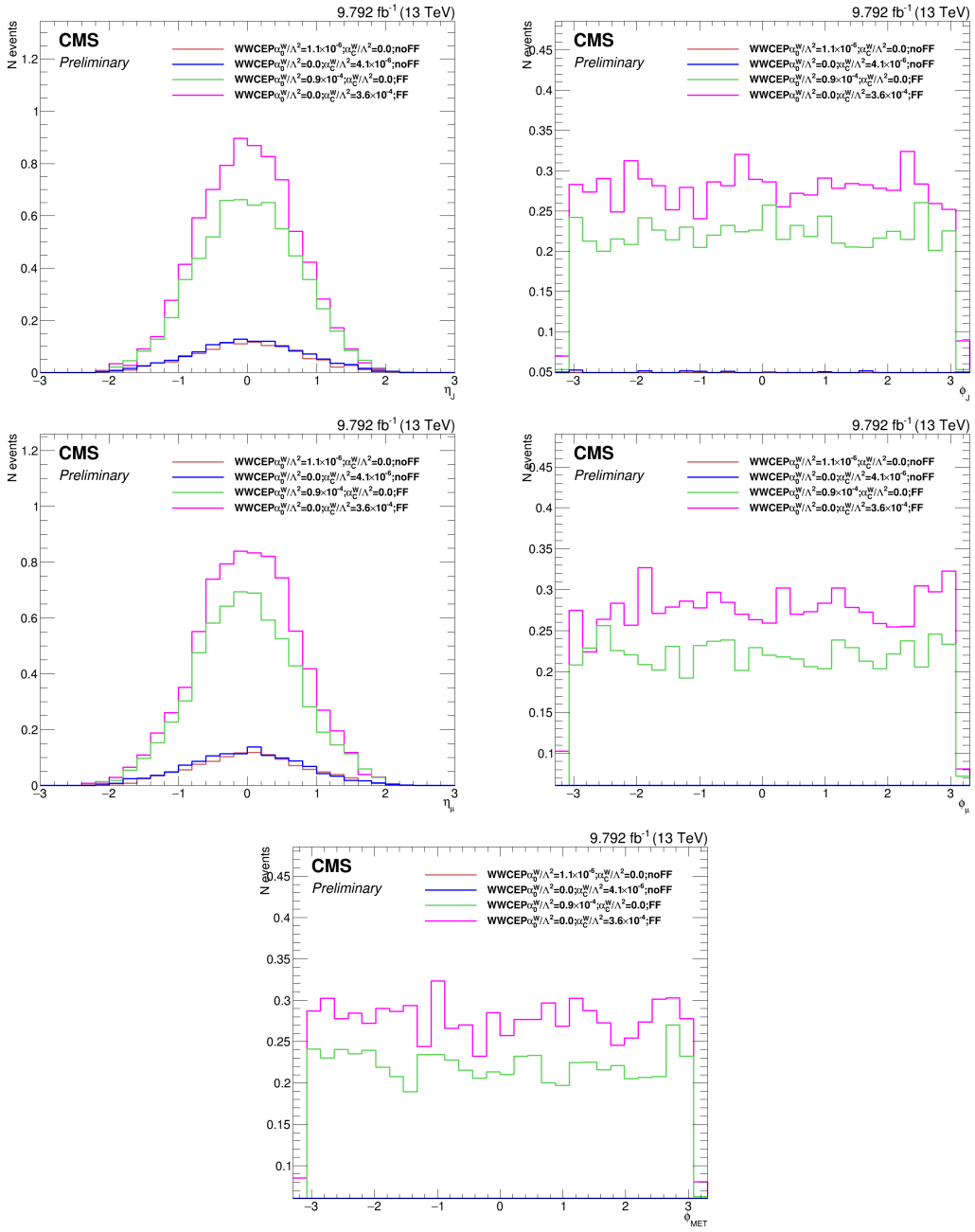

Subtitle: Signal MC distribution of jet η (top left), jet ϕ (top right), muon η (middle left), muon ϕ (middle right), the missing transverse energy ϕ (bottom).

Source: The author, 2019.

Figure 50 - Extra track multiplicity distribution considering different p_T cuts points.

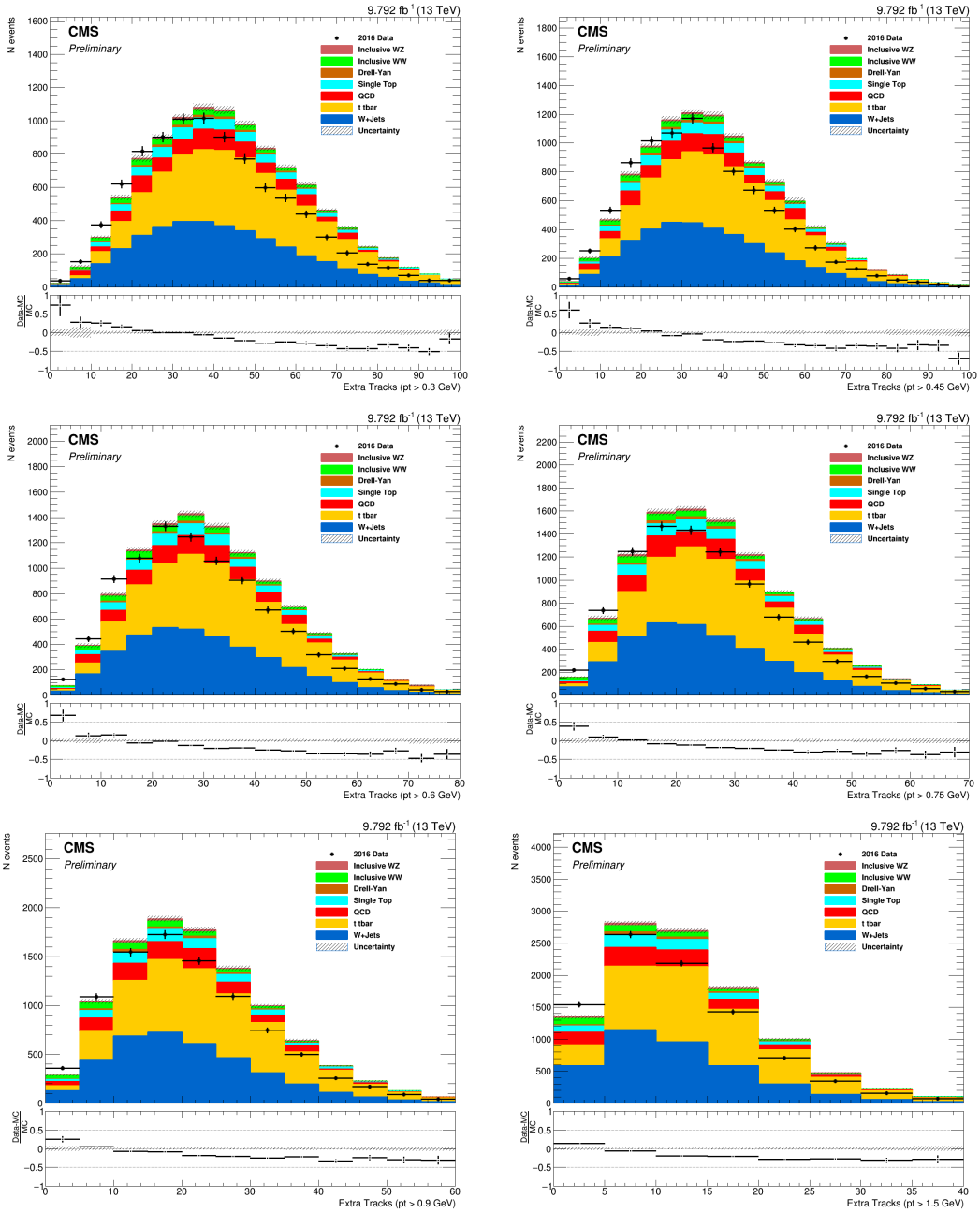

Subtitle: Comparison between data and background for extra track multiplicity considering different p_T cut points, from > 0.3GeV to > 1.5GeV.

Source: The author, 2019.

Figure 51 - Extra track multiplicity distribution considering different dz cuts points.

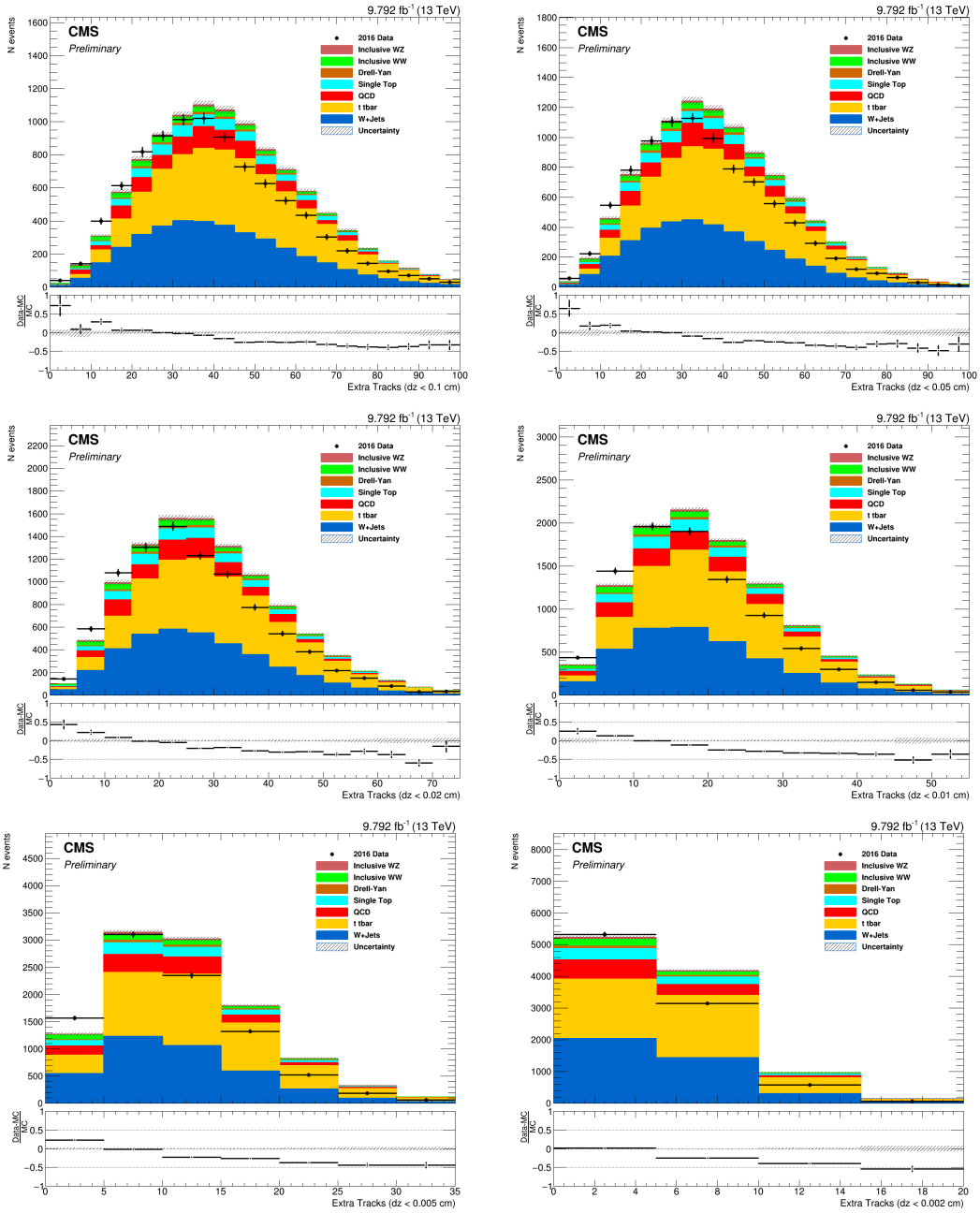

Subtitle: Comparison between data and background for extra track multiplicity considering different dz cut points, from < 0.1cm to < 0.002cm.

Source: The author, 2019.